Modelling interannual sea ice variability in the Gulf of St. Lawrence

by

Brendan DeTracey

A Thesis submitted to the

Faculty of Graduate Studies and Research

in partial fulfilment of the requirements for the degree of

Master of Science

Department of Atmospheric and Oceanic Sciences,

McGill University, Montréal, Québec.

Abstract

An uncoupled, modified Hibler ice model has been applied to the Gulf of St.Lawrence for three different winters of varying severity, in order to examine interannual sea ice variability. The simulation was initialized with observed November sea surface temperatures, and forced by weekly geostrophic winds, monthly averaged meteorological data and model geostrophic surface currents.

Results showed a general correlation with observations, reproducing differences in the sea ice cover between the years chosen. Neglecting oceanic effects caused excessive ice formation in the northwest Gulf and produced discrepancies between the observed and modelled ice edge.

Sensitivity studies revealed a high sensitivity to variations in both the forcing fields and the model free parameters. Further modelling studies must include a coupled ocean component, and force the ice component with weekly meteorological data to improve the accuracy of the prediction.

Résumé

Un modèle de glace de Hibler modifié et non-couplé a été utilisé dans le golfe du Saint-Laurent pour trois hivers de sévérités différentes, et ce pour examiner la variabilité interannuelle de la glace de mer. La simulation a été initialisée avec les températures de la surface de l'eau observées en novembre, et est controlée par des vents géostrophiques hebdomadaires, des données météorologiques moyennes mensuelles, et des courants de surface géostrophiques modélisés.

Les résultats démontrent une corrélation avec les observations en reproduisant les différences dans la couverture de glace entre les différentes années choisies, et ce en négligeant les effets océaniques causés par une formation de glace excessive dans le nord-ouest du golfe qui produisent des différences entre la limite de glace observée et simulée.

Des études de sensibilités révèlent une sensibilité élevée aux variations dans les champs externes imposés et les paramètres libres du modèle. Les études de modélisation dans le futur doivent inclure une composante océanique couplée, et aussi contrôler la composante de glace avec des données météorologiques hebdomadaires, et ce pour améliorer la précision des prédictions.

Acknowledgements

In alphabetical order:

Anonymous telephone person at Ice Central

G. Bugden

J.C. Croteau

G.&G. DeTracey

K. DeTracey

Folks from interlibrary loans

R. Gauthier

Gumby

D. Holland

R.G. Ingram

P. Mercier

V. Koutitonsky

T. Reynaud

J. Wang

& all the trees who so generously donated their lives ...

Table of Contents

List of Figures

List of Symbols and Constants

A	ice compactness	
α_{ice}	albedo of ice	0.75 / 0.616
α_{ocn}	albedo of ocean surface	0.15
C	ice strength decay constant	20.0
C_{air}	air-ice drag coefficient	2.4×10^{-3}
C_E	Dalton Number	1.75×10^{-3}
C_H	Stanton Number	1.75×10^{-3}
$c_{p,air}$	specific heat capacity of air	1004 $J\bullet kg^{-1}\bullet K^{-1}$
$c_{p,wat}$	specific heat capacity of sea water	3930 $J\bullet kg^{-1}\bullet K^{-1}$
C_{wat}	water-ice drag coefficient	10×10^{-3}
$\mathbf{D}$	coriolis force	
D_1	diffusion coefficient	$0.004\Delta x$
D_2	biharmonic diffusion coefficient	$D_1\ \Delta x^2$
Δx	grid spacing	15 km
Δt	timestep	12 h
e	vapour pressure	
ε	emissivity of ice and ocean surfaces	0.97
$\dot{\varepsilon}_{ij}$	strain rate tensor	
f	Coriolis parameter	$1.081\times10^{-4}\ s^{-1}$
$\Gamma(h/A)$	growth rate of ice of thickness h/A	
$\mathbf{F}$	internal ice stress	
$\mathbf{G}$	force due to sea surface tilt	
h	effective ice mass	
h/A	average ice thickness	
h_0	open water decay constant	0.25 m
h_{snow}	snow thickness	
h_{mix}	mixed layer thickness	

k_{ice}	conductivity of ice	2.1656 $W \cdot m^{-1} \cdot K^{-1}$
k_{snow}	conductivity of snow	0.31 $W \cdot m^{-1} \cdot K^{-1}$
L	latent heat of evaporation/sublimation	$2.5/2.834 \times 10^{-6}$ $J \cdot kg^{-1}$
L_f	volumetric heat of fusion	302 $MJ \cdot m^{-3}$
P^*	ice strength constant	27.5×10^{-3} $N \cdot m^{-2}$
ρ_{air}	density of air	1.3 $kg \cdot m^{-3}$
ρ_{ice}	density of ice	910 $kg \cdot m^{-3}$
ρ_{wat}	density of seawater	1025 $kg \cdot m^{-3}$
q_{air}	specific humidity of air	
q_{surf}	specific humidity at surface	
Q_{do}	deep ocean heat flux	
Q_{cond}	conductive heat flux	
Q_{lat}	latent heat flux	
Q_{longin}	incoming longwave heat flux	
$Q_{longout}$	outgoing longwave heat flux	
Q_{sens}	sensible heat flux	
Q_{short}	shortwave heat flux	
Q_{surf}	surface heat flux	
σ_{ij}	stress tensor	
T_{air}	air temperature	
T_B	bottom temperature of ice	-1.7 °C
T_f	freezing temperature of seawater	-1.7 °C
T_{mix}	mixed layer temperature	
T_{surf}	temperature of ice or ocean surface	
τ_{air}	force due to air-ice drag	
τ_{wat}	force due to water-ice drag	
u	ice velocity	
U_G	geostrophic surface wind	
U_{wat}	geostrophic ocean current	
ϕ	constant air turning angle	25°

θ	constant water turning angle	25°

1. Introduction

Ice covers roughly 7% of the world ocean. In the past twenty years there has been a growing interest in modelling and understanding sea ice behaviour because of its importance in global climate. Sea ice is highly reflective to solar radiation, and serves as an insulating layer between cold polar air masses and the warmer ocean beneath the ice. An increase in sea ice cover may result in local cooling which in turn would increase sea ice cover, leading to a positive feedback. The salt rejection during the freezing of sea water also tends to increase the ocean surface salinity, changing the vertical stability of the water column, and resulting in deep convective overturning. The marginal ice zones are also of interest; upwelling of nutrient rich water in these regions makes them areas of increased biological production.

Sea ice in the Gulf of St. Lawrence has been studied primarily because of its effect upon winter shipping routes, but also because of its importance to the Canadian fishing industry. The Gulf yields 25% of the Canadian commercial fish catch by weight.

The purpose of this study was to examine interannual sea ice variability in the Gulf of St. Lawrence for the years 1968, 1969 and 1972. These years have been selected because they represent extreme cases of ice cover in the Gulf: 1969 was the least severe ice season in the past 30 years; 1972 was one of the most severe; 1968 was chosen to represent an average ice season.

An uncoupled, modified Hibler ice model was applied to the Gulf for these years in a first attempt at simulating interannual ice cover variability, and as a stimulus for further climate study in this region.

2. The Gulf of St. Lawrence

2.1 Physiography and Bathymetry

The Gulf of St. Lawrence is a semi-enclosed sea with a surface area of approximately 226 000 km^2 (Forrester 1964) and a volume of 34 500 km^3 (Forrester and Vandall 1968). There are two connections with the Atlantic Ocean, Cabot Strait and the Strait of Belle Isle. Cabot Strait has a width of 104 km, a maximum depth of 480 m, and a cross-sectional area of 35 km^2; the Strait of Belle Isle is more restricted, with a width of about 15 km, a maximum depth of 60 m, and a cross-sectional area of 1 km^2 (Trites 1972).

An important bathymetric feature in the Gulf (Figure 2.1) is the Laurentian Channel, a deep trench of 500 m maximum depth, which extends from the mouth of the Saguenay River to the continental shelf. Branching off from the Laurentian Channel are the Esquiman Channel, which extends towards the Strait of Belle Isle, and the Anticosti Channel, which extends towards Jacques Cartier Passage, north of Anticosti Island. Southwest of the Laurentian Channel is a large shallow area known as the Magdalen Shallows, in which depths range from 50-80 m. Separating Prince Edward Island from Nova Scotia is the Northumberland Strait with a length of 200 km, width of 20 km and depth of 20 m. Lauzier et al.(1957) calculated that one quarter of the Gulf is shallower than 50 m while less than one fifth is deeper than 300 m.

2.2 Meteorological Forcing

Monthly-averaged wind stresses have been calculated geostrophically from mean

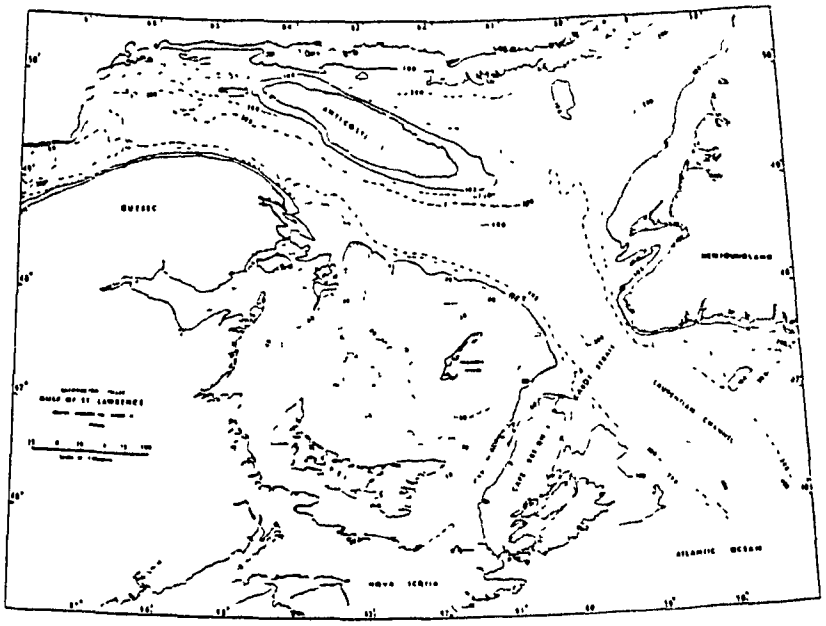

Figure 2.1 Bathymetry of the Gulf of St. Lawrence (from Canadian Hydrographic Service, Chart no. 801)

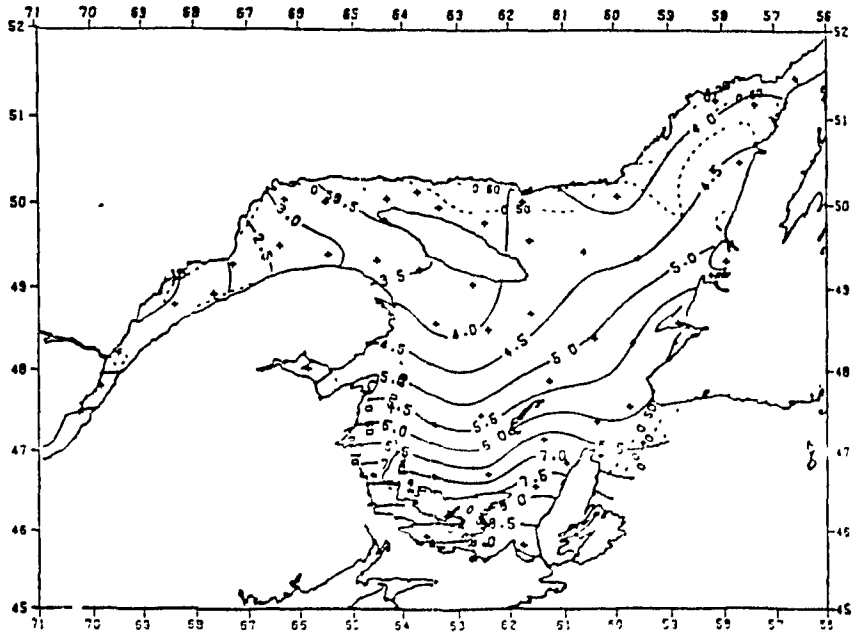

Figure 2.2 November sea surface temperature (Weiler and Keeley 1981)

sea-level pressures, interpolated from shore based stations (Murty and Taylor 1970; Vandall 1973; Koutitonsky et al. 1986). These studies show that winter winds are strongest over the Gulf, originating from the northwest in the northerly regions, and from the west in the southerly regions. From February to June the winds gradually weaken and turn until they originate from the southwest.

Mean monthly air temperature distributions over the Gulf have been compiled by Vigeant (1984) from ship measurements. These reveal that below freezing temperatures appear first over the northern shores of the Gulf and the estuary by November, and extend to Cabot Strait by December. Above freezing temperatures generally appear first over the estuary and the southwestern region of the Gulf by the end of March, and extend over the Gulf by April.

2.3 Water Masses

During the summer, the water column is vertically stratified in three distinct layers, in areas of deep water. A thin (10-30 m) upper layer of low (27-32 psu) salinity water is separated by a sharp seasonal thermocline from an intermediate cold (-1°C to 2°C) and saltier (31.5-33 psu) layer which extends down to 125 m (Koutitonsky et al. 1991). In the deep channels there also exists a bottom layer of warmer (4°C to 6°C) and saltier (34.6 psu) water (Lauzier and Bailey 1957), which interacts little with the intermediate layer.

In the fall-winter season, the entire upper layer must be cooled to freezing before ice formation begins, because the temperature of maximum density is always less than the freezing point for water with salinities greater than 24.7 psu. Salt rejected during ice

formation generates convective overturning which causes the upper and intermediate layers to merge.

Monthly averaged climatological sea surface temperature distributions have been compiled from ship data by both Weiler and Keeley (1980) and Vigeant (1987). Their results show that autumnal cooling is greatest in the northern regions of the Gulf, particularly in the Strait of Belle Isle and Estuary regions, and that SST's generally reach the freezing point first in these regions (Figure 2.2).

Bugden et al. (1982) produced seasonally averaged surface salinity fields by dividing all previously existing measurements into high and low run-off years. In both cases, lower salinity waters are seen to hug the Gaspé Peninsula shores upon leaving the estuary, follow a cyclonic distribution in the Magdalen Shallows, and exit the Gulf near the southern boundary of Cabot Strait. Higher salinity waters are found in the central and northwestern half of the Gulf. Examination of horizontal salinity gradients prior to ice formation reveals a maximum salinity difference of about 3 psu across the Gulf. The given salinity range (28.5-31.5 psu) produces freezing point differences of only 0.17 degrees, which is not considered significant enough to affect ice formation. Spatial variability in the vertical stability of the water column and the mixed layer depth is a more important factor.

2.4 Circulation

A typical summer circulation pattern for the upper layer was sketched by Trites (1972) using all the previously available data. The general circulation is cyclonic in

nature, with two way flow through both the Cabot Strait and the Strait of Belle Isle (Figure 2.3). The strongest surface currents are observed both in the Gaspé Current, which begins to develop in the Rimouski area and follows the entire length of the Gaspé coast, and in the outflow through the Cabot Strait. These currents may reach values of 20 - 40 $cm \cdot s^{-1}$.

Little is known about the winter circulation, due to the paucity of observed data. El-Sabh (1976) used monthly averaged density fields to calculate surface geostrophic currents and found the winter geostrophic currents to be considerably weaker than summertime values (Figure 2.4). Lack of wintertime T-S measurements in both the Magdalen Shallows and northeastern Gulf prevented the calculation of currents in those regions.

2.5 Heat Budget

Several investigations have been made into the surface heat budget of the Gulf. Coombs (1962) calculated a heat budget using fortnightly averaged meteorological data over the period November 15, 1961 to February 18, 1962, which he related to ice growth in Cabot Strait. Matheson (1967) investigated ice formation for two winter seasons, by classifying atmospheric circulation patterns over the gulf into five categories, and calculating the turbulent heat losses associated with each category.

Bugden (1981) calculated net climatological surface heat fluxes for several regions of the Gulf in order to develop a box model of mean monthly salt and heat budgets. He showed that the net surface heat fluxes reverse, becoming positive, during the first week

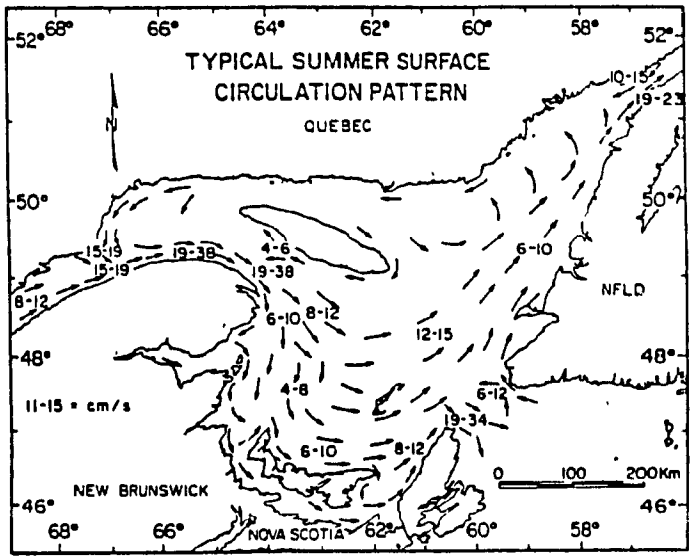

Figure 2.3 Summer surface circulation in $cm \cdot s^{-1}$ (Trites 1972).

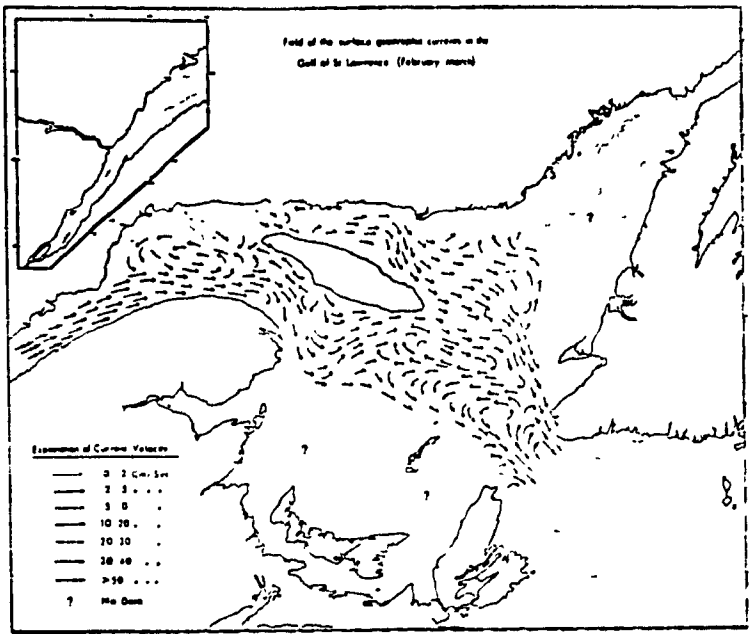

Figure 2.4 Winter surface circulation (El-Sabh 1976).

of March and reverse again in September-October, becoming negative. Maximum surface heat fluxes occur in June with values ranging from 180-256 $W \cdot m^{-2}$; minimum heat fluxes occur in December with values of approximately -250 $W \cdot m^{-2}$.

2.6 Sea Ice

Déry (1992) produced monthly averaged maps of sea ice compactness for the period 1965-1990. The monthly and seasonal averages of sea ice compactness for six sub-regions of the Gulf were examined for trends and compared to trends in forcing variables, such as surface air temperature and run-off. He found that the average ice cover for the entire Gulf did not exhibit a significant trend for the study period, but displayed a high amount of interannual variability. The greatest amount of variability was observed in deeper waters, such as the Esquiman area, which is the most saline region in the Gulf.

Correlations between ice cover and surface air temperature revealed that the ice cover often responded better to surface air temperature after a lag of one month. Déry concluded that although the ice cover often responded significantly to the immediate or the previous surface air temperature forcing, few of the series showed very high correlations that would demonstrate a strong link of the Gulf of St.Lawrence ice response to air temperature forcing.

A comparison with the run-off time series showed that the St.Lawrence River discharge was not a driving factor for ice variability, because its main spectral resonance was at a period much longer than that for the interdecadal variability of the ice cover.

Finally, T-S profiles were examined, but no simple relations could be determined due to the complexity of the system. In general, Déry found it difficult to relate the ice cover simply to any one forcing variable.

Figure 2.5 shows climatological maps of the ice onset for the weeks 3 to 6 (from mid-December to mid-January). Units are in tenths. Week 3 shows the initial ice formation. Ice concentration is highest in the lower estuary due to ice import from the St. Lawrence River. Ice formation in the upper estuary, north shore, and Strait of Belle Isle is due simply to the fact that these areas have the coldest mixed layer temperatures. In the southwest Gulf, the ice cover probably results from a rapid December cooling of the mixed layer, caused by the shallowness of the water. Weeks 4-6 show a progression of the ice edge over the Gulf towards Cabot Strait. Figure 2.6 shows monthly averaged climatological maps for January to May. Average January conditions place the ice edge at Cabot Strait, and by February the ice edge has progressed out of the Gulf. The most severe ice conditions are observed in February when the Gulf is almost completely covered. In March, the ice cover begins to melt and by April the Gulf has significantly less ice but higher ice concentrations in the northeast and south Average May conditions show an ice free Gulf with the exception of the northeast.

There is only limited information on ice thickness in the Gulf The "Ice Summary and Analyses" (Department of Transport 1968, 1969, Environment Canada 1972) reports show four thickness categories: new ice (0-10 cm), grey ice (10-15 cm), grey white ice (15-30 cm), and first year ice (>30 cm). The open-ended range of the last category makes estimation of ice thickness difficult for larger thicknesses(Figures 7.3, 7.6, 7.9;Chapter 7).

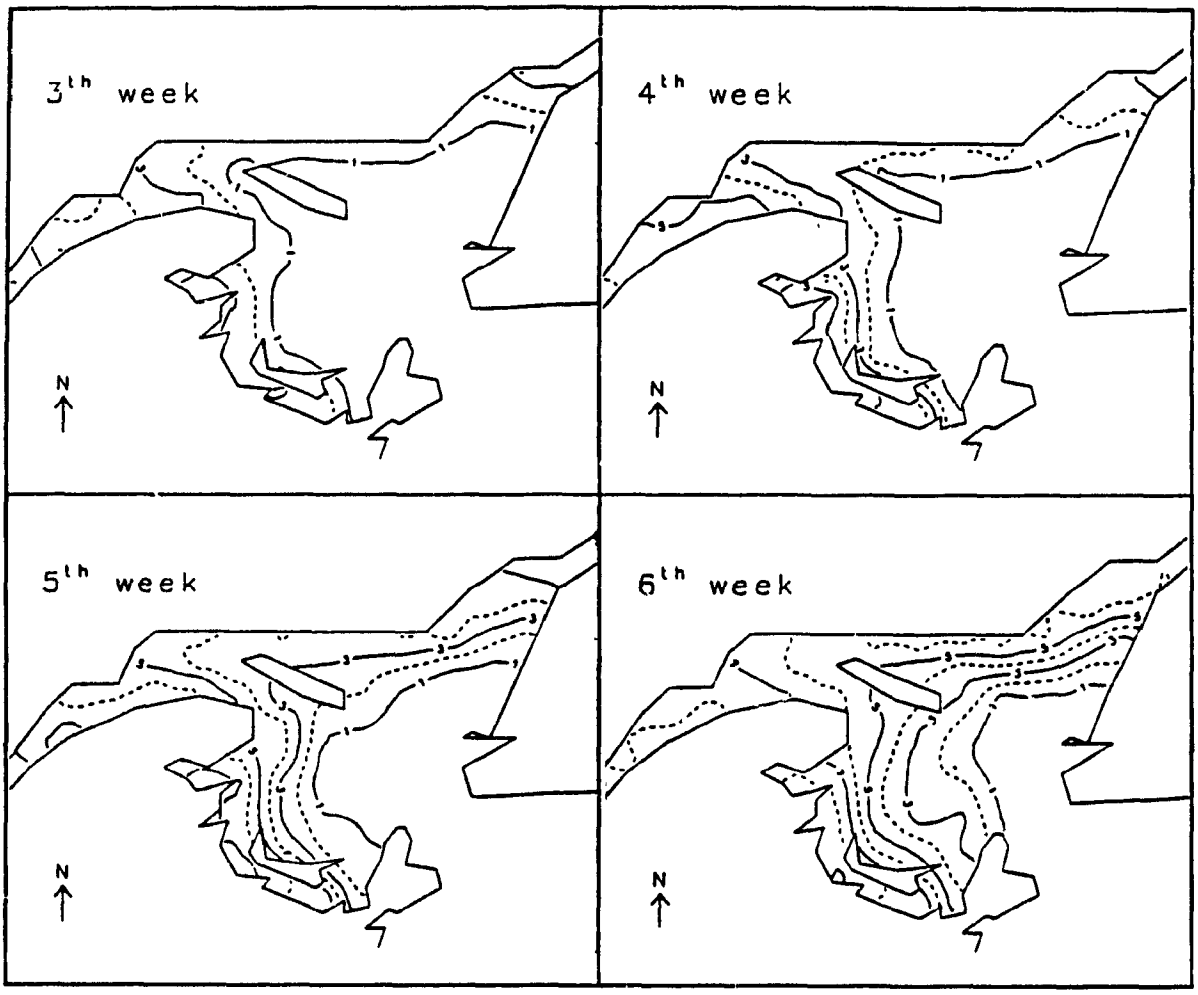

Figure 2.5 Climatological maps of ice onset, weeks 3-6 (Déry 1992).

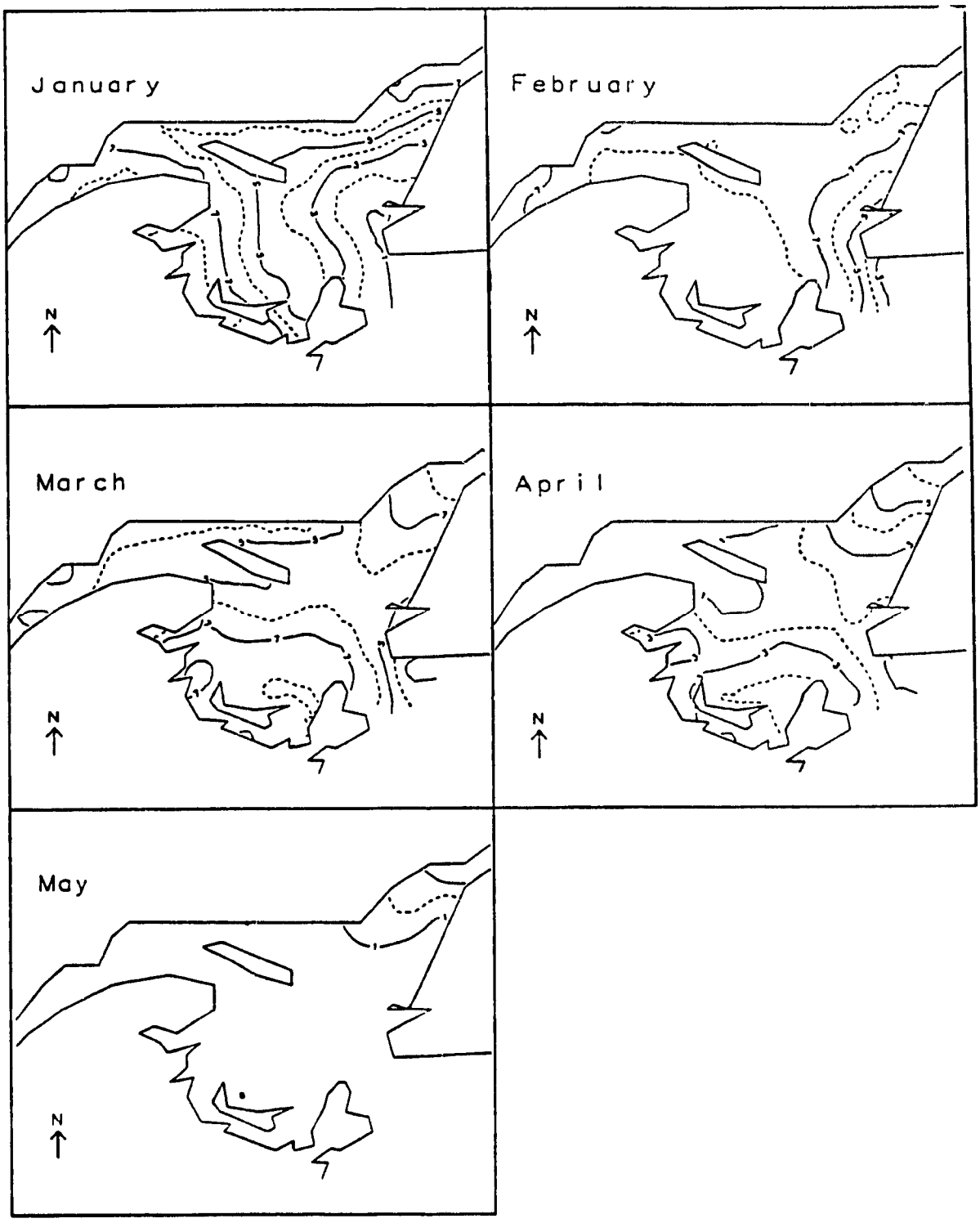

Figure 2.6 Climatological maps of monthly averaged icefields (Déry 1992).

3. A Brief History of Sea Ice Modelling

3.1 Thermodynamic Models

One of the first thermodynamic models to describe the growth and decay of sea ice was that of Anderson (1961), who correlated sea ice thickness and the cumulative number of freezing-degree days. Although such a model had a physical basis, it contained implicit assumptions about the oceanic heat flux and the snow thickness which rendered it applicable only to the region for which it was derived.

Maykut and Untersteiner (1971) developed an extensive, forty layer, one dimensional thermodynamic sea ice model, based on previous work by Untersteiner (1964). Forced by specified atmospheric heat fluxes, snowfall, and a constant deep ocean heat flux, the model produced time dependant ice thicknesses and vertical ice temperature profiles that agreed well with observations. The effects of ice salinity, brine cells, shortwave penetration, and variations in ice density, specific heat, and conductivity were all included. However, the model took thirty-eight simulation years to reach equilibrium.

Semtner (1976) simplified the Maykut and Untersteiner model in order to make it suitable for climate modelling. By changing the finite difference scheme, making simplifications in the thermodynamics, and reducing the number of vertical layers, computational time was greatly reduced, but ice thicknesses were still favourably reproduced. Semtner produced both a three layer version (two ice layers and one snow layer), and a 'zero layer' version, (one layer of ice and one layer of snow), in which short wave penetration is parameterized by modifying the surface albedo, and the ice is assigned a linear temperature profile. Most sea-ice models today use variations of

Semtner's scheme.

3.2 Dynamic Models

Studies in sea ice dynamics originate from Nansen's historic Arctic voyage, during which the first successful observations of ice drift were taken. It was Nansen's observation of the deviation betwee , ice drift and wind direction that led Ekman (1905) to his theory of drift currents. Over the following years, as more observations of ice drift were accumulated, attempts were made to solve the equation of motion for steady-state drift.

The general equation of ice motion is given by

$$m\frac{d\mathbf{u}}{dt} = \mathbf{D} + \boldsymbol{\tau}_a + \boldsymbol{\tau}_w + \mathbf{G} + \mathbf{F} \qquad (3.1)$$

where m is the ice mass(per unit area), **u** the velocity, **D** the coriolis force, τ_a and τ_w the forces due to air and water stresses, G the force component due to sea surface slope, and **F** the force between ice floes. Early attempts to solve this equation (Sverdrup 1928, Rossby and Montgomery 1935, Shuleikin 1938) assumed a steady state solution (du/dt=0), and ignored one or more of the forcing terms, usually the effects of ocean currents, sea surface slope, and force between floes.

Zubov (1943) derived an empirical rule that ice drifts parallel to surface atmospheric isobars at a speed of 1/100 of the geostrophic wind. Gordienko (1958) derived a similar relationship to Zubov's, but included a parameterization of surface roughness that made older, rougher ice drift at higher velocities.

Fukotomi (1958) included effects of ice compactness in his solution. Fel'zenbaum (1958) was the first to include the effects of water currents.

Campbell (1964) attempted the first climatological large scale numerical steady-state solution for the Arctic Ocean. He included all of the forcing terms, and followed Ruzin (1958) in treating the ice as a thin Newtonian viscous fluid in order to parameterize the force between floes. General features of observed ice drift, such as the Beaufort Gyre and the Transpolar Drift Stream were reproduced.

3.3 Thermodynamic-Dynamic Models

The first thermodynamic-dynamic model was that of Doronin (1970). Doronin coupled Nikiforov's (1957) continuity equation for ice compactness to equations describing the dynamic and thermodynamic evolution of the ice, parameterizing the internal ice force as a function of ice compactness. Doronin concluded that thickness and compactness could not be accurately calculated unless thermodynamics were included.

During the Arctic Ice Dynamics Joint Experiment (AIDJEX) (1970-1972) extensive measurements resulted in a better understanding of the dynamic and thermodynamic properties of sea ice. Thorndike et al. (1975) developed a set of equations that described the dynamics and thermodynamics of an ice thickness distribution; Rothrock (1975) explained how to couple such a distribution to an ice rheology. Much attention was paid to finding an appropriate rheology with which the interactive force between floes could be parameterized. Coon et al. (1974) suggested ice could be modelled by plastic behaviour; Pritchard (1975) considered an elastic-plastic rheology.

The final AIDJEX ice model (reviewed in Coon 1979) successfully modelled the dynamics and thermodynamics of sea ice on spatial scales of 100 km and time scales of 1 day. No attempt was made to use the model in areas of low concentration, nor was any attention given to describing the thermodynamics between the ice and upper ocean.

Parkinson and Washington (1979) simulated the annual cycle in both the Arctic and Antarctic using the zero layer Semtner model, with lead parameterizations (Washington et al. 1976), and coupling it to the steady-state equation of motion. Monthly averaged temperatures, snowfall rates, and wind stress were used to force the ice. The ocean was represented by a 30 m thick, motionless, mixed layer. Internal ice resistance was parameterized by iteratively correcting the ice velocities such that no one grid square exceeded a prescribed maximum ice concentration. The annual ice cycle was reasonably reproduced but the ice thickness distribution did not agree with observations.

Hibler (1979,1980) also presented a model of the yearly Arctic ice cycle which incorporated a viscous-plastic ice rheology. Eight day averaged geostrophic winds and mean dynamic topography were used for dynamic forcing; ice growth and melt was calculated using seasonal growth rates estimated by Thorndike et al. (1975). Later papers included the zero layer Semtner thermodynamic model and a motionless ocean mixed layer.

Hibler and Walsh (1982) applied the Hibler model to the Arctic for the 1973-1975 period, with daily forcing. Agreement with observations was good except in the northern Atlantic, where too much ice was predicted, probably due to warm Atlantic water inflow not included in the model. Also, the simulated summer melt in the Beaufort Sea was too

strong due to the absence of a modelled snow cover, which would have reflected more of the solar energy and delayed the summer melt.

3.4 Coupled Ice-Ocean Models

Neglect of the ocean component prevented earlier modelling attempts from accurately predicting the large scale sea-ice edge in the Greenland and Barents Seas. The first coupled ice-ocean model (Hibler and Bryan 1984, 1987) combined the previously described Hibler ice model with a multi-level Bryan-Cox ocean model (Bryan, 1969). Hibler and Bryan compared the coupled results to previous results and found the winter ice margin to be significantly improved. They also found that the inclusion of ocean currents greatly increased the ice drift in the East Greenland Current, accounting for about 50% of the total drift rate.

Semtner (1987) produced similar results by coupling his three layer thermodynamic ice model, to a "bulk viscous" dynamics (Hibler 1988), and to a fully prognostic general circulation ocean model (Semtner 1974, 1986). Comparing results to those from using a fixed depth motionless mixed layer revealed that the central Arctic ice thickness and compactness were drastically reduced by full ocean coupling.

4. Model Description

The following chapter gives a brief description of the Hibler (1979,1980) ice model.

4.1 Momentum Balance

Following the notation of Hibler (1979), the momentum equation for ice is given by,

$$m\frac{du}{dt} = -mf\,k\times u + \tau_{air} + \tau_{wat} - mg\nabla H + F \qquad (4.1)$$

where d/dt is the substantial time derivative , k a unit vector normal to the surface, u the ice velocity, f the coriolis parameter, m the ice mass per unit area, τ_{air} and τ_{wat} forces due to air and water stresses, H the sea surface dynamic height, g the acceleration due to gravity, and **F** the force due to variation in internal ice stress. Tidal forcing is omitted.

The air and water stress terms are determined from simple nonlinear drag laws (Brown 1979, McPhee 1975)

$$\tau_{air} = \rho_{air} C_{air} |U_g| (U_g \sin\phi + k\times U_g \sin\phi) \qquad (4.2)$$

$$\tau_{wat} = \rho_{wat} C_{wat} |U_{wat} - u| [(U_{wat} - u)\cos\theta + k\times(U_{wat} - u)\sin\theta] \qquad (4.3)$$

where U_g is the geostrophic wind, U_{wat} is the geostrophic ocean current, C_{air} and C_{wat} are the air and water drag coefficients, ρ_{air} and ρ_{wat} are air and water densities, and ϕ and θ

are constant air and water turning angles. For the atmospheric drag law, the ice velocity **u** is omitted since it is considered negligible compared to the geostrophic winds.

4.1.1 Drag Coefficients

The air-ice drag coefficient C_{air} is chosen to be a constant value of 2.4×10^{-3}. In reality, it is a function of wind speed, atmospheric stability, and surface roughness and compactness. Measurements of C_{air} range from $1.2 - 5.3\times10^{-3}$ (Overland 1985, Guest and Davidson 1987). A value of 2.4×10^{-3} is a reasonable average between first year rough and smooth ice.

The water-ice drag coefficient C_{wat} is chosen to be 10×10^{-3}. Measurements of C_{wat} are scarce and range from $2 - 21\times10^{-3}$ (Shirasawa and Ingram 1991).

Both values are similar to those chosen by Tang and Yao (1987) in a modelling study of sea-ice motion off Newfoundland during LIMEX 1987(Labrador Ice Margin Experiment).

4.2 Ice Thickness Distribution

The sea ice in any grid cell is characterized by two variables: the compactness A, defined as the areal fraction covered by ice, and the effective ice mass per unit area h, which is defined as the ice thickness if the ice were spread uniformly over the entire grid cell. The ice is assumed to be uniformly distributed between 0 and 2h/A in thickness, with an average ice thickness h/A. Continuity equations, with added thermodynamic source/sink terms, are used to describe the evolution of A and h, as

follows,

$$\frac{\partial h}{\partial t} = -\frac{\partial (uh)}{\partial x} - \frac{\partial (vh)}{\partial t} + S_h + (diffusion)_h \tag{4.4}$$

$$\frac{\partial A}{\partial t} = -\frac{\partial (uA)}{\partial x} - \frac{\partial (vA)}{\partial t} + S_A + (diffusion)_A \tag{4.5}$$

where u and v are the x and y components of the ice velocity. S_h and S_A are the thermodynamic source/sink terms given by the equations,

$$S_h = \Gamma(\frac{h}{A})A + (1 - A)\Gamma(0) \tag{4.6}$$

$$S_A = \begin{cases} (\Gamma(0)/h_0)(1-A), & \text{if } \Gamma(0)>0, \\ 0, & \text{if } \Gamma(0)<0, \end{cases} + \begin{cases} 0, & \text{if } S_h>0, \\ (A/2h)S_h, & \text{if } S_h<0. \end{cases} \tag{4.7}$$

where $\Gamma(h/A)$ is the growth rate of ice of thickness h/A, and $\Gamma(0)$ is the growth rate of ice upon open water. The diffusion terms are added for numerical stability and are small. The net ice growth or melt is given by S_h which is the sum of the ice growth/melt over the fraction of the grid cell covered with ice and the growth/melt of new ice over the remaining fraction of open water. If $\Gamma(0)$ is negative (melting) the excess heat is assumed to produce lateral melting, and is used to melt any ice remaining in the grid cell, while the mixed layer temperature remains at the freezing point.

The growth/decay of ice compactness is given by S_A. The first term in Equation (4.7) specifies that if the growth of ice over open water $\Gamma(0)$ is positive then the area of open water (1-A) decays exponentially with a time constant $h_0/\Gamma(0)$. The term h_0 is an adjustable parameter. Hibler originally chose a value of 0.5 m which gave decay times of approximately 5 days. If $\Gamma(0)$ is negative, it does not contribute to a change in A, but as previously mentioned, contributes to lateral melt. The second term in Equation (4.7) describes the change in ice compactness under melting conditions. Assuming the ice is uniformly distributed between 0 and 2h/A in thickness and that all thicknesses melt at the same rate, over a time Δt all ice of thickness less than $S_h\Delta t$ will melt and form open water. This ice covers a fraction of area equal to $S_h\Delta t$ A/2h, which for Δt small gives the sink term in Equation (4.7).

Finally, an additional mechanical sink term is introduced by the condition $A \leq 1$.

4.3 Constitutive Law

The internal ice force **F** is determined from the partial derivatives of the two dimensional stress tensor σ_{ij}, that is $F_i = \partial\sigma_{ij}/\partial x_j$. The stress tensor is given by

$$\sigma_{ij} = 2\eta\dot{\epsilon}_{ij} + [(\zeta - \eta)\dot{\epsilon}_{kk} - P]\delta_{ij} \qquad (4.8)$$

where ϵ_{ij} is the strain rate tensor, P is a pressure term dependent on both thickness and compactness, ζ is the nonlinear bulk viscosity, η is the nonlinear shear viscosity, ϵ_{kk} is the trace of the strain rate tensor, and δ_{ij} is the Kronecker delta function. For more details the reader is referred to Hibler (1977,1979). Hibler's formulation treats ice as a viscous

fluid for small deformation rates, and as a rigid plastic fluid for large deformation rates. This choice of rheology is based on the following assumptions: i) on a reasonably large scale, sea ice is isotropic; ii) sea ice has little resistance to divergent stresses; iii) stresses are relatively independent of strain rate magnitude; iv) sea ice is highly resistant to convergent stresses. The advantages of this rheology are that an Eulerian formulation and larger timesteps may be used. The disadvantage is that ice which should be stationary, can still move in the numerical model. The pressure term P is given by the equation

$$P = P^* h \exp[-C(1-A)] \tag{4.9}$$

in which P^* is a constant called the ice strength. Studies have revealed an order magnitude difference between observations and numerical simulations for the value of P^* (Häkkinen 1990); it is generally regarded as an adjustable parameter. Hibler's original choice of P^* was 5.0×10^3 $N \cdot m^{-3}$ but he later increased this value by a factor of five. The constant C has some large value, such as 20, to produce a rapid decrease in viscosity for ice concentrations less than 85% (Häkkinen 1990).

More recently, Overland and Pease (1988) developed a constitutive law for first year ice in coastal regions, in which ice strength depends quadratically, instead of linearly, on ice thickness. Their model is applicable only on spatial scales of less than 10 km.

4.4 Thermodynamics

4.4.1 Surface Heat Budget

A comprehensive overview of the surface heat and mass balance, and the

growth of sea ice may be found in Maykut (1986).

The thermodynamics are based on the zero layer Semtner (1976) model, using surface heat budget calculations similar to those of Parkinson and Washington (1979). Two separate heat budgets are performed for each grid cell: one for open water and one for ice covered water.

The mixed layer is treated as a slab of fixed thickness that must cool entirely to freezing before ice formation begins. The surface heat budget terms that must be considered over open water are incoming short wave, incoming atmospheric longwave, outgoing longwave, and sensible and latent heat exchange. Designating positive fluxes to be those entering the surface, the heat balance is given by

$$Q_{surf} = (1 - \alpha_{ocn})Q_{short} + Q_{longin} - Q_{longout} + Q_{sens} + Q_{lat} \qquad (4.10)$$

in which α_{ocn} is the ocean albedo.

The ice covered case has a similar heat balance given by

$$Q_{surf} = (1 - \alpha_{ice})Q_{short} + Q_{longin} - Q_{longout} + Q_{sens} + Q_{lat} + Q_{cond} \qquad (4.11)$$

where Q_{cond} is an additional term representing the conductive flux through the ice. The various radiation flux terms are described below.

Incoming Shortwave: See section 6.4, chapter 6.

Incoming Longwave: Incoming longwave is calculated using the empirical relation derived by Maykut and Church (1973),

$$Q_{longin} = 0.7855(1 + 0.2232C^{2.75})\sigma T_{air}^4 \qquad (4.12)$$

where C is the cloud fraction in tenths, σ is the Stefan-Boltzmann constant, and T_{air} is the

air temperature. This method was compared to that used by Parkinson and Washington (1979) which applied a cloudiness correction (Marshunova 1961) to a clear sky longwave parameterization by Idso and Jackson (1969). Both methods produced almost identical results.

Outgoing Longwave: Both ice and ocean are treated as blackbodies for longwave emission. That is

$$Q_{longout} = \varepsilon \sigma T_{surf}^4 \tag{4.13}$$

where ε is emissivity of either sea water or ice, σ is the Stephan-Boltzmann constant, and T_{surf} is either the mixed layer temperature, or the surface temperature of the ice.

Sensible Heat: Sensible heat is calculated using the standard bulk aerodynamic formula

$$Q_{sens} = \rho_{air} c_{p,air} C_H |U_G| (T_{air} - T_{surf}) \tag{4.14}$$

where ρ_{air} is the air density, $c_{p,air}$ the specific heat of air, C_H the turbulent heat exchange coefficient, U_G the geostrophic wind, and T_{air} and T_{surf} the temperatures of the air and the surface(ocean or ice).

Latent Heat: Latent heat is calculated from the bulk formula

$$Q_{lat} = \rho_{air} L C_E |U_G| (q_{air} - q_{surf}) \tag{4.15}$$

where L is the latent heat of vaporization or sublimation, depending on whether an ice cover exists, C_E is the latent heat turbulent exchange coefficient, and q_{air} and q_{surf} are the air and surface specific humidities. The formulae to determine the specific humidities are

(Haltiner and Martin 1957)

$$q_{air} = \frac{0.622e}{p - (1 - 0.622)e} \tag{4.16}$$

$$q_{surf} = \frac{0.622e_s}{p - (1 - 0.622)e_s} \tag{4.17}$$

where p is the air pressure. Vapour pressure e and saturation vapour pressure e_s are determined from the empirical formula (Murray 1967)

$$e_s = 611 \times 10^{a(T_{surf}-273.16)/(T_{surf}-b)} \tag{4.18}$$

where (a,b) = (9.5, 7.66) if an ice cover exists and (7.5, 35.86) if no ice cover exists. For e, Equation (4.17) is used with T_{surf} replaced by the surface dew point temperature T_d.

Conductive Flux: Treating the ice as a slab of average thickness h/A, the conductive flux through the ice is given by

$$Q_{cond} = \frac{k_{ice}}{(h/A)}(T_B - T_{surf}) \tag{4.19a}$$

where k_{ice} is the conductivity of the ice, T_B is the bottom temperature of the ice slab, and T_{surf} , as stated previously, is the surface temperature of the ice. T_B is set to the freezing point. In the presence of snow, the conductivity is replaced by a weighted average of the conductivities of snow and ice. That is,

$$Q_{cond} = \frac{k_{ice}k_{snow}}{k_{ice}h_{snow} + k_{snow}\left(\frac{h}{A}\right)}(T_B - T_{surf}) \tag{4.19b}$$

Deep Ocean Heat Flux: The deep ocean heat flux Q_{do} is meant to represent the heat provided to the slab mixed layer, from the deeper waters below, through convective overturning. For the central Arctic Basin, its value has typically been chosen at 2 $W \cdot m^{-2}$ (Maykut and Untersteiner 1969, Hibler 1979, Washington and Parkinson 1979). Allison (1981) inferred values of 15-50 $W \cdot m^{-2}$ during the first month of growth of Antarctic ice, and 7-15 $W \cdot m^{-2}$ in succeeding months. The value of Q_{do} would be expected to be greatest during ice formation, and smallest during ice melt when the water column increases in stability. For the Gulf , Q_{do} is chosen to be 40 $W \cdot m^{-2}$ from December 15 to January 30, and 10 $W \cdot m^{-2}$ until March 15, in grid squares with at least 5 cm of ice. A sensitivity study was then used to investigate the effects of Q_{do}.

4.4.2 Calculating Ice Growth

The ice growth rate f(d) is determined in the following manner. For open water

$$\Gamma(0) = \frac{Q_{surf} + Q_{do}}{L_f} \qquad (4.20)$$

where L_f is the volumetric heat of fusion of sea water. The total heat gained or lost by the mixed layer is the sum of the surface heat flux and the deep ocean heat flux Any energy lost by the mixed layer, after it is cooled to freezing, results in the formation of an equivalent volume of ice

In the ice covered grid cell fraction, the growth rate is determined by assuming that the surface energy balance is in equilibrium. That is,

$$(1 - \alpha_{ice})Q_{short} + Q_{longin} - Q_{logout} + Q_{sens} + Q_{lat} + Q_{cond} = 0 \qquad (4.21)$$

and that the surface temperature adjusts to maintain this equilibrium. Equation (4.21) is solved iteratively for T_{surf} using the Newton-Raphson procedure. After the surface temperature has been found, the net heat flux into the ice is known and the ice growth is calculated by the following equation,

$$\Gamma(h/A) = \frac{-(Q_{cond} + Q_{do})}{L_f} . \qquad (4.22)$$

where L_f is the volumetric heat of fusion of water.

4.5 Ocean Mixed Layer

As stated previously the ocean mixed layer is represented by a non-moving slab. The mixed layer depth, although temporally constant, varies spatially. Figure 4.1 shows the mixed layer depth field produced by examining climatological November sigma-t profiles for the Gulf (Petrie 1990). Overall, the Gulf was assigned a mixed layer depth of about 40 m, except for the Magdalen Shallows which was assigned an approximate depth of 20 m. Attempts to produce mixed layer depth fields for each year were unsuccessful due to several factors. The mixed layer depths exhibited a high amount of spatial variability and there were not enough measurements from any one year to produce a reliable objective analysis. Also, the November cruise data was sampled at 10 m intervals, which introduces a large uncertainty when determining the mixed layer depth. The mixed layer depth field used falls within this uncertainty, for each year considered.

In the absence of an ice cover, the mixed layer temperature is calculated

diagnostically from

$$\rho_w c_{p,w} h_{mix} \frac{\partial T_{mix}}{\partial t} = Q_{surf} + Q_{do} \qquad (4.23)$$

where h_{mix} is the mixed layer depth, ρ_w is the density of sea water, $c_{p\,w}$ is the specific heat of sea water, T_{mix} is the mixed layer temperature, Q_{surf} is the net surface energy flux described by Equation 4.10, and Q_{do} is the deep ocean heat flux. If Equation 4.23 produces a temperature below freezing, the temperature remains at the freezing point and ice is formed. The freezing point is set to a constant value of -1.7 ^{0}C, which is equivalent to a water salinity of 31 psu. This is considered adequate given the small range of surface salinities encountered in the Gulf.

4.6 Thermodynamic/Radiative Constants

The ocean albedo was set at 0.15. The ice albedo was chosen as by Hibler (1980). For surface temperatures below freezing, a snow covered ice albedo of 0.75 was used. For temperatures above 273.16 K, a snow free albedo of 0.616 was used. The emissivities of ice and ocean were 0.97. The sensible and latent heat exchange coefficients were both set at 1.75×10^{-3}, following Hibler (1980). For the ice conductivity Semtner's(1976) adjusted value of 2.1656 $W\bullet m^{-1}\bullet K^{-1}$ was used.

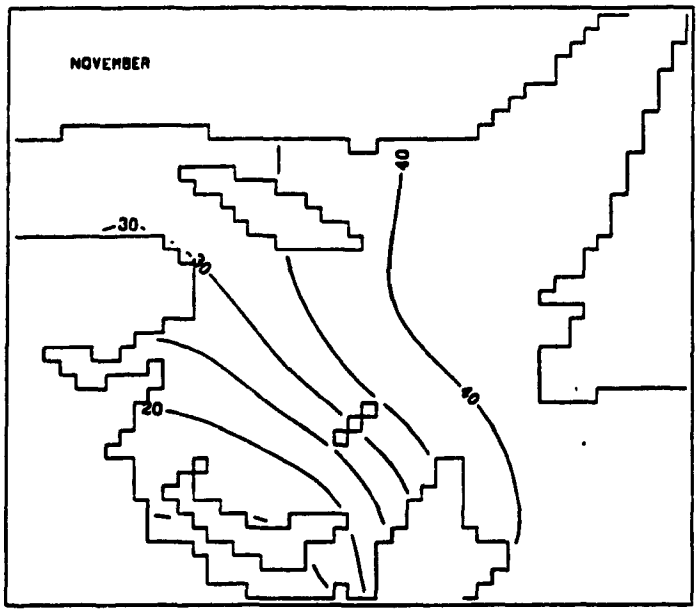

Figure 4.1 November mixed layer depth field. Depths are in metres.

5. Numerical Methods

5.1 Model Grid

Figure 5.1 shows the model grid. The grid cell dimensions are 15 km × 15 km. This is the largest grid spacing that will resolve all of the major straits, excluding the Northumberland Strait. At each ocean grid point, a sea ice velocity is calculated. The ice thickness and compactness are calculated at points on another grid which is staggered with respect to the velocity grid (Figure 5.2). This configuration is known as a 'B-grid' (Mesinger and Arakawa 1976).

5.2 Numerical Integration Scheme

The momentum equation (Eq. 4.1) is solved using a semi-implicit predictor corrector procedure (Ames 1969) that centres the nonlinear terms. Two relaxations are required at each timestep, one to centre the nonlinear terms and one to advance to the next timestep. For each case, point relaxation techniques are used to solve the linearized implicit equations. The acceleration term is included by a backward time step.

The continuity equations (Equations 4.4 & 4.5) are integrated explicitly; the advection terms are integrated by a modified Euler step (Kurihara 1965), accurate to second order in time, while the thermodynamic and diffusion terms use a forward Euler step. The diffusion terms in the continuity equations (Equations 4.4 & 4.5) are given by

$$(diffusion)_h = D_1\nabla^2 h + D_2\nabla^4 h \qquad (5.1)$$

$$(diffusion)_A = D_1 \nabla^2 A + D_2 \nabla^4 A \qquad (5.2)$$

where $D_1 = 0.004\ \Delta x$ and $D_2 = \Delta x^2\ D_1$. These terms are included for numerical stability, although diffusion of sea ice may actually occur due to random effects. The diffusive fluxes are estimated to be less than 3% of the advective fluxes in this model (Hibler 1979).

The coupled equations are effectively solved by a forward-backward scheme (Mesinger and Arakawa 1976). The only essential stability requirement is a CFL condition for the advection terms: $\Delta t \leq \Delta x\ (2^{1/2} \mid u \mid)^{-1}$. Assuming a maximum ice velocity of 20 $cm \cdot s^{-1}$ and a grid size of 15 km, yields a maximum timestep of 14.7 hours. Therefore, a half day time step was used.

5.3 Boundary Conditions

A no slip condition was used on ocean-land boundaries, meaning the shoreline ice velocities were set to zero. The diffusion coefficients were also zero for boundary points. For the St. Lawrence estuary, Strait of Belle Isle, and the Atlantic Ocean boundary points, a zero-gradient boundary condition was prescribed. Ice was also allowed to advect freely in or out of the domain on these boundaries by setting the ice strength to zero.

For a more complete description of the spatial finite differencing, and time integration methods, the reader is referred to Hibler (1979).

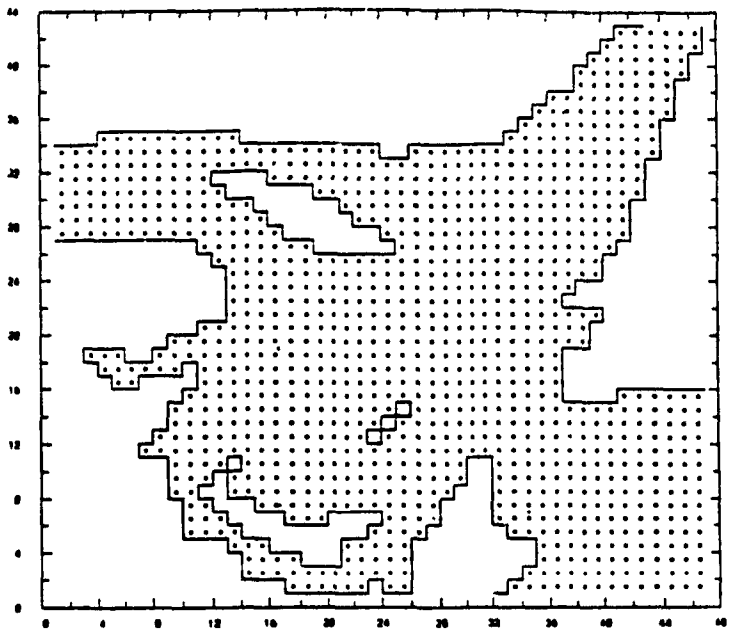

Figure 5.1 Model grid for the Gulf of St.Lawrence. Grid spacing is 15 km.

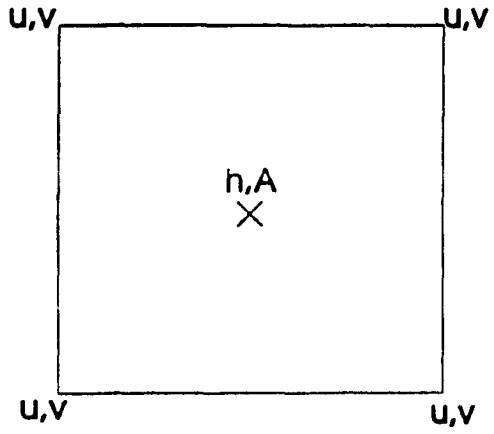

Figure 5.2 Staggered grid used in numerical calculations.

6. Forcing Fields

The model forcing fields described in this chapter may all be found in the Appendix.

6.1 Objective Analysis

To interpolate sparse data to the model grid, a simple objective analysis (Haltiner and Williams 1980) was performed. This method involves taking an initial guess field of the desired quantity, and correcting this field using a weighted mean of the difference between the observed and initial guess fields for all observations within a given radius of influence. The scheme is formally described by equations 6.1-6.3

$$T = T_{guess} + \frac{\Sigma WQ}{\Sigma W} \qquad (6.1)$$

$$Q = T_{guess} - T_i \qquad (6.2)$$

$$W = 0, \quad if \quad r>R \quad OR \quad W = e^{-\frac{4r^2}{R^2}}, \quad if \quad r \leq R \qquad (6.3)$$

in which r is the spatial distance between the gridpoint and the observation T_i, and R is the radius of influence. The weighting function (Equation 6.3), taken from Levitus (1982), is strongly dependant on r.

The corrected field is then used as the guess for another iteration using a smaller radius of influence. Iteration is continued until the difference between observations and the corrected field is less than a prescribed error, or until a maximum number of iterations has been performed.

6.2 Air and Dew Point Temperatures

Mean monthly air and dew-point temperatures for fifteen stations surrounding the Gulf were obtained from the Atmospheric Environment Service of Canada. The station locations are shown in Figure 6.1. The lack of data over the Gulf itself leads to difficulties in performing an objective analysis. The initial guess fields for both air and dew point temperatures were taken from a climatological atlas (Environment Canada 1987). Using the traditional method of applying a successively decreasing radius of influence did not yield satisfactory results, often giving an average error greater than one degree Celsius between the observed and objectively analyzed values. However, a constant radius of influence of 375 km (25 gridpoints) applied successively for up to 20 iterations gave average errors less than 0.5 degrees Celsius. Overall, the analyzed fields can not be expected to be exact, but are only crude representations of the temperature gradients between meteorological stations.

6.3 Wind Fields

Mean weekly and fortnightly sea surface pressure charts were digitized from a set of ice summary and analysis publications produced by the Department of Transport, Meteorological Branch, Canada (1968,1969) and the Atmospheric Environment Service (1972). Surface pressures are digitized onto a 49 point grid and cubic-spline fitted to the model grid.

Surface winds were calculated using the geostrophic approximation. This assumption may not be accurate close to the shore where topographic effects are involved.

1	Sept Isles
2	Natashquan
3	Blanc Sablon
4	Daniel's Harbour
5	Stephenville
6	Port aux Basques
7	Burgeo
8	Sydney
9	Grindstone Island
10	Charlottetown
11	Chatham
12	Charlo
13	Gaspé

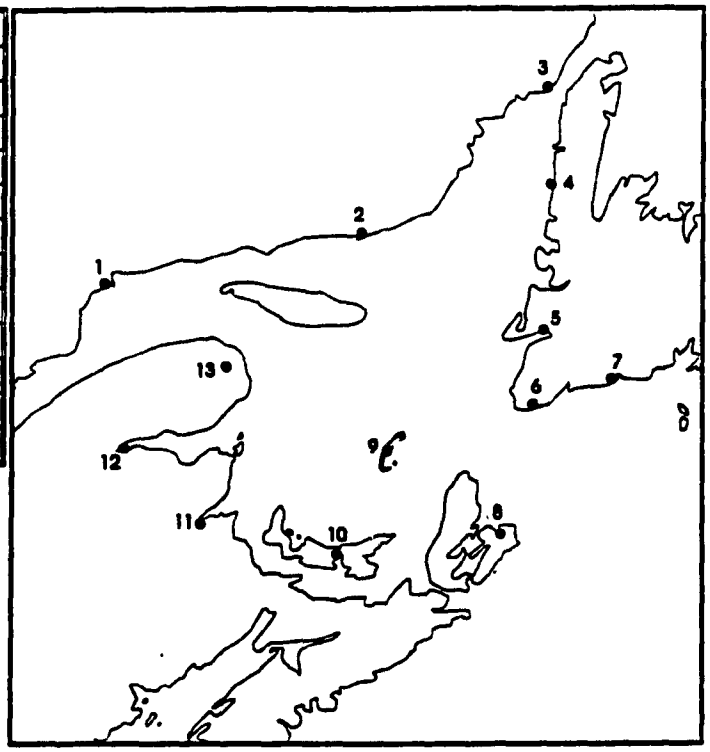

Figure 6.1 Location map of meteorological stations.

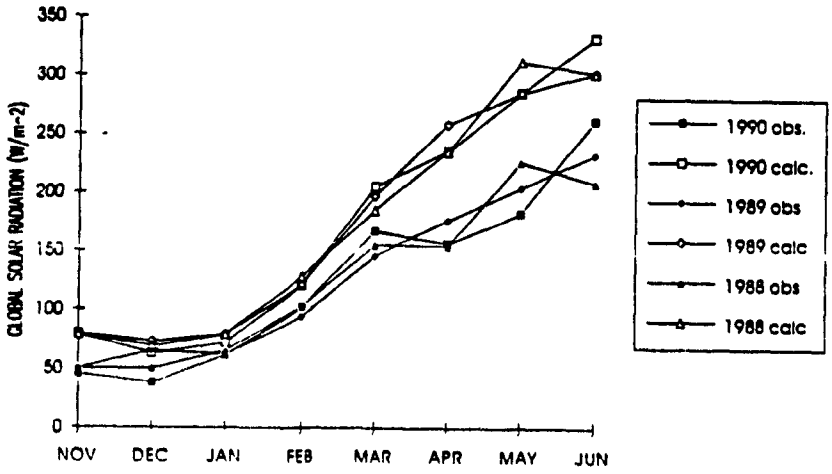

Figure 6.2 Comparison of calculated and observed incoming solar radiation at Charlottetown.

Such an influence has been documented by Herfst (1984) who observed that surface winds are orographically steered along the axis of the St.Lawrence Estuary. Headlands along the Gaspé shoreline, the west coasts of Newfoundland and Cape Breton Island must also have a strong influence on the coastal surface winds.

6.4 Solar Radiation

Incoming global solar radiation was only recorded at two stations in the study area for the years of interest. These data were obtained from the Atmospheric Environment Service of Canada. Fortunately, these two stations were Fredericton and St. John's, which straddle the Gulf.

Most ice modelling studies have used parameterizations of the solar radiation, such as that of Zillman (1972), which calculate the incoming global radiation for clear skies, and then apply a cloud correction (Laevastu 1960). This method, when tested for recent monthly averaged measurements made at Charlottetown, revealed considerable differences between observations and formula calculations (Figure 6.2) Consequently, the measured values at Fredericton and St. John's were used in an objective analysis using successive iterations with a large radius of influence (1500 km). The initial guess fields were taken from a climatological atlas of solar radiation for the decade 1967-1976 (Environment Canada 1987).

6.5 Clouds

Since measured values were used for incoming solar radiation, cloud fraction only

appears in the incoming long wave parameterization, Equation 4.12. Monthly cloud fractions from Grindstone Island, provided by the Atmospheric Environment Service, were used to represent average cloud conditions over the Gulf.

6.6 Snowcover

Values of monthly averaged snow depth were provided by the Atmospheric Environment Service, and were objectively analyzed, as described in Section 6.2, to produce spatial fields. A snow accumulation/melting rate was then calculated by taking the difference in snow depths between consecutive months.

6.7 November Sea Surface Temperature

November SST's were provided by Gary Bugden of the Bedford Institute of Oceanography. The measurements are the result of ice forecasting cruises made annually, during a ten day period near the end of November. Figure 6.3 shows the positions at which soundings were taken. The lack of measurements outside of the Cabot Strait, near the Strait of Belle Isle and in the Magdalen Shallows, is unfortunate.

An objective analysis was performed using decreasing radii of influences of 3000, 1500, 750, and 375 km, and climatological November water temperatures (Weiler and Keeley 1980) were used as the initial guess field. This analysis removed much of the small scale temperature variability from areas in which a high density of soundings were taken, such as in the Cabot Strait. The average error between the objectively analyzed and observed SST's was approximately 1 degree Celsius.

The model was initialized with the analyzed SST fields on the day corresponding to the middle of the ten day cruise. For the years 1967, 1968, and 1971 these dates were November 20, 19, and 24, respectively.

6.8 Surface Currents

Ocean surface currents were taken from a diagnostic model, driven by monthly averaged three-dimensional density fields (C. Toro, 1991). The estimated error of these calculated currents is 2-4 cm/s. The major features of the circulation are a cyclonic eddy in the northwestern Gulf, the Gaspé current, and a strong seaward flow following the Laurentian trough (Figure 6.4). Currents outside of the Cabot Strait were produced by combining the summer time diagnostic calculations of Reynaud (personal communication) with the results of Toro. The flow speeds outside Cabot Strait were taken to be the same as Toro's just inside Cabot Strait, with the main flow exiting on the southwest side of the strait, and then following the east shore of Cape Breton. A smaller current follows the south shore of Newfoundland and enters through the northeast side of Cabot Strait.

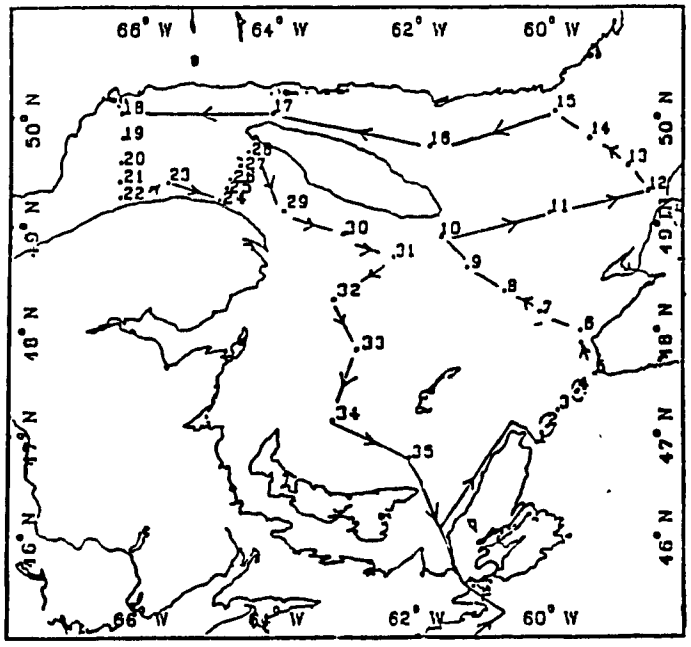

Figure 6.3 Location map of November cruise soundings. (G.L. Bugden, personal communication).

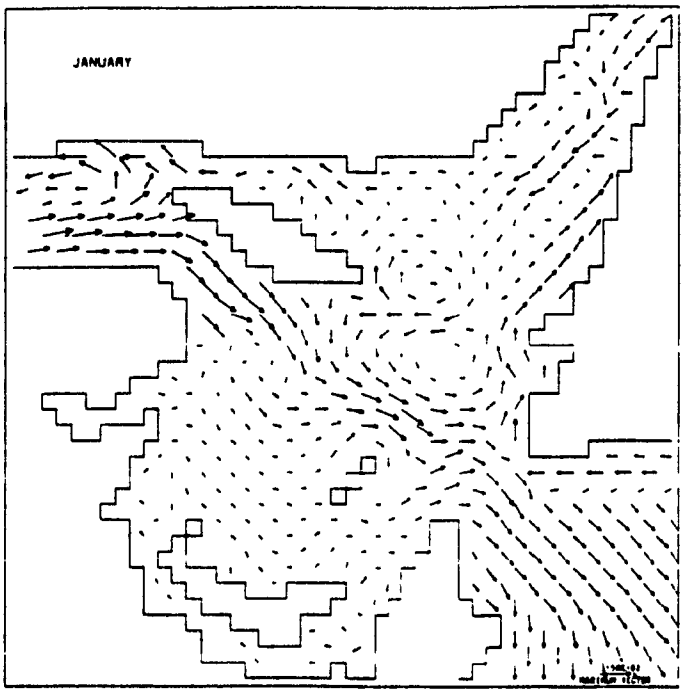

Figure 6.4 January surface currents. Units are $cm \cdot s^{-1}$.

7. Results

7.1 1968

Figures 7.1 and 7.2 show the compactness and thickness results for the 1968 simulation. Figure 7.1 may be compared with observed ice distributions and thicknesses (Department of Transport 1968, 1969; Environment Canada 1972) shown in Figure 7.3. The simulation captures the gross features of ice formation and melt, giving reasonable values of ice compactness and thickness. Ice formation begins first in the estuary and Magdalen Shallows. The ice edge, indicated by the one tenth contour, advances towards Cabot Strait. Ice compactness increases through February and March. Melt is well pronounced in April and the Gulf is essentially clear by May. The simulation has difficulty in reproducing the ice characteristics outside of Cabot Strait. The ice edge does not advance as far as observed.

In April the estuary is overly congested. This is probably caused by not including the effects of run-off, which would introduce warmer fresher water to the estuary and increased ice melt. Run-off also increases surface currents in the estuary which would increase ice advection into the central Gulf. These problems could only be resolved by using a coupled model that explicitly includes run-off.

Figure 7.2 shows the evolution of the ice thickness field. The average maximum ice thickness is about 30 cm. The thickest ice is simulated in the southern portion of the Gulf, trapped between Prince Edward Island and Cape Breton Island, and on the northwest shore of Newfoundland, due to the persistence of winter northwesterlies.

7.2 1969

1969 simulation results may be seen in Figures 7.4 and 7.5. Observations are shown in Figure 7.6. The small amount of ice observed in 1969 was caused by slightly warmer November SST's and warm winter temperatures. At Grindstone Island the mean temperature from December 1 to March 31 was 2.4°C above normal. Consequently, the simulation does produce less ice. Ice formation begins in the estuary, Magdalen Shallows and on the north shore. January, February, and March sea ice compactness correlate well with observations. In April there is residual ice in the Shallows. The residual ice in the estuary probably occurs for the same reasons as the 1968 simulation. In April and May, the simulation does not reproduce the ice observed in the northwest Gulf which resulted from advection through the Strait of Belle Isle.

The ice thickness is generally less than 10 cm, which agrees with observations. The maximum average modelled ice thickness is 15 cm.

7.3 1972

Simulation results are shown in Figures 7.7 and 7.8. A comparison with observed ice compactnesses (Figure 7.9) again shows a rough agreement. The severe ice conditions in 1972 were caused by slightly colder November SST's and cold winter temperatures. At Grindstone Island the mean temperature from December 1 to March 31 was 3°C below normal. Modelled January conditions show the ice edge advancing towards Cabot Strait. Ice concentration continues to increase until mid-March at which time the Gulf is nearly covered. In April, ice concentrations are still high, especially in the Shallows, leading to

the persistence of low ice concentrations in May, as observed.

Differences between simulated and observed compactnesses are similar to those for previous years. The ice edge is too slow in reaching Cabot Strait, and ice formation outside the Strait is almost non-existent. There is also too much ice in the estuary in April and May. The problems in simulating the ice edge could be caused by the simple representation of the mixed layer, i.e. ice is not allowed to exist unless the mixed layer is at the freezing point. Lack of SST data in this area also implies that the values produced by the objective analysis may be too close to climatological values, hence too warm.

The simulated ice thicknesses (Figure 7.8) indicate an average maximum thickness of 30-35 cm, which is slightly higher than that of 1968. Ridged ice of greater thickness is found in the Shallows, and off the coast of Newfoundland. In April and May, the ice is too thick in the northeast Gulf. It is expected that ice might be overestimated along the western shore of Newfoundland, because the inflow of warm salty Atlantic water through the northwestern side of Cabot Strait is not included in the un-coupled model. Observations indicate that the thickest spring ice was located in the Shallows.

7.4 Intercomparison

Figure 7.10 shows a comparison of the domain averaged ice thickness, compactness, areal coverage, and growth for all three years. The domain averaged ice thickness is the average of the ice mass, h, over the entire Gulf, and should not be

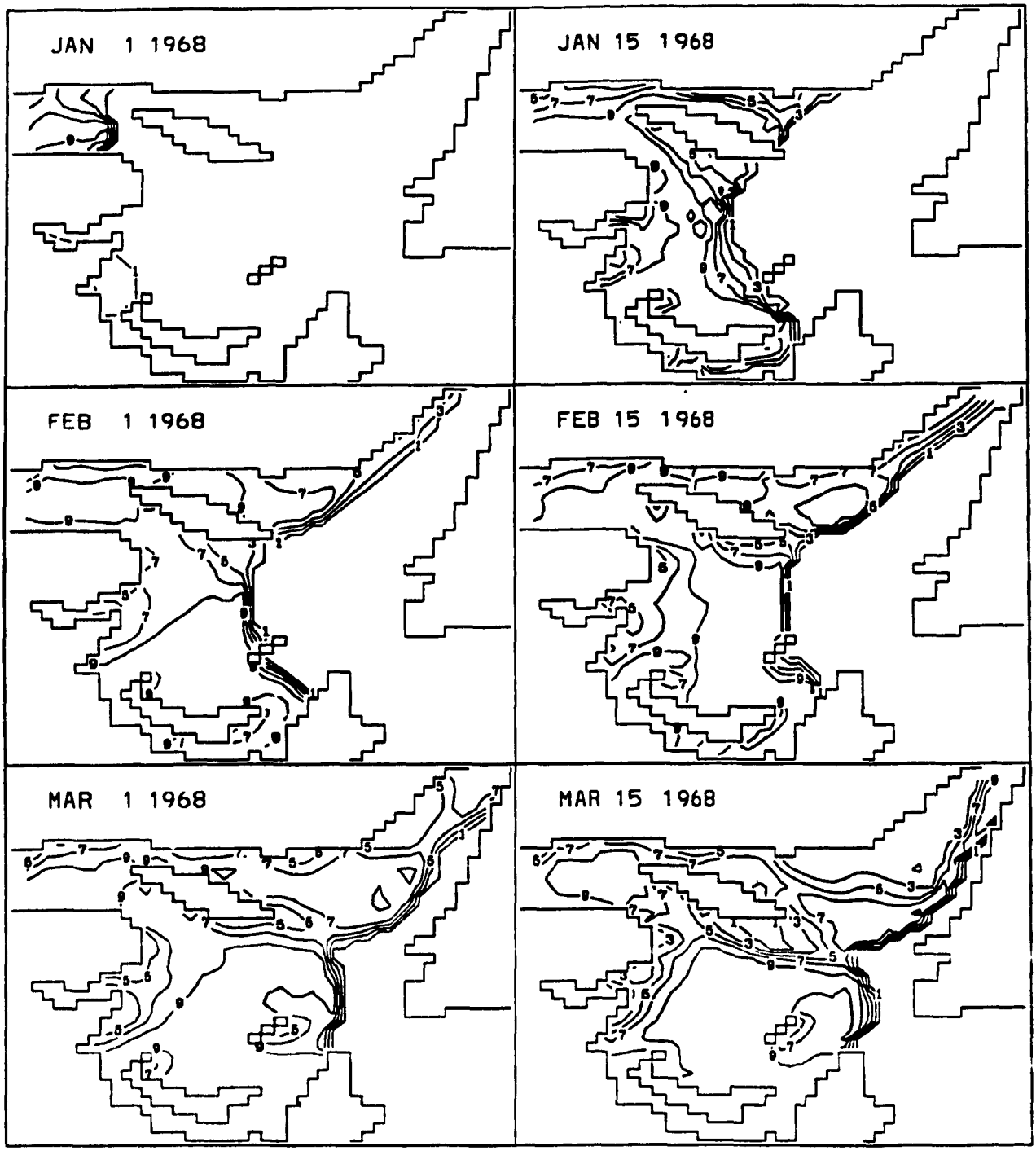

Figure 7.1 1968 ice compactness distributions.

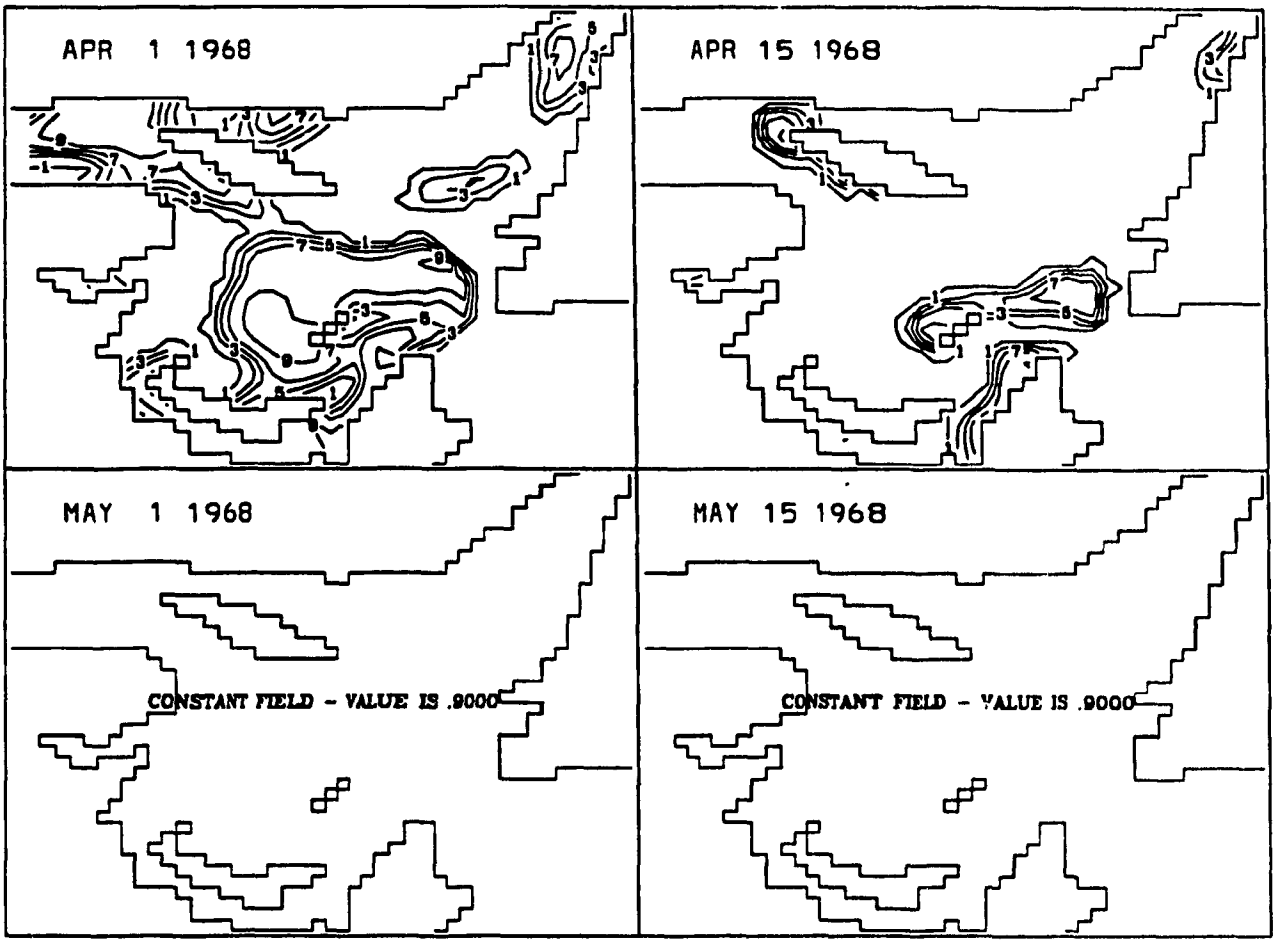

Figure 7.1 continued.

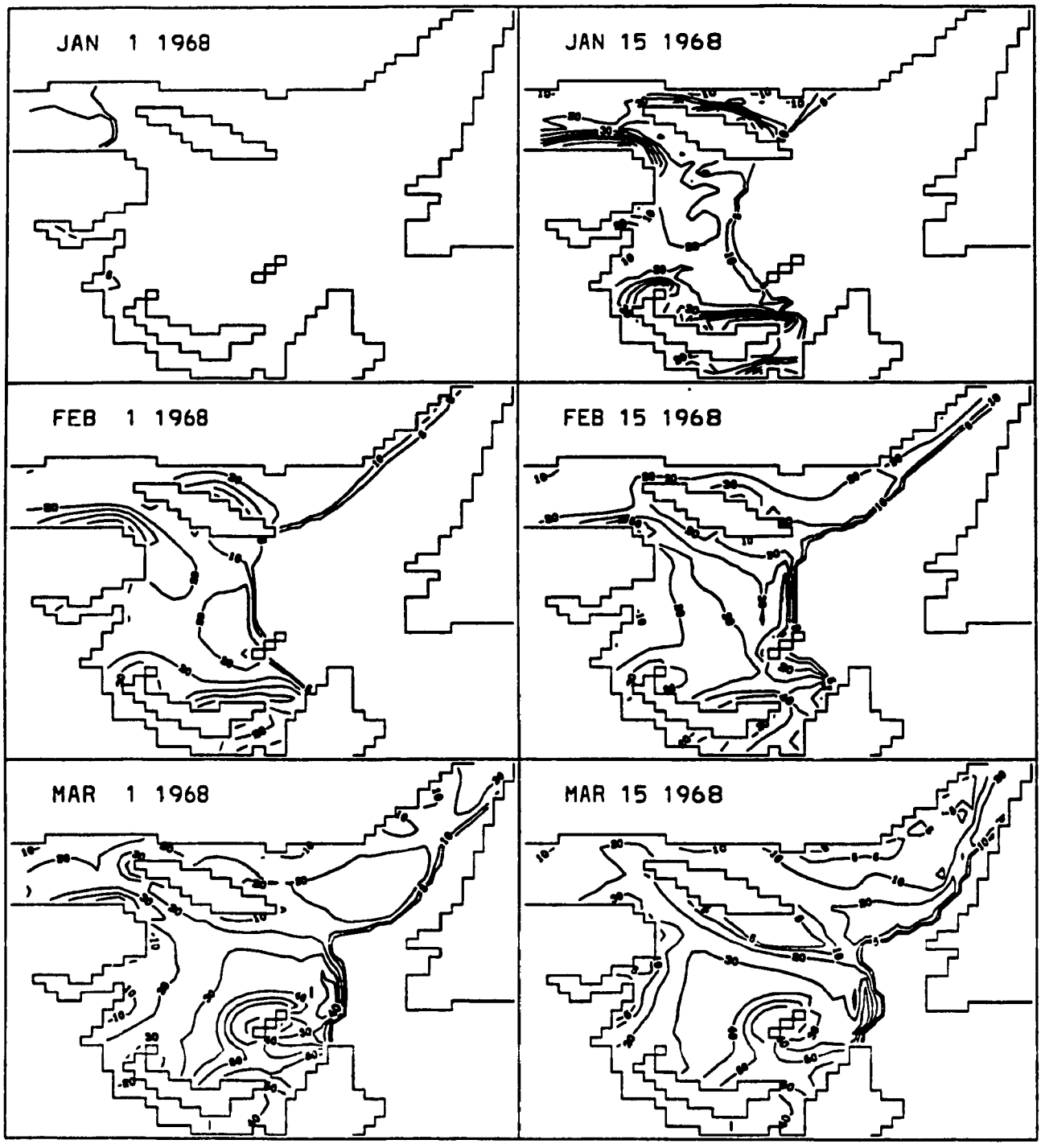

Figure 7.2 1968 ice thickness (cm) distributions.

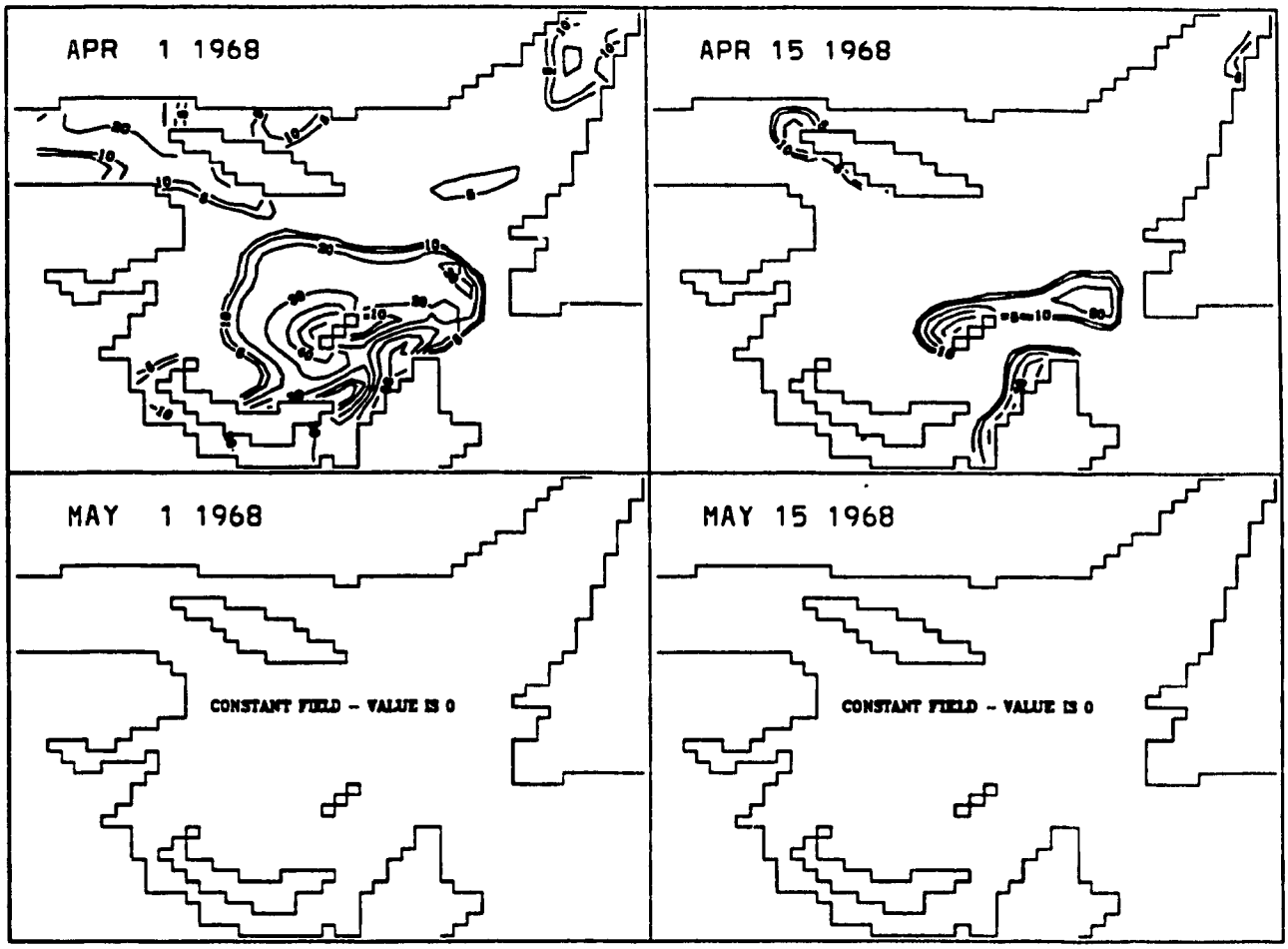

Figure 7.2 continued.

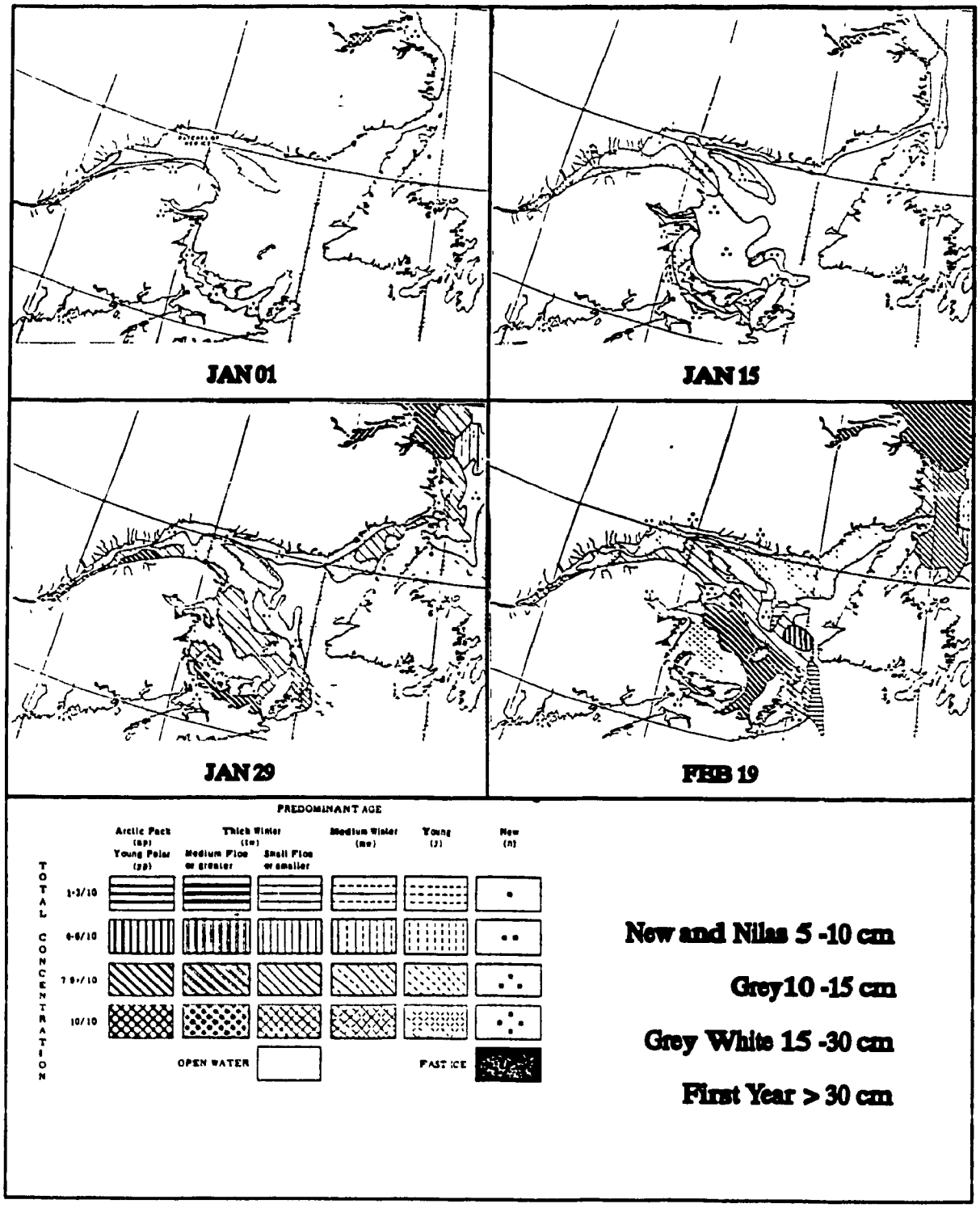

Figure 7.3 1968 observed ice compactness and thickness distributions.

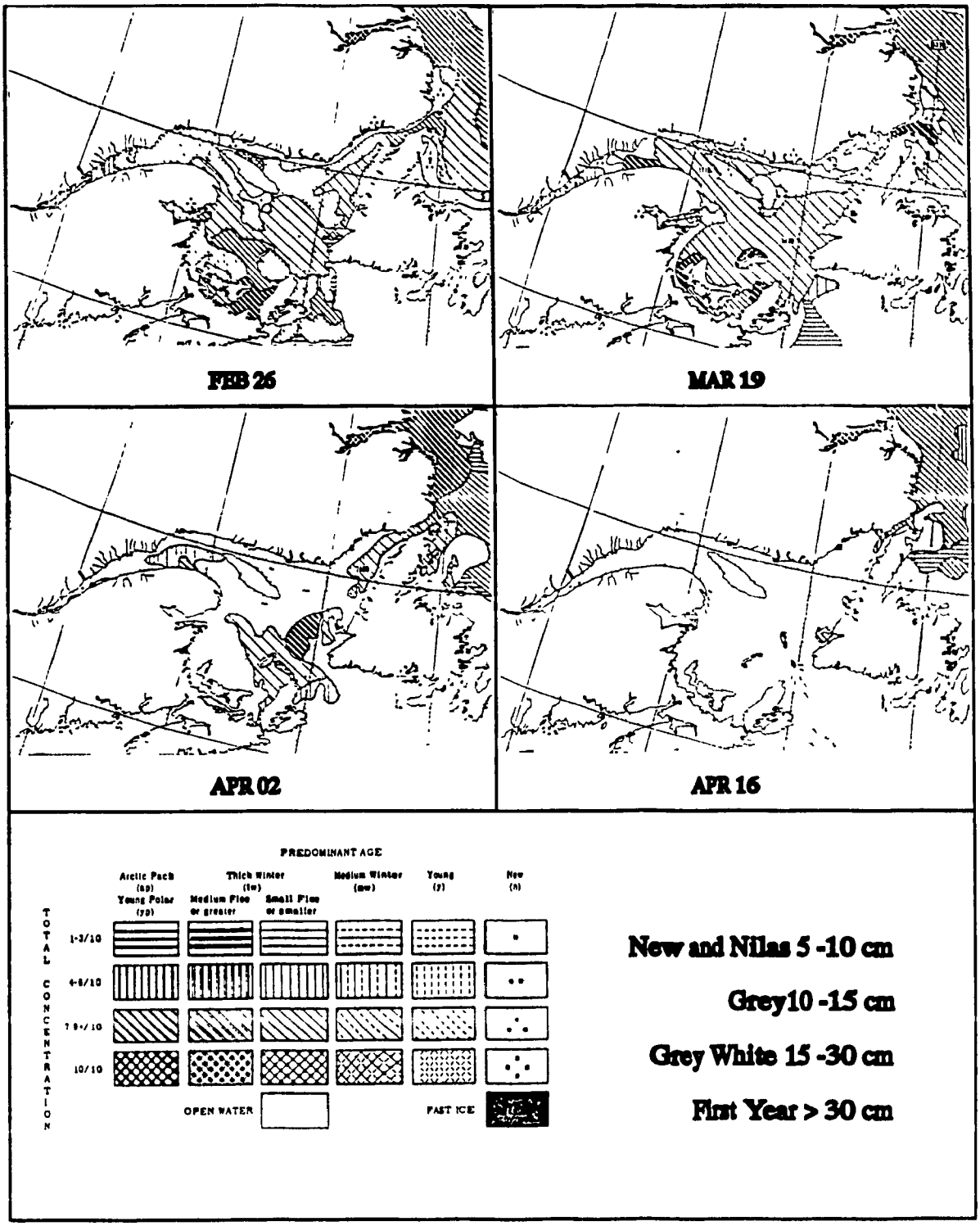

Figure 7.3 continued.

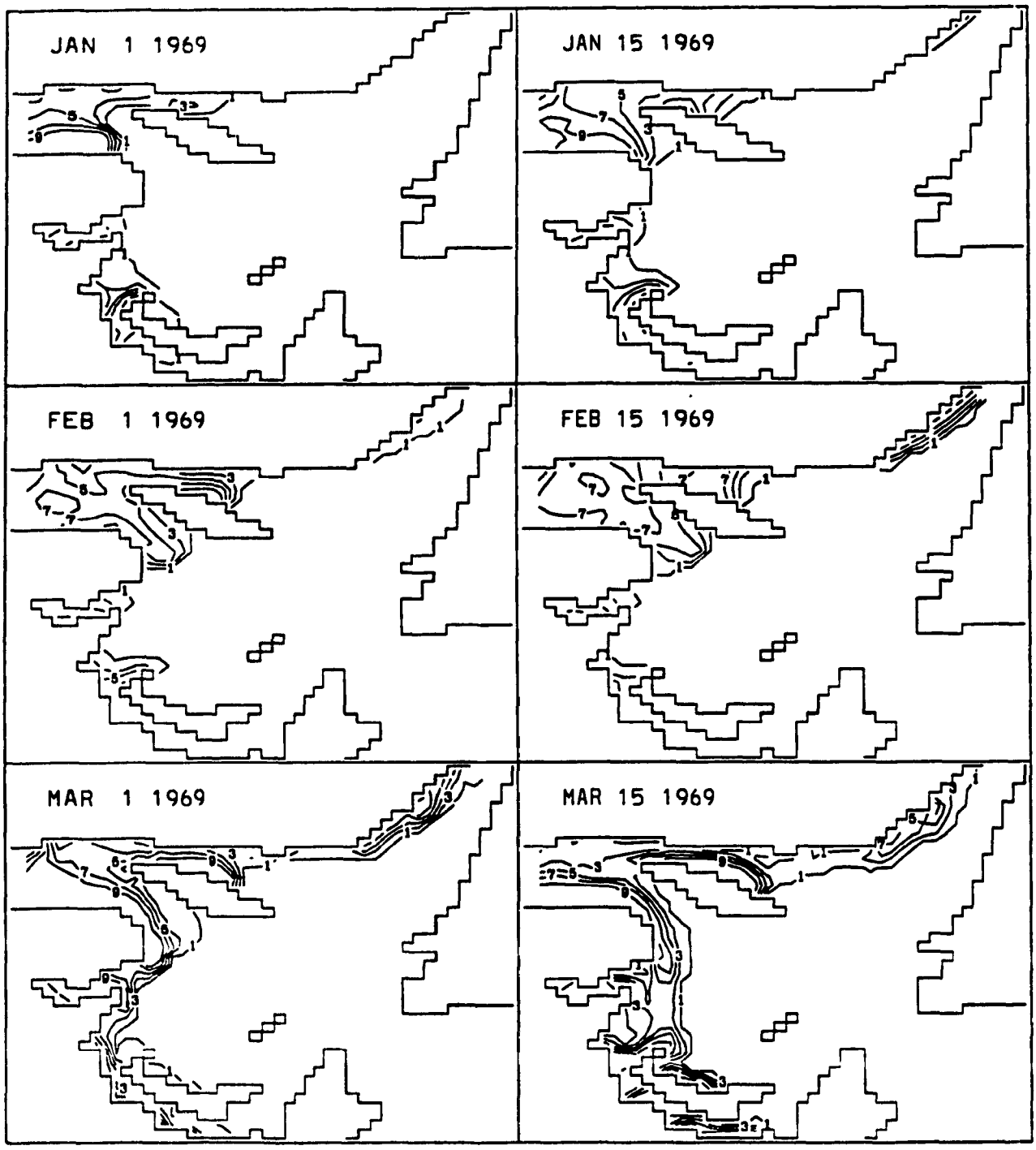

Figure 7.4 1969 ice compactness distributions.

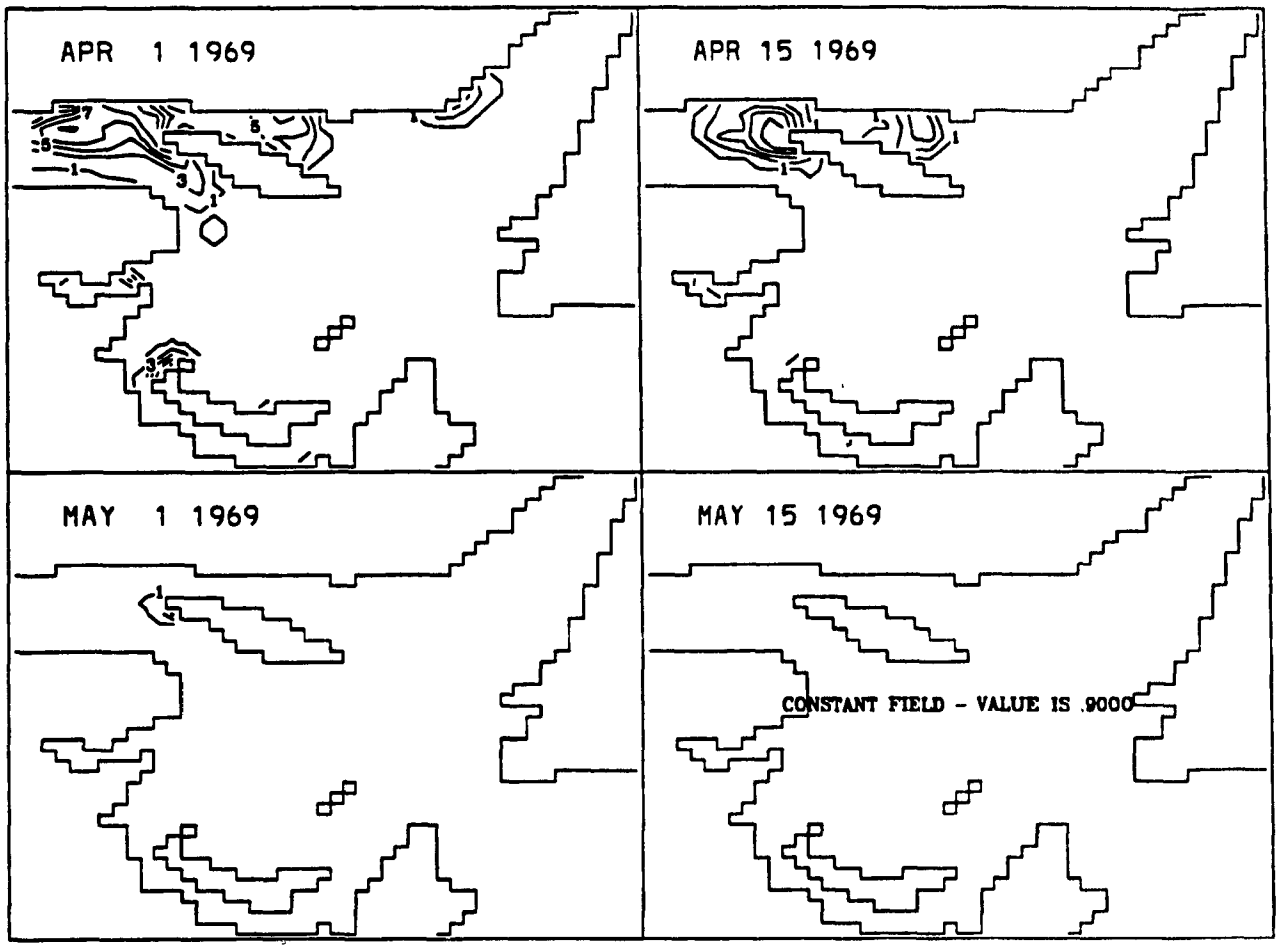

Figure 7.4 continued.

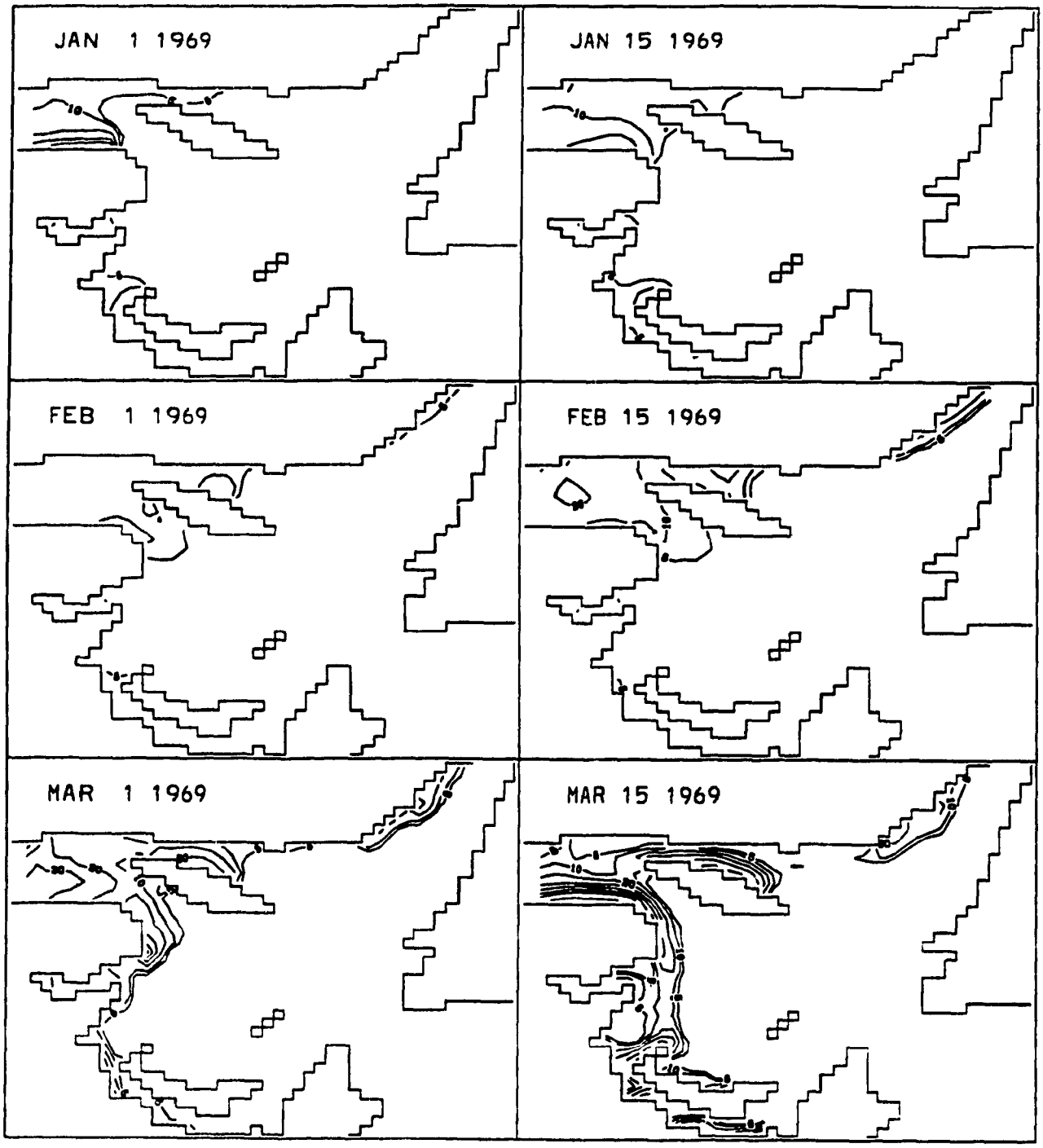

Figure 7.5 1969 ice thickness (cm) distributions.

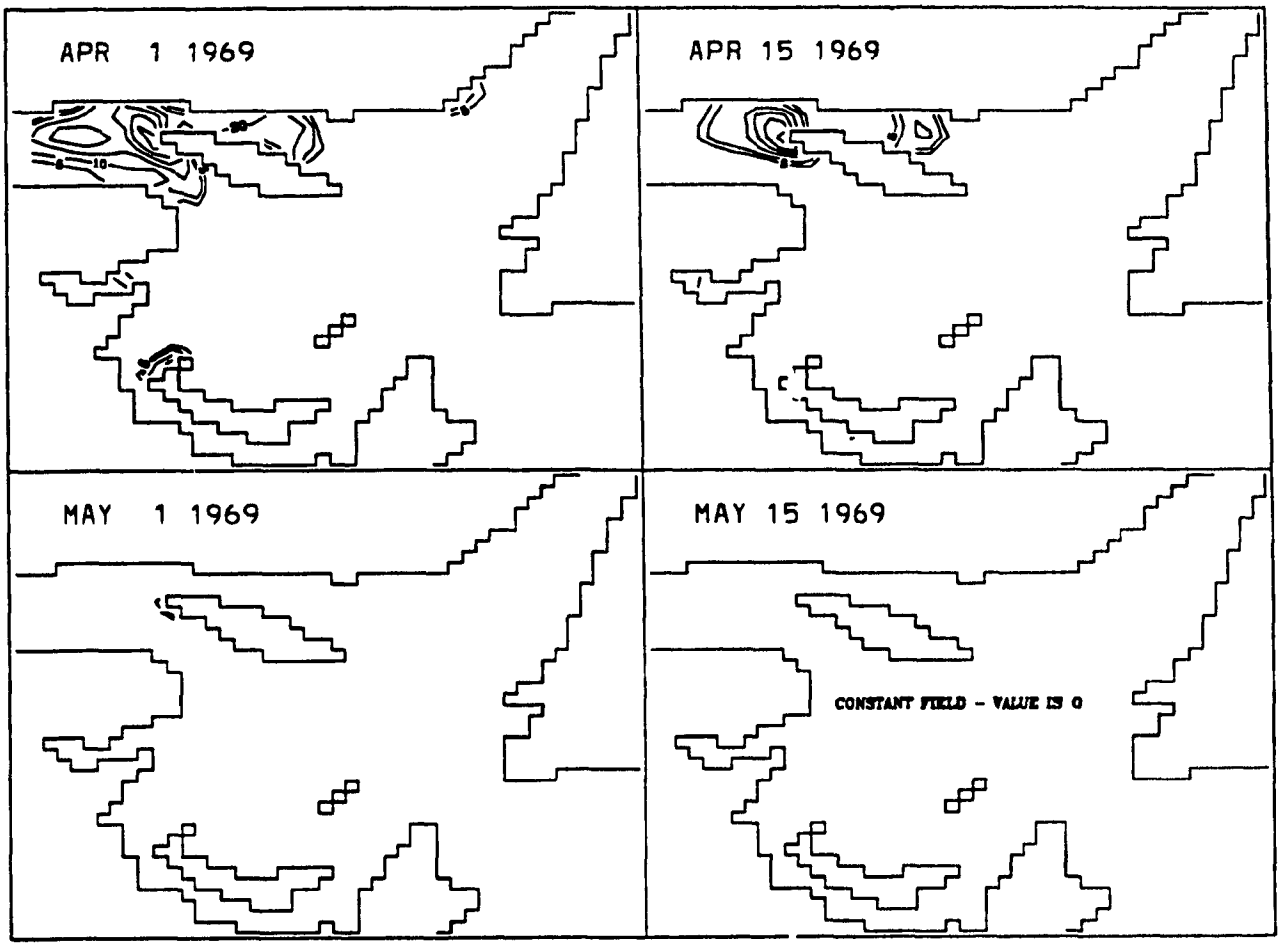

Figure 7.5 continued.

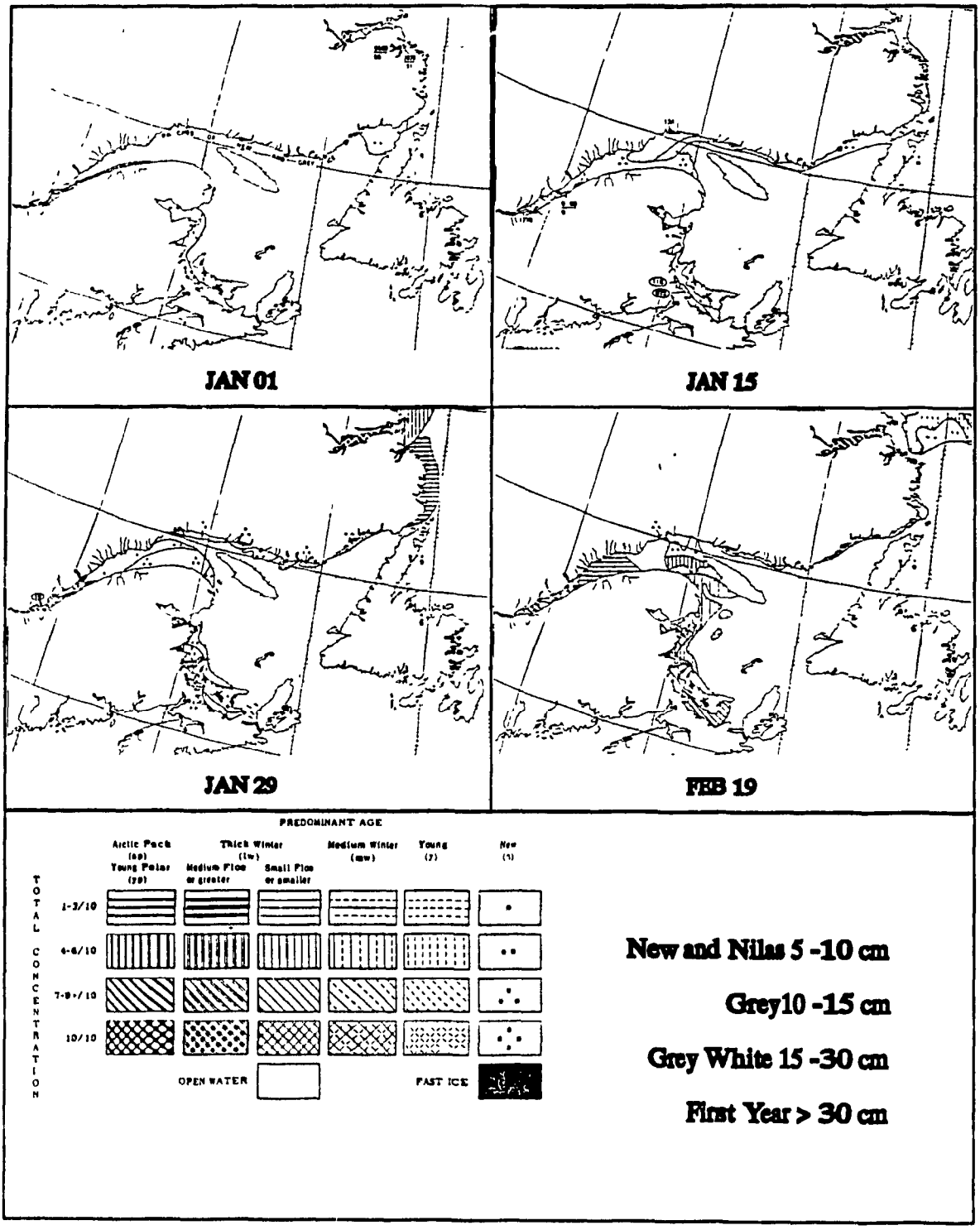

Figure 7.6 1968 observed ice compactness and thickness distributions.

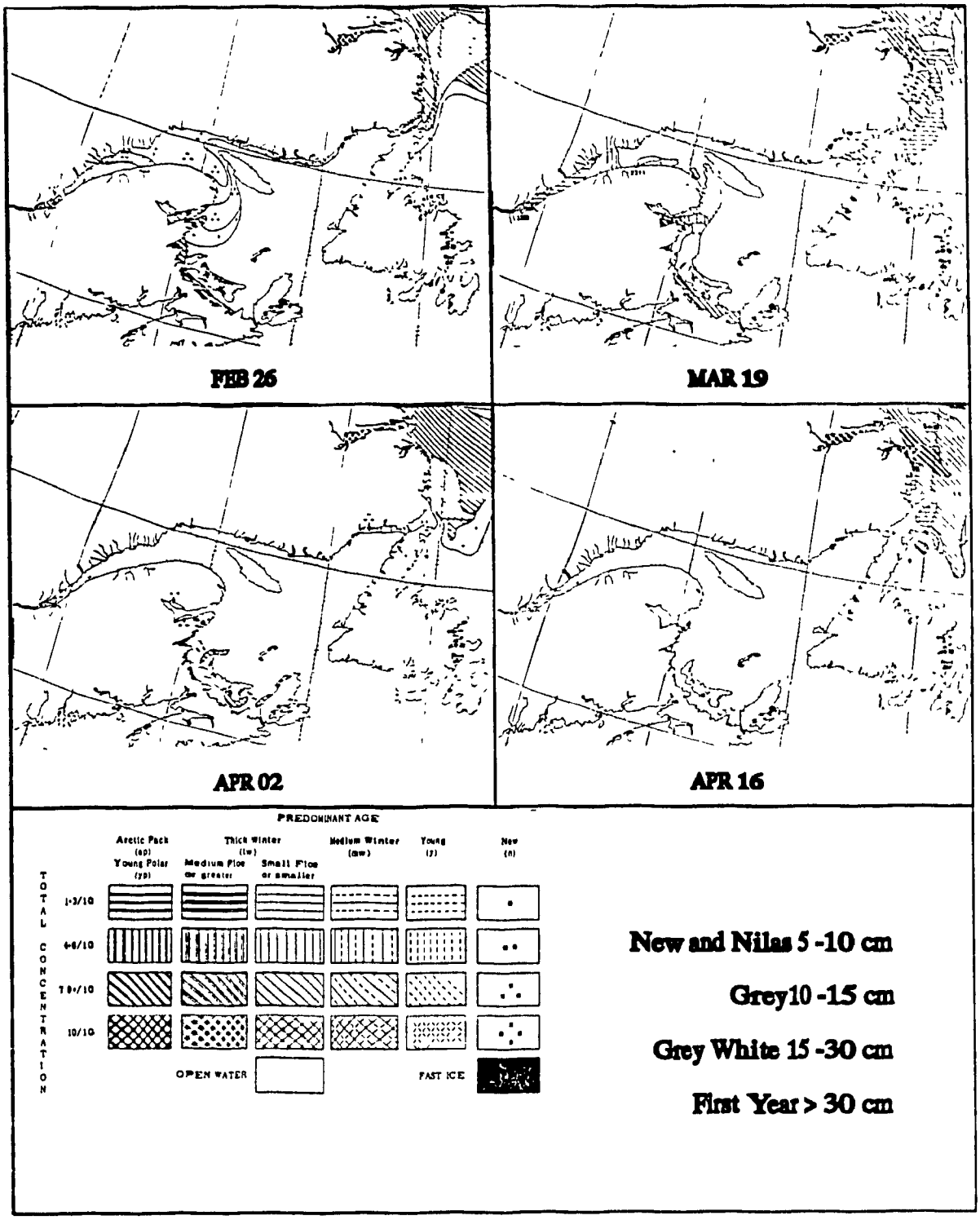

Figure 7.6 continued.

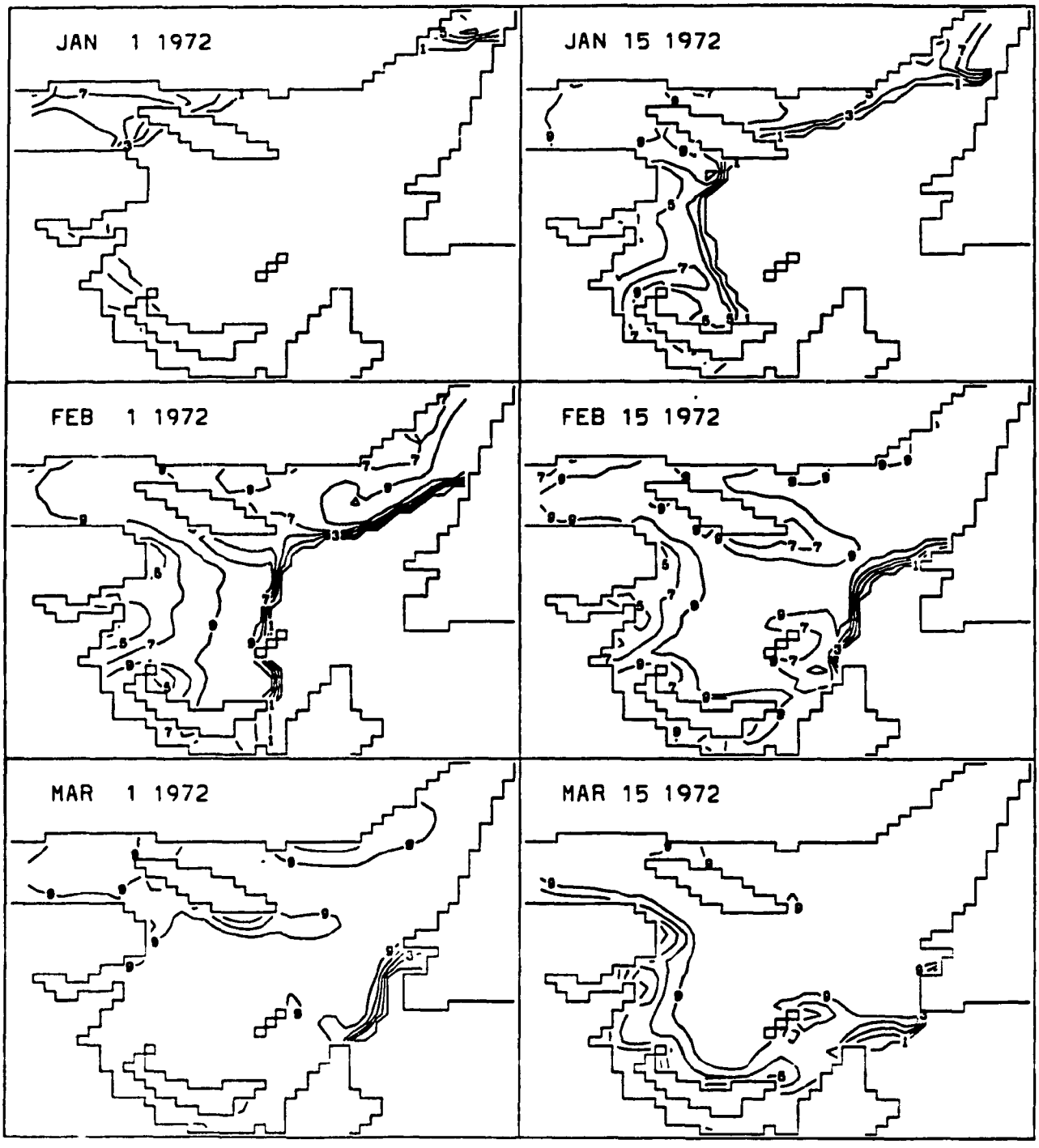

Figure 7.7 1972 ice compactness distributions.

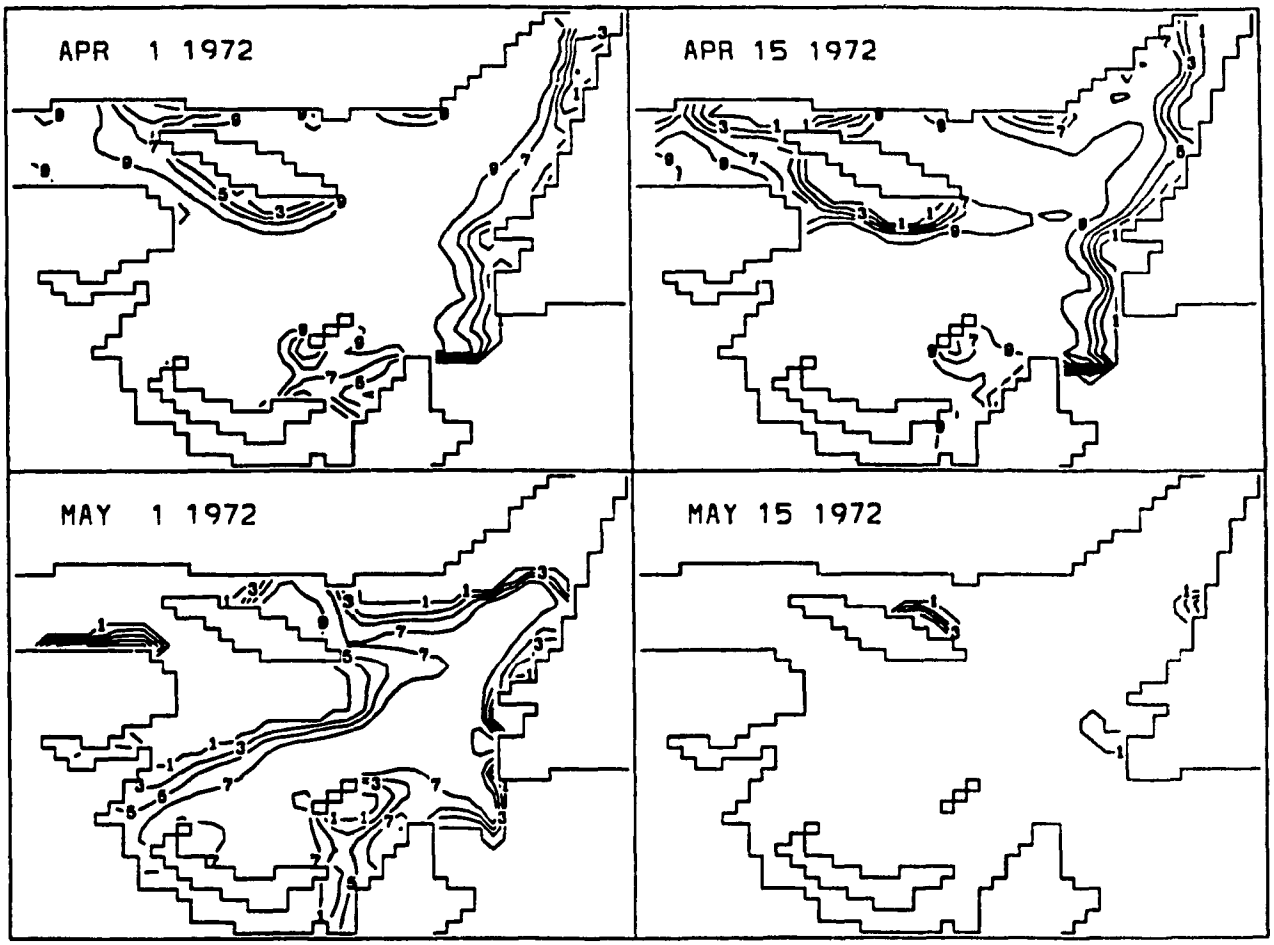

Figure 7.7 continued.

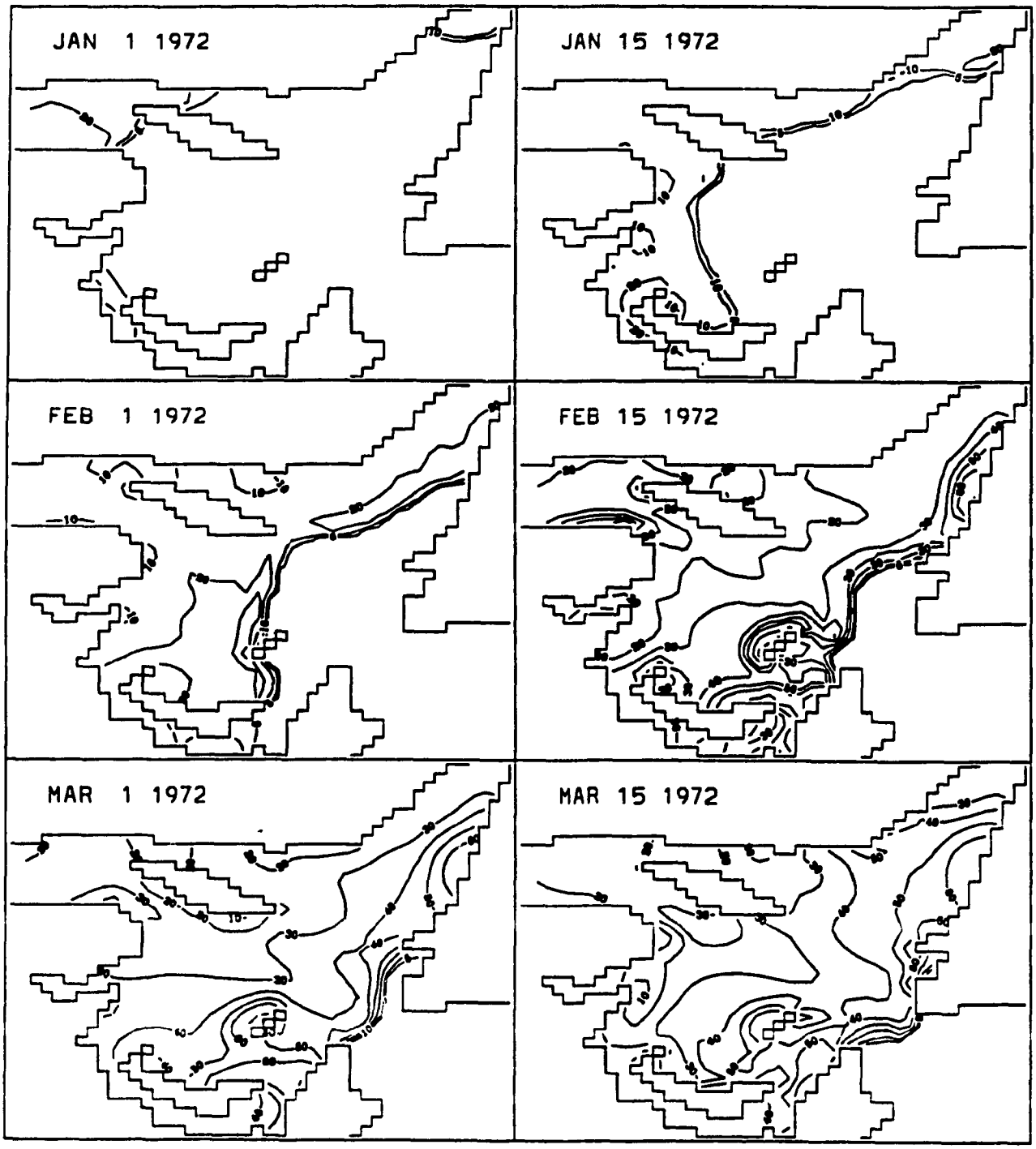

Figure 7.8 1972 ice thickness (cm) distributions.

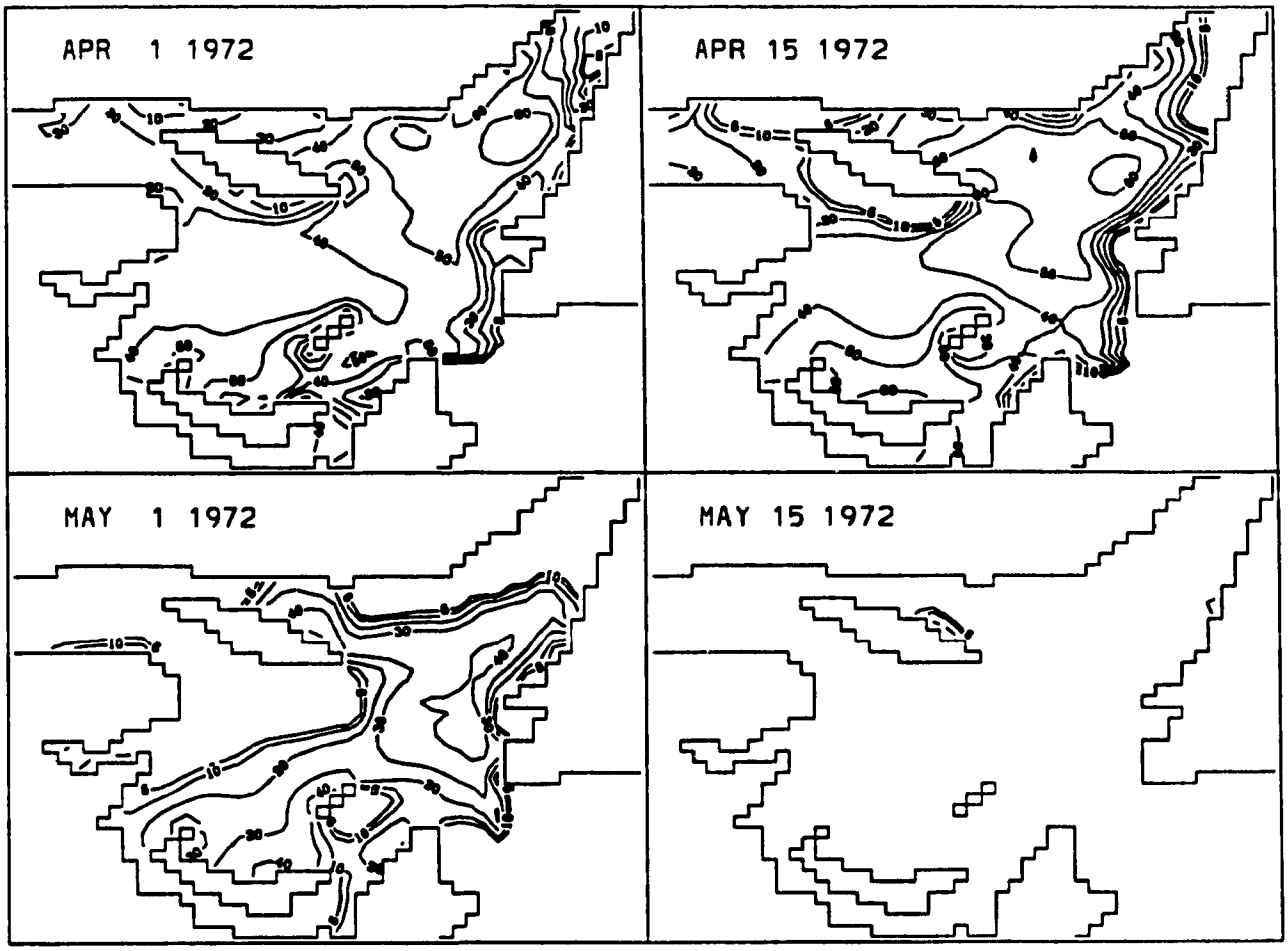

Figure 7.8 continued.

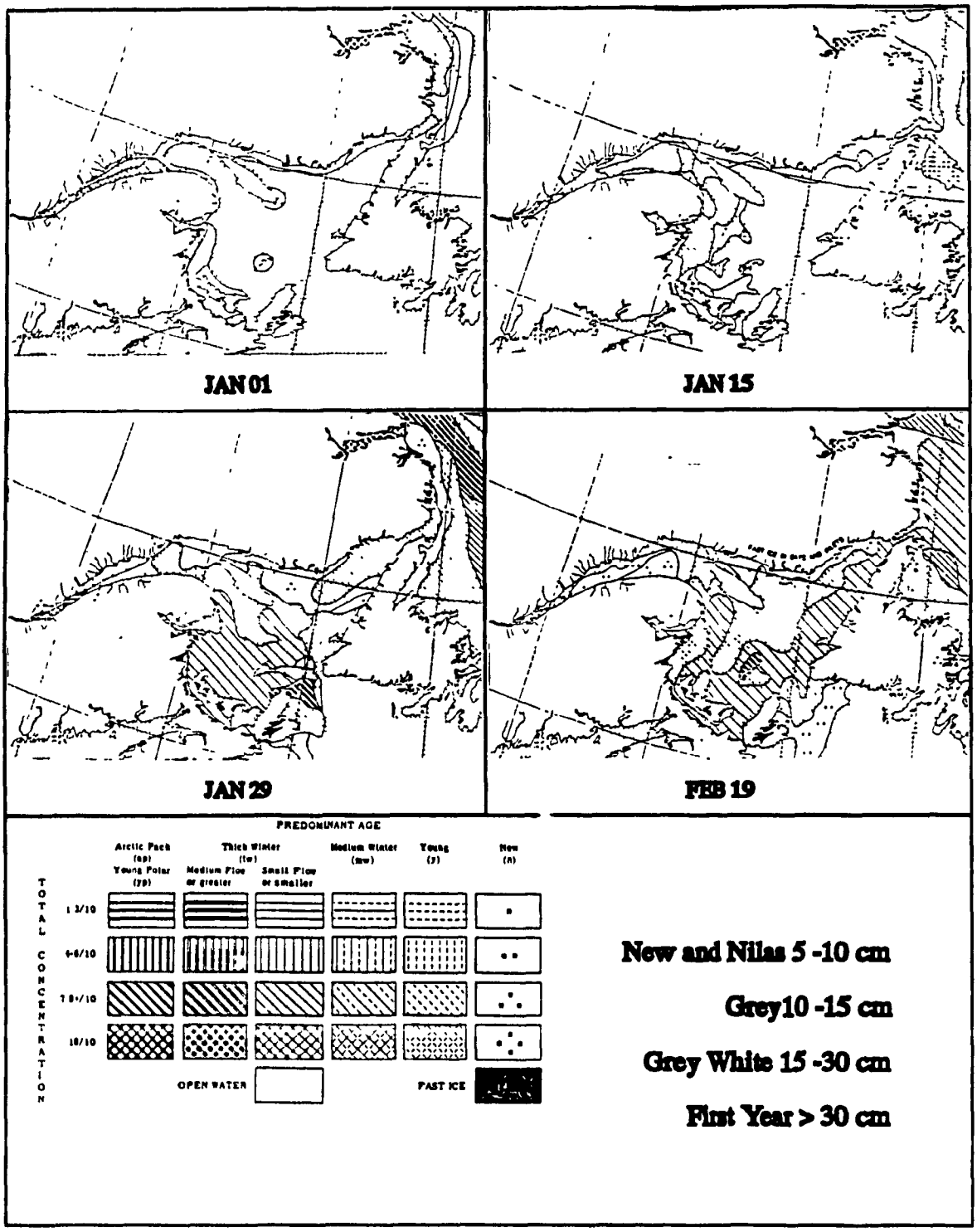

Figure 7.9 1972 observed ice compactness and thickness distributions.

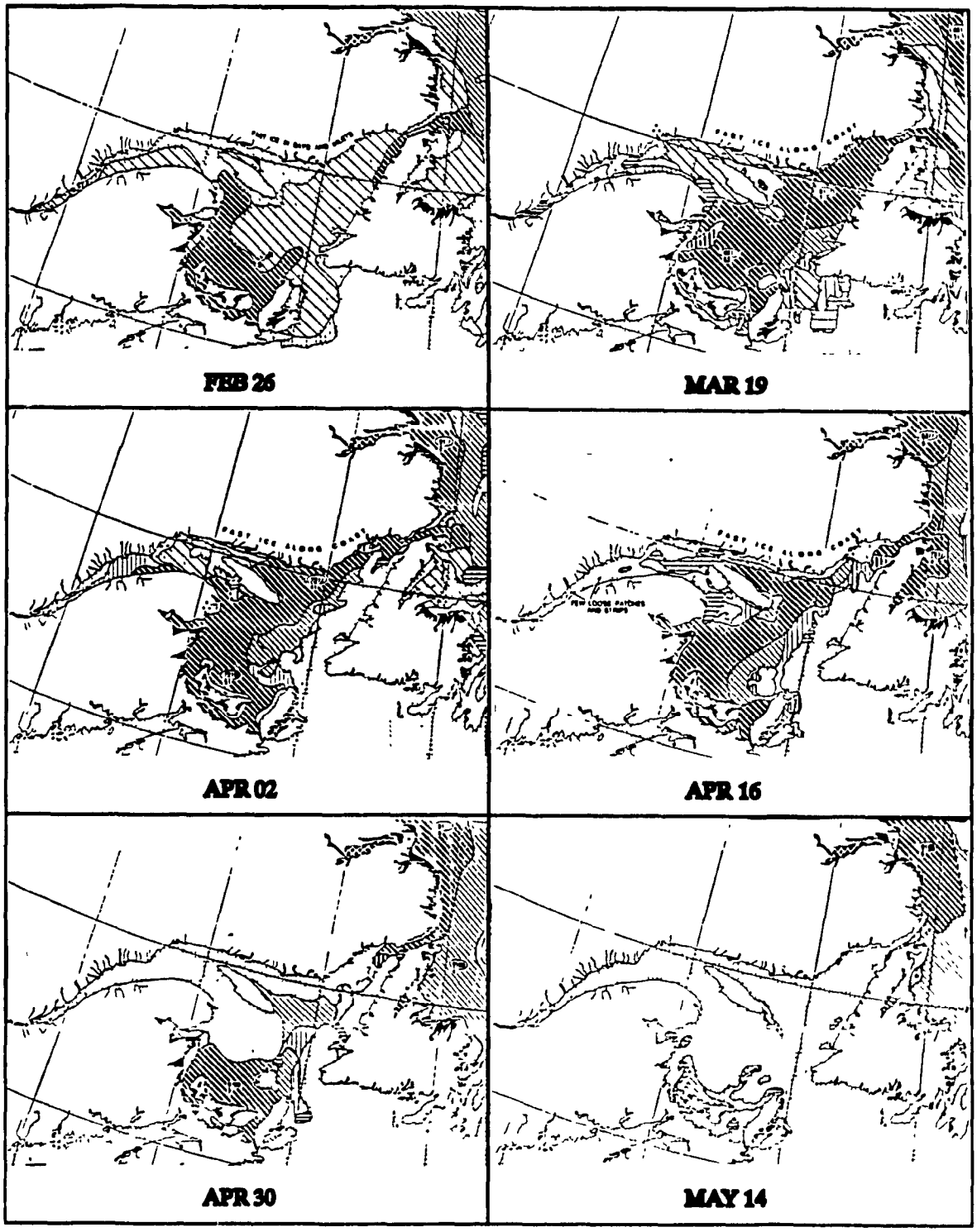

Figure 7.9 continued.

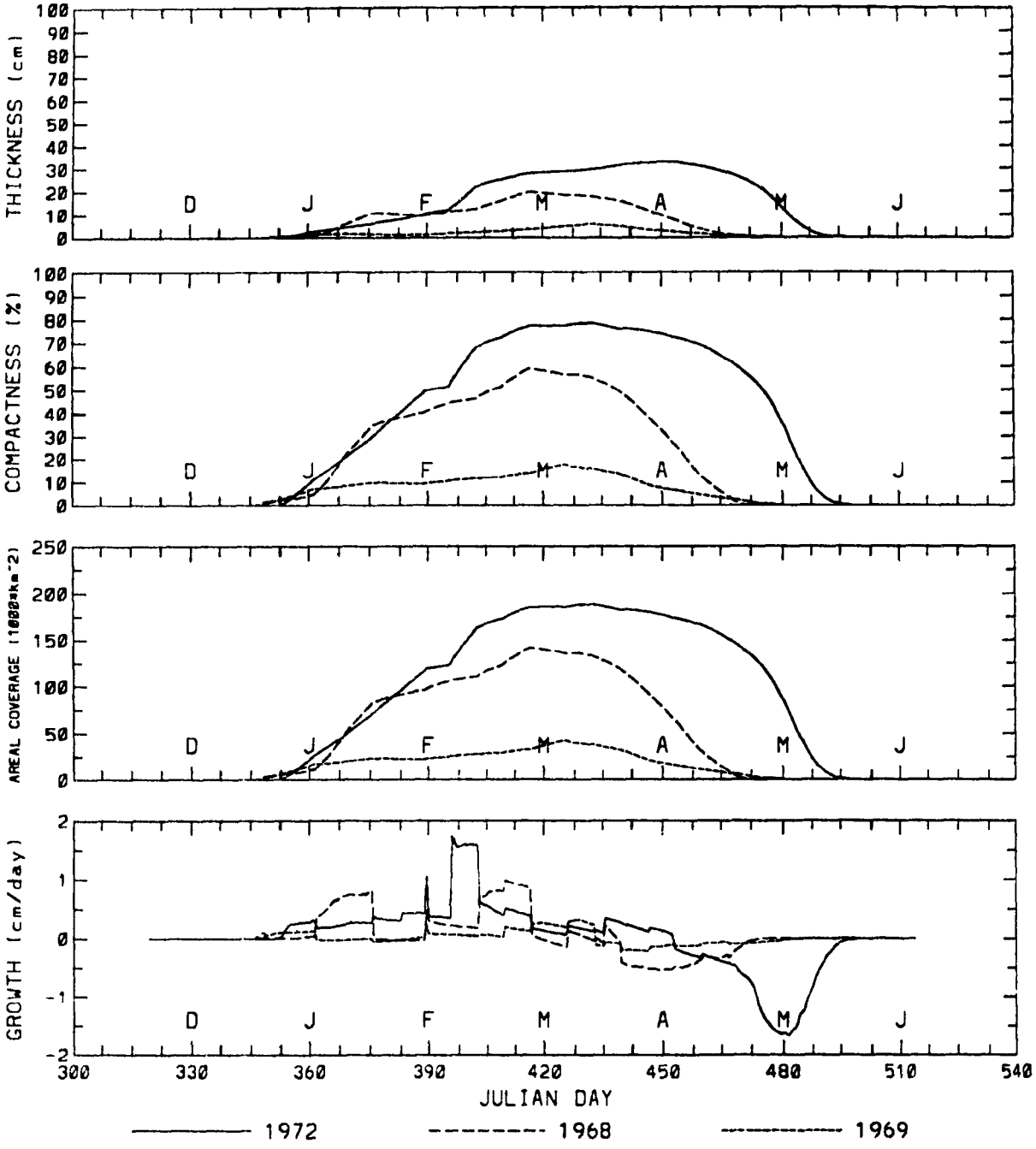

Figure 7.10 Comparison of domain-averaged characteristics

confused with the ice thickness h/A as described in Section 4.2. The letters in each frame correspond to the first day of each month (i.e. 'D' for December 1). Although 1968 and 1972 start off with similar thicknesses and compactnesses, the 1972 ice coverage grows slightly larger and persists longer due to colder than normal spring temperatures. The dates of initial ice formation all occur in mid-December. The Gulf is completely ice free by the third week of April 1968, the third week of April 1969, and third week of May 1972. These dates are all within one week of observations.

Examination of the growth rates reveals the sensitivity of growth to the atmospheric circulation over the Gulf. This is not surprising since ice growth over open water is due mostly to sensible and latent heat losses, which in turn depend on wind speed. Spring melt is caused mostly by shortwave radiation, hence the growth/melt curve becomes much more smooth.

In conclusion, the simulation did give some semblance of interannual variability. The severity of the ice cover is driven by three main factors: mixed layer depth, November SST, and winter air temperatures. The accuracy of the simulation is highly dependant on the quality of these data.

7.5 Ice Velocities

Figure 7.11 shows the weekly evolution of the ice velocity fields from January 1 to May 7 for the year 1972. The ice drift pattern changes weekly in response to the wind forcing, with maximum velocities of about 30 $cm \cdot s^{-1}$. From January until mid-February, the ice drifts predominantly in a southeasterly direction, leading to build up off

the west coast of Newfoundland and in the Magdalen Shallows. By mid-February, ice drift velocities fall in areas where increasing ice thickness and compactness tend to restrict the motion of the pack. By mid-April, the ice pack is less restricted and there is a steady drift of ice through Cabot Strait.

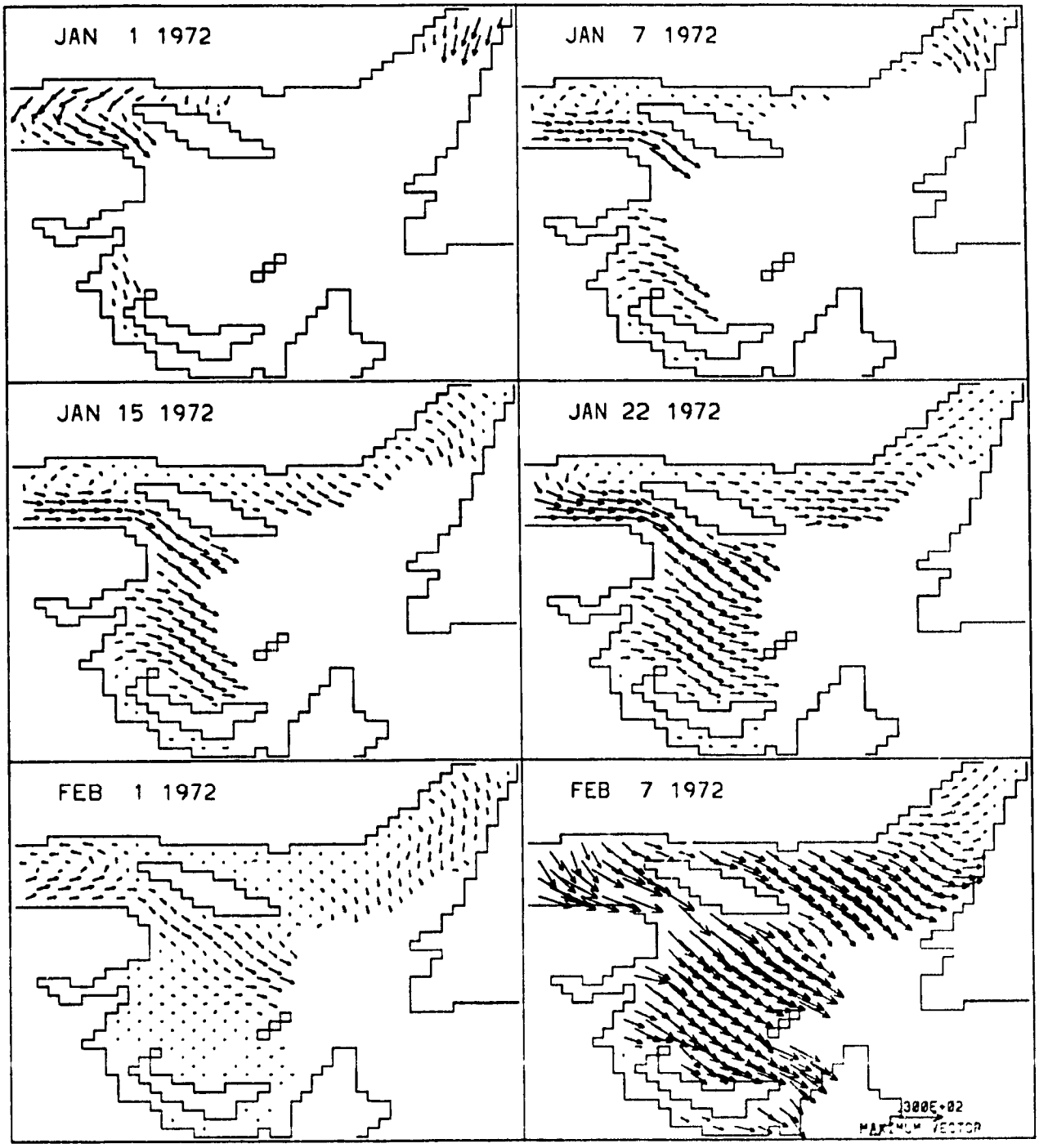

Figure 7.11 1972 ice velocity fields. The longest vector is 30 cm•s^{-1}.

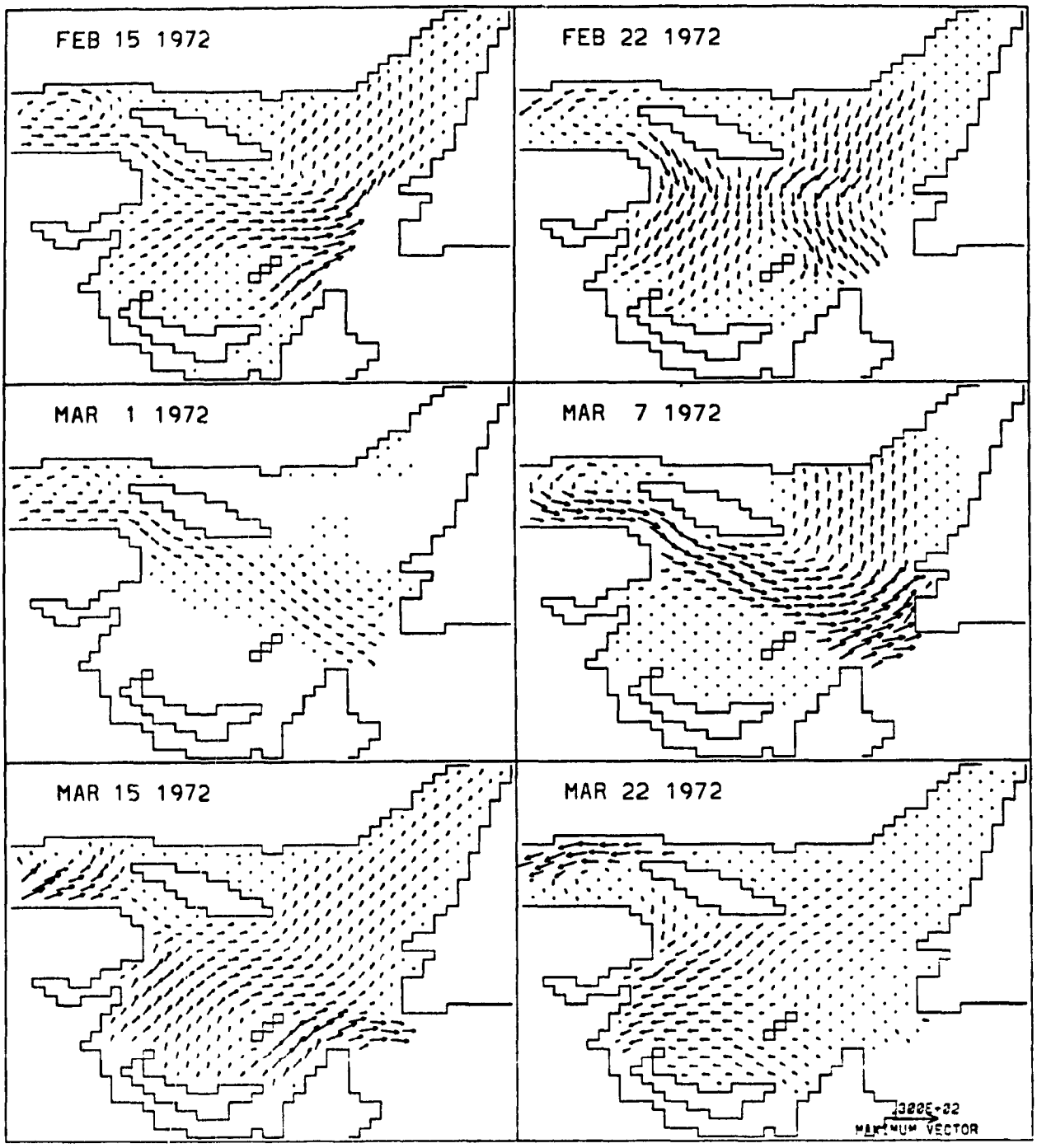

Figure 7.11 continued.

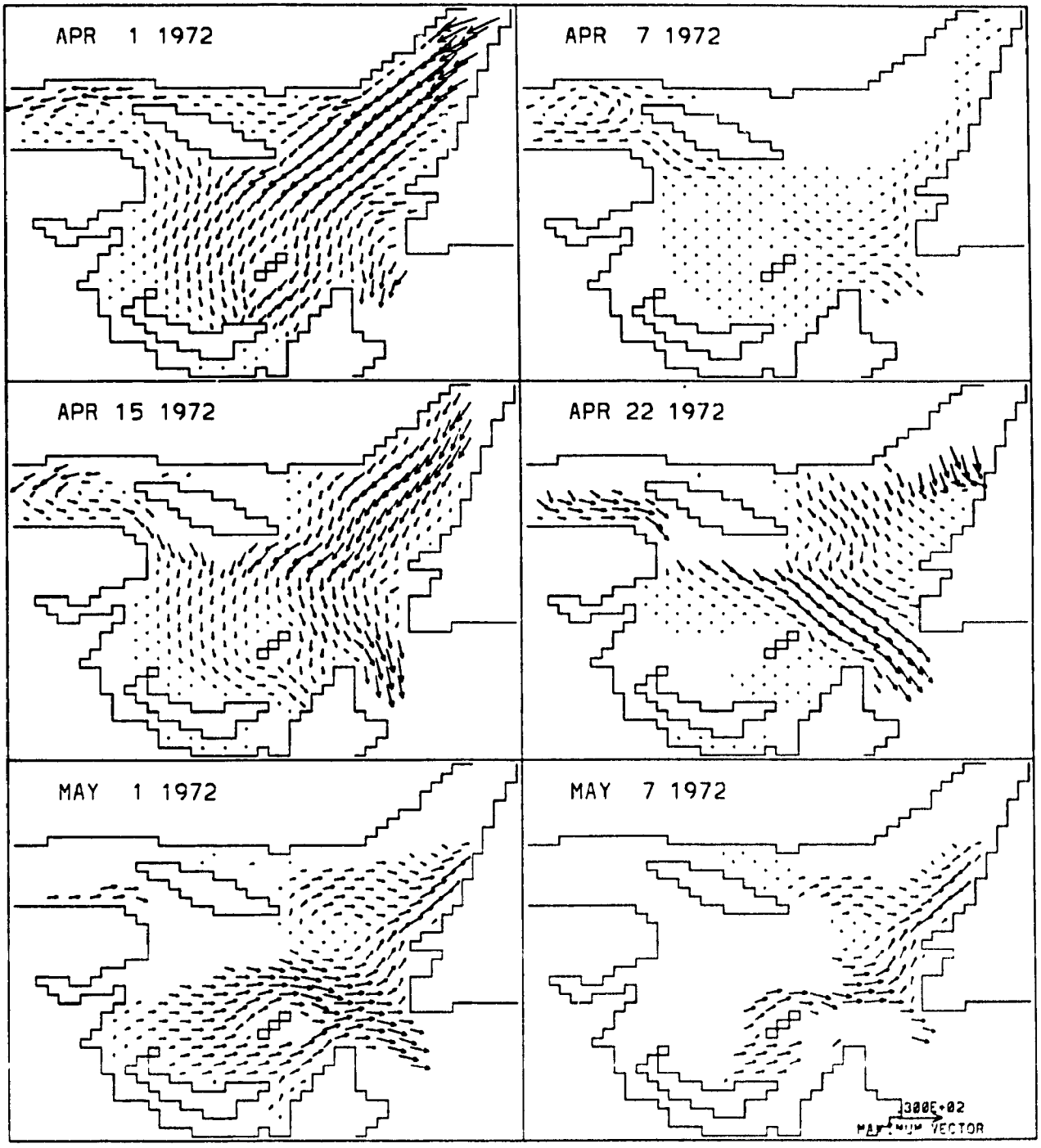

Figure 7.11 continued.

8. Sensitivity Studies

Several studies were made to examine the simulation's sensitivity to varying the forcing data and the model's free parameters. The year 1972 was arbitrarily chosen as the year on which these studies were performed. In all the following figures the curves captioned '1972' refer to the control run.

8.1 Experiment 1 - Air Temperature

In this experiment the air temperatures were varied by ±4°C over the whole domain. Reducing the air temperature by 4° increased the ice cover thickness 10 cm and the ice cover persisted well into June. Increasing the air temperature reduced the thickness by only 5 cm, with the ice clearing a week earlier (Figure 8.1).

The original air temperature forcing fields were produced by an objective analysis in which there was only one measurement in the Gulf itself, at Grindstone Island. This introduced additional error into the analysis, which was compounded by the large north-south temperature gradient that always exists across the Gulf.

8.2 Experiment 2 - November SST

The November SST's were varied by ±2°C. This altered the date of ice formation by ±1 week (Figure 8.2). The compactness and thickness during ice formation were affected, but the simulations coincided by mid-April and continued to do so until the end of the ice season. Varying the SST's in this manner introduced a ±5 cm difference in February ice thickness.

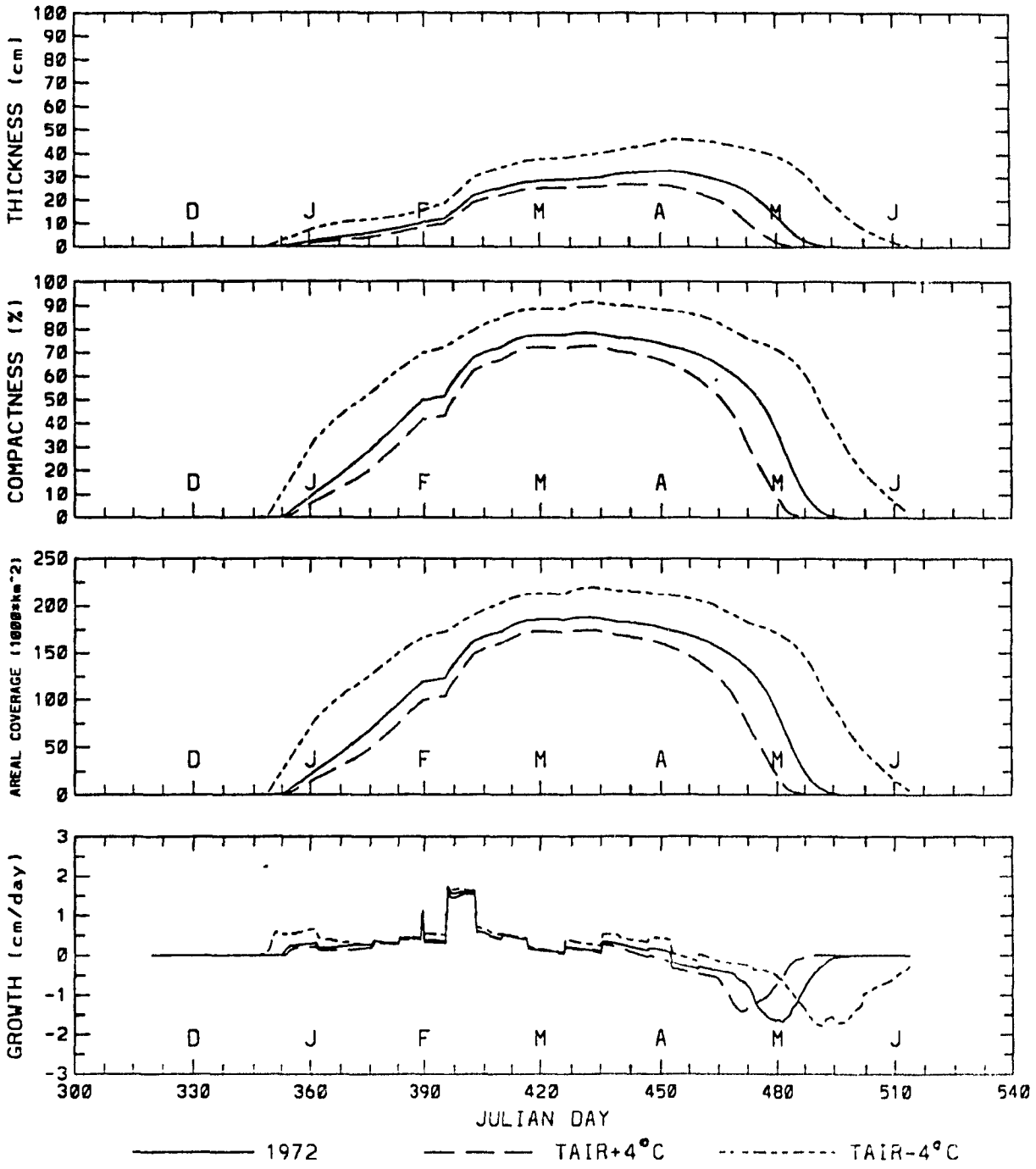

Figure 8.1 Experiment 1. Air temperature ± 4°C

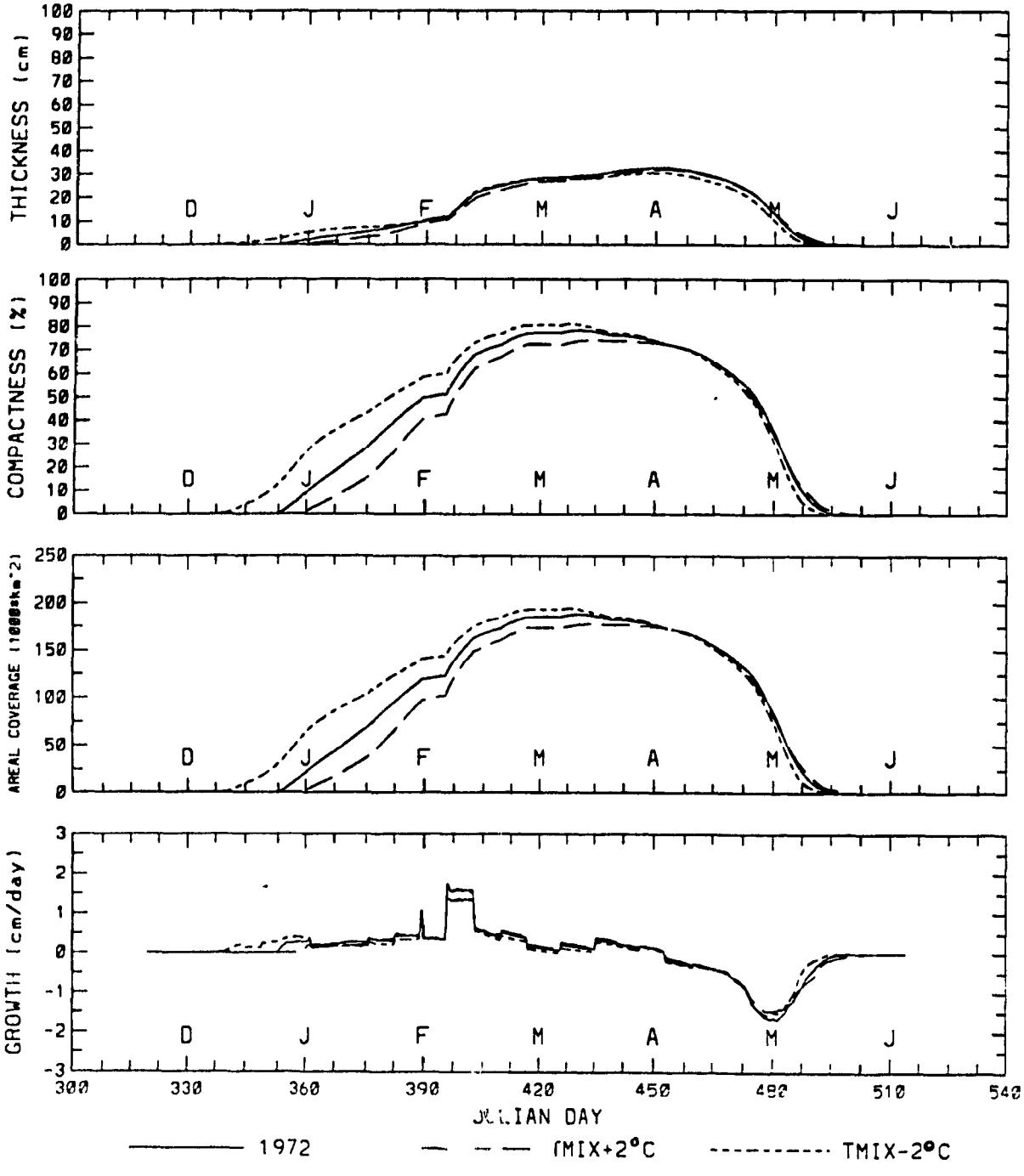

Figure 8.2 Experiment 2. November SST ± 2°C

8.3 Experiment 3 - Mixed Layer Depth

The November mixed-layer thicknesses were varied by ±5 m. As stated in Section 4.5, this was the error in estimating the mixed layer thickness based on the 10 m sampling interval of the November cruise. This affected the ice cover mostly during formation (Figure 8.3), making small variations in thickness and compactness early in the ice season.

8.4 Experiment 4 - Snowcover

The conductivity of snow is an order of magnitude less than that of ice, making snowfall an important factor in the growth of young thin ice. There is also a very large gradient of snow depths across the Gulf. In all three years considered, the stations along the north shore had maximum accumulated depths of at least 100 cm, while Grindstone Island had only 20-30 cm, and Sydney, Nova Scotia, 10-15 cm. In the first part of this experiment, the rate of snowfall was increased by 20 cm a month; in the second part there was no snow (Figure 8.4).

Changing the snowfall, did not affect initial ice growth, since this was growth upon open water, but as the ice cover matured a significant change in thickness was observed. Without a snow cover the ice was up to 20 cm more thick Increasing the snow cover resulted in a 15 cm reduction in thickness. Overall, the mid-winter growth rates were changed by ±0.25 cm/day.

The problems in representing the snow cover are illustrated Table 8.1.

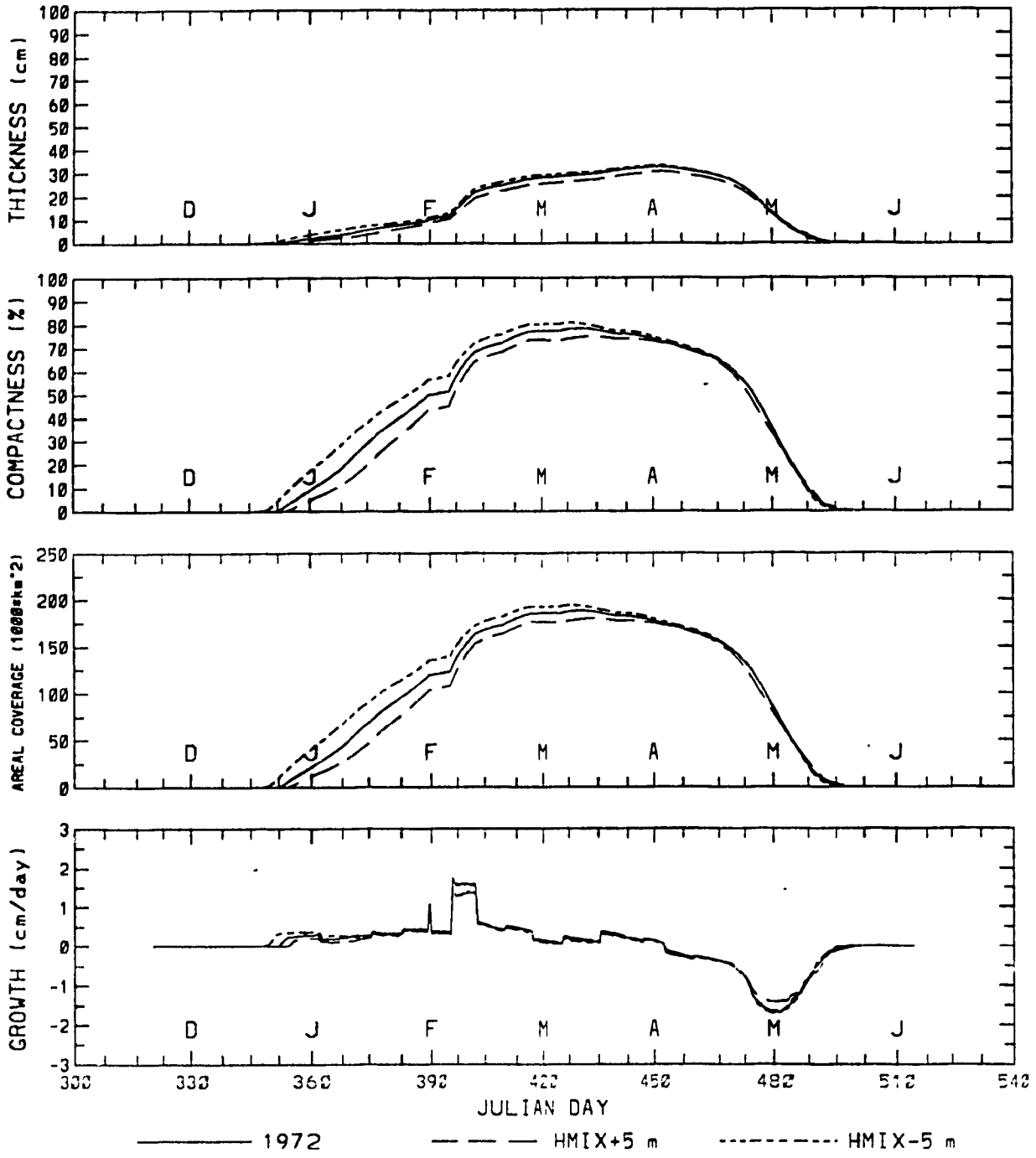

Figure 8.3 Experiment 3. Mixed layer depth ± 5 m.

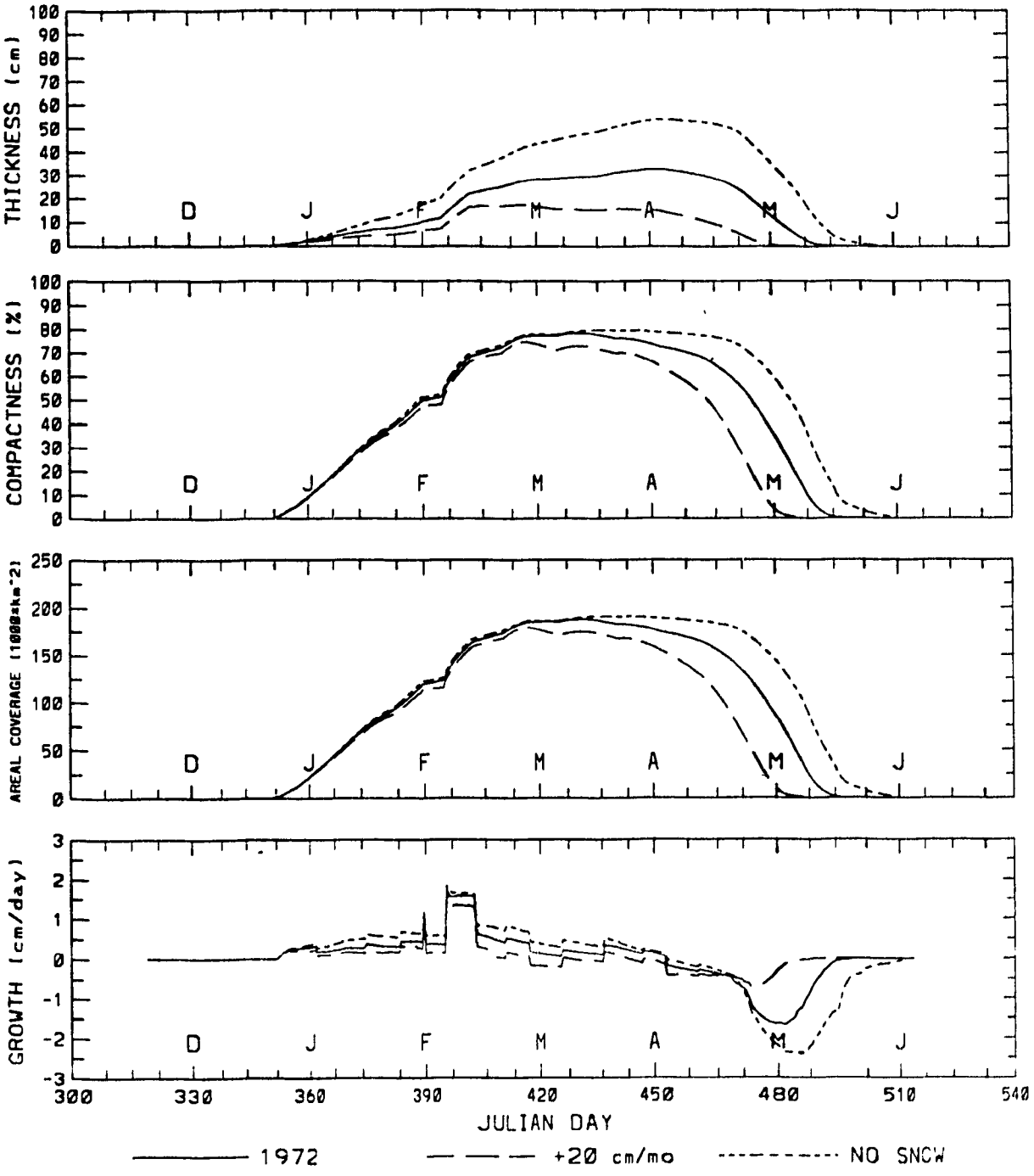

Figure 8.4 Experiment 4. Snowfall increased 20 cm/month & no snow cover.

Table 8.1

Station	Month	Precip.	Snowfall	Snowdepth
Natas.	Dec	9	84	38
Sydney	Dec	16	112	8
Nata.	Jan	8	60	113
Sydney	Jan	14	74	7
Nata.	Feb	13	87	151
Sydney	Feb	15	90	11

All measurements are in cm.

In Table 8.1 , total monthly precipitation, snowfall and average snow depth are tabulated for Natashquan and Sydney, for the year 1972. Even though Sydney received more snow than Natashquan, and had weekly average temperatures well below zero, the accumulated snow depth at Natashquan was much larger than that at Sydney.

Snow depth can not be represented by simply accumulating the measured snowfall. An 'artificial' snow accumulation rate must be calculated from measured snow depths as described in Section 6.6. Snow accumulation rates calculated from weekly averaged snow depths would be preferable.

8.5 Experiment 5 - Ocean Heat Flux

When the deep ocean heat flux was increased by 10 $W \cdot m^{-2}$, the ice thickness was decreased by about 5 cm (Figure 8.5). Without any ocean heat flux the ice thickness is increased by almost 20 cm. Deep ocean heat flux is an extremely important variable, and can only be accurately represented by a coupled model; in an un-coupled model, and without observations, this flux becomes a tuning variable to reproduce observed thicknesses. Spatial variations in the heat flux would also be important.

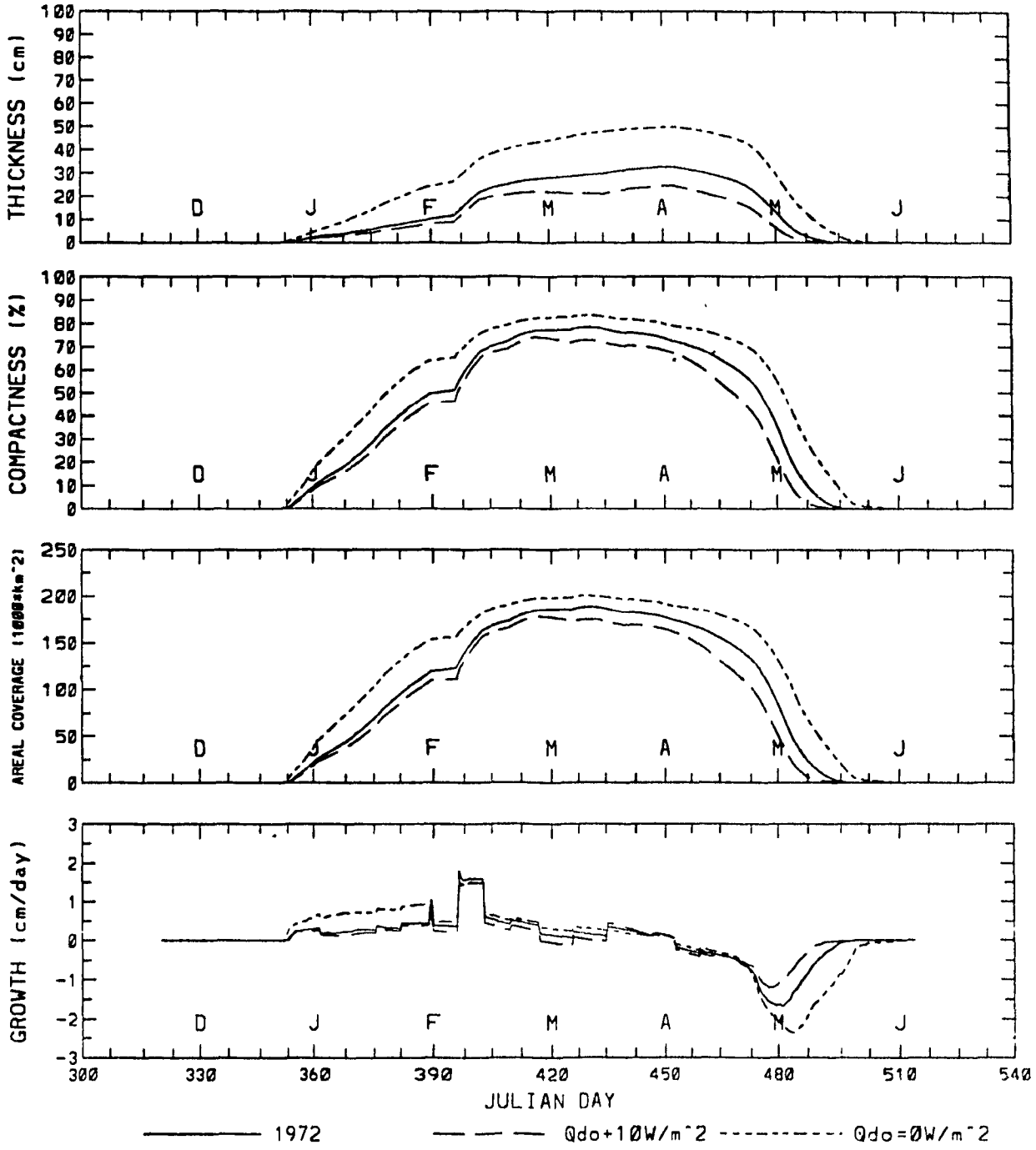

Figure 8.5 Experiment 5. Deep ocean heat flux Q_{do} + 10 W•m^{-2} & Q_{do}=0 W•m^{-2}.

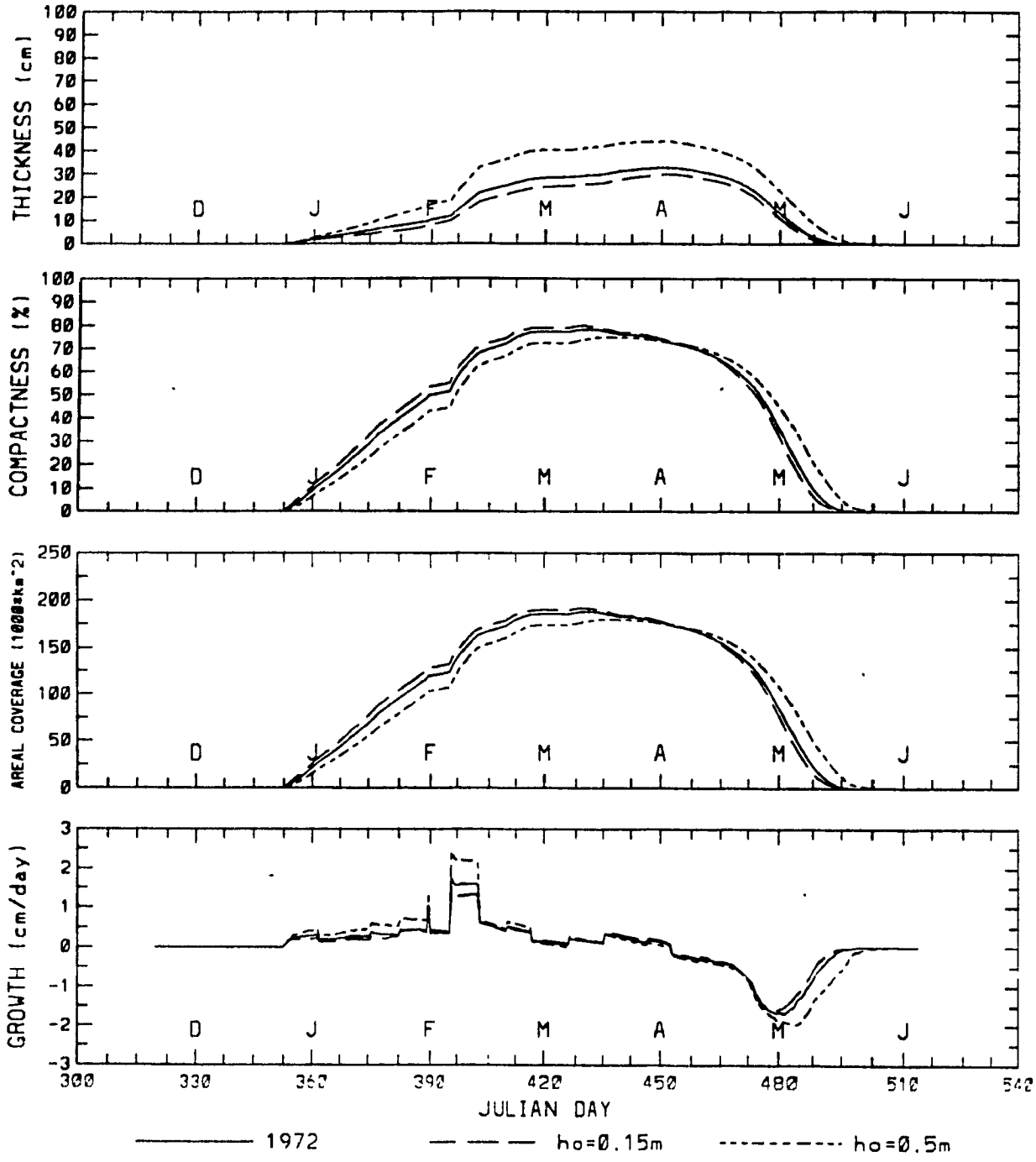

Figure 8.6 Experiment 6. Open water decay constant h_0=0.5 m & h_0=0.15 m.

8.6 Experiment 6 - Open Water Decay Constant

The simulation was very sensitive to changes in the open water decay constant h_0 which had a control value of 0.25 m (Figure 8.6). Increasing h_0 to 0.5 m decreased the rate at which open water closed, leading to a 10 cm more thick ice cover that had an unrealistically small compactness. Decreasing h_0 to 0.10 m caused open water to close more quickly, and decreased the amount of ice formed.

8.7 Experiment 7 - Ice Strength Constant

The ice strength P^* (27.5×10^3 $N\cdot m^{-2}$) was doubled to 55×10^3 $N\cdot m^{-2}$ and subsequently halved to 13×10^3 $N\cdot m^{-2}$. Increasing P^* stiffened the ice, causing fewer leads and slightly thinner ice (Figure 8.7). Restriction of ice motion prevented advection and ridging , and yielded spring ice compactnesses that were too large. Decreasing P^* led to slightly thicker ice and slightly smaller concentrations, caused by increased ridging.

8.8 Experiment 8 - Ice-Air Drag Coefficient

Doubling the ice-air drag coefficient from 2.4×10^{-3} to 4.8×10^{-3} increased the amount of open leads and resulted in more ice. Ice compactness was slightly reduced since greater wind forcing caused more advection and ridging. Decreasing the coefficient to 1.2×10^{-3} had the opposite effect (Figure 8.8).

8.9 Experiment 9 - Ice-Ocean Drag Coefficient

The ice-ocean drag coefficient was first doubled to 20×10^{-2} and then halved to

5×10^{-2}. These changes had a negligible effect on the simulation (Figure8.9).

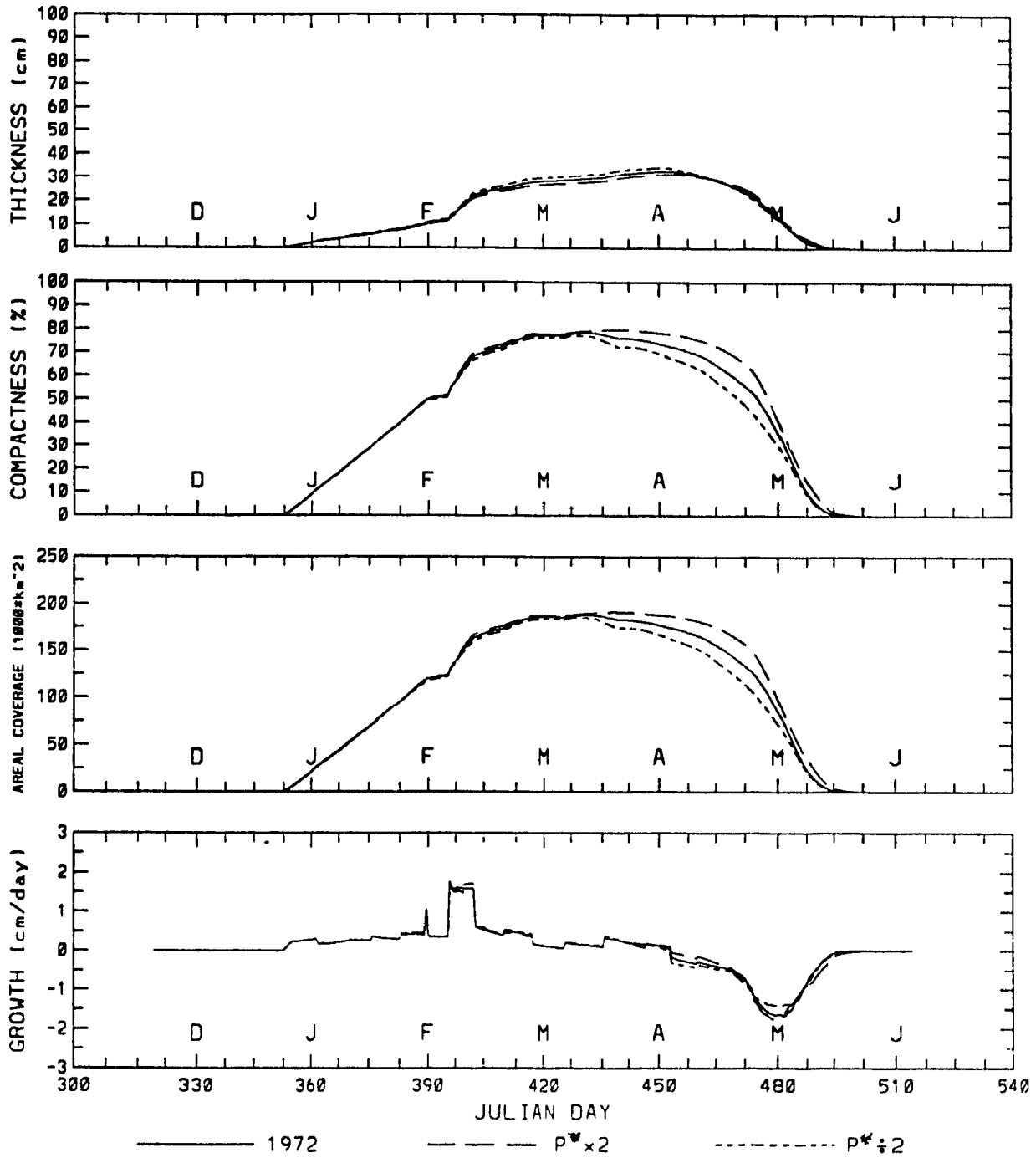

Figure 8.7 Experiment 7. Ice strength $P^* \times 2$ & $P^* \div 2$.

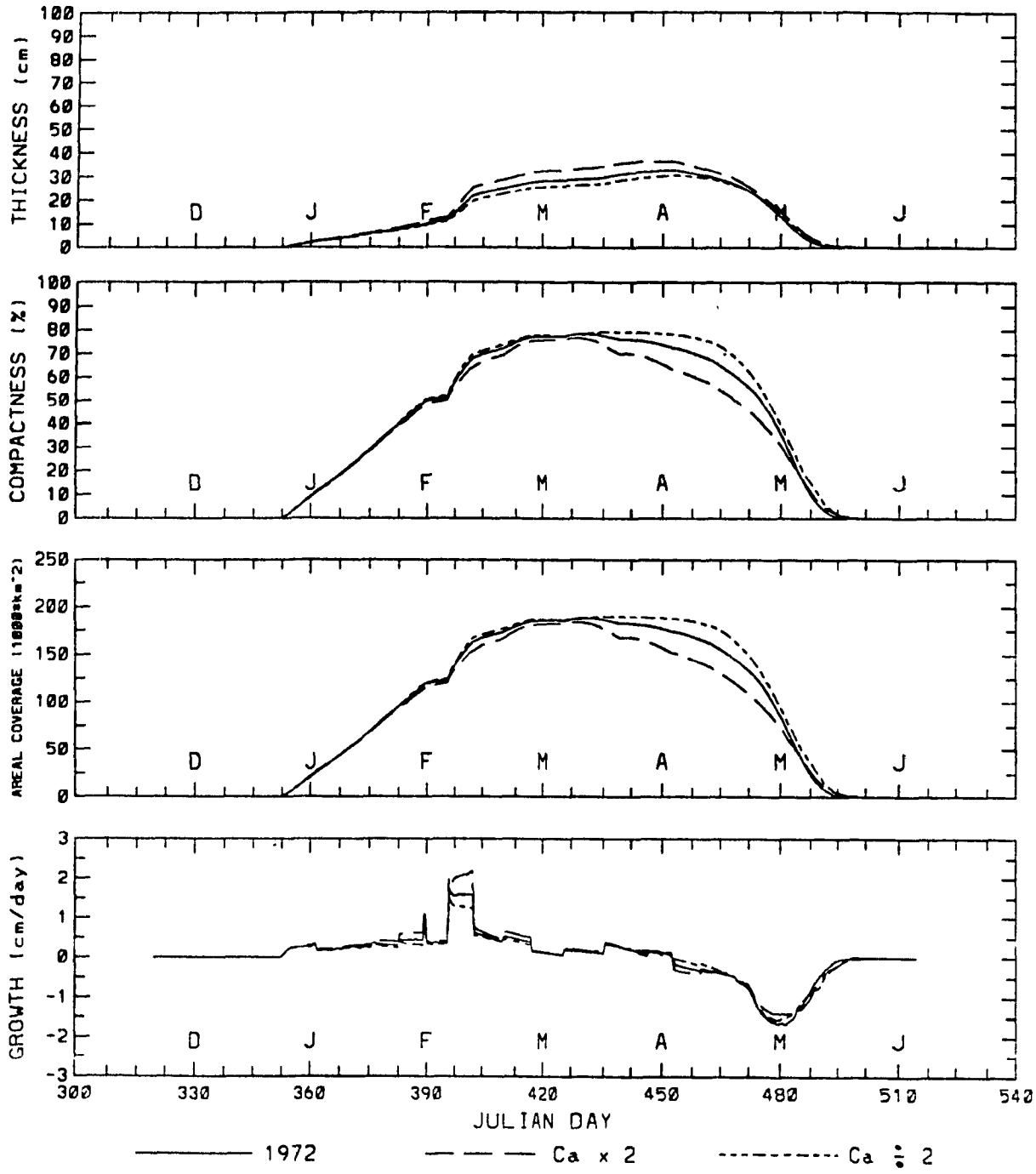

Figure 8.8 Experiment 8. Air-ice drag coefficient $C_a \times 2$ & $C_a \div 2$.

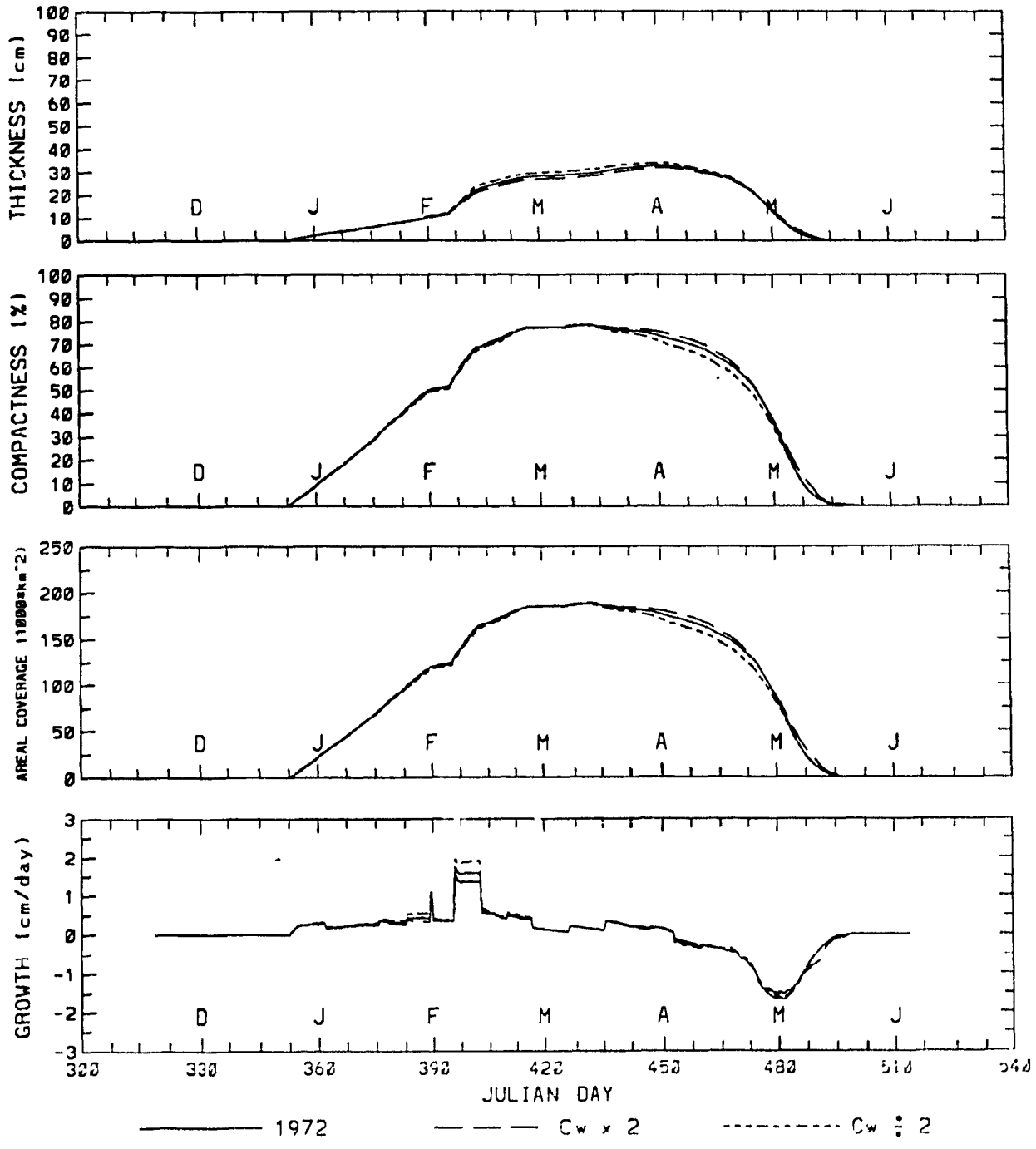

Figure 8.9 Experiment 9. Water-ice drag coefficient $C_w \times 2$ & $C_w \div 2$.

9. Conclusions

An uncoupled ice model was applied to the Gulf of St. Lawrence to examine interannual variability of the sea ice cover for the years 1968, 1969, and 1972. Although each simulation year was run using the same mixed layer depth field and prescribed deep ocean fluxes, differences in initial November SST's and the meteorological forcing were enough to simulate some of the variability, and capture the general features of the growth and evolution of the ice cover.

The following factors contribute to difficulties in modelling sea ice in the Gulf:

1) The large gradient across the Gulf, of all meteorological variables (air temp, snowfall, wind etc.) makes it difficult to produce reliable forcing fields, especially since there is only one station taking measurements in the Gulf itself, at Grindstone Island. A climatological model could be run using monthly averaged air temperatures taken from ship measurements (Vigeant 1984), but the results of this study suggest that weekly averaged meteorological data should be used for improved accuracy. Snow cover must be represented by weekly measurements.

2) There are not enough shipboard oceanographic measurements to produce reliable mixed layer depth fields, just before ice onset, for any given year: the lack of November data outside Cabot Strait, in the Magdalen Shallows, and in the northwest Gulf also limits the accuracy of the initial SST's. Similarly, a climatological model would not suffer from this inadequacy.

3) The modelled ice thickness was dominated by the value of deep ocean heat flux, which was chosen to produce reasonable thicknesses. Field measurements or a coupled model

would be needed to remove this arbitrariness from the simulation.

4) An uncoupled approach neglects some of the processes needed to simulate the ice cover and over-simplifies the treatment of the mixed layer. For example, wind induced upwelling at the ice edge may change the mixed layer thickness (Häkkinen 1987). Also, advection into the Gulf of outside water masses, such as run-off from the St. Lawrence River and warm water inflow through Cabot Strait , is probably important in modelling the Gulf ice cover.

A better understanding of sea ice in the Gulf of St. Lawrence could be achieved with the development of a coupled model, but the lack of oceanographic observations make the study of interannual variability unlikely at this time. A coupled, climatologically forced model would meet with more success.

References

Allison, I. 1981. Antarctic sea ice growth and oceanic heat flux, p.161-170 in I. Allison [ed.] *Sea Level Ice and Climatic Change*, IAHS, Washington D.C., publication 131, 303 p.

Ames, W.F. 1969. *Numerical Methods for Partial Differential Equations*. Barnes and Noble, New York, 291 p.

Anderson, D.L. 1961. Growth rate of sea ice. *J. Glaciol.*, 3, 1170-1172.

Bugden, G.L. 1981. Salt and heat budgets for the Gulf of St. Lawrence. *Can. J. Fish. Aqua. Sci.*, 38, 1153-1167.

Cambell, W.J. 1964. On the steady-state flow of sea ice. Dept. of Atmos. Sc., University of Washington, Seattle, 167p.

Coombs, J.A. 1962. A Preliminary investigation of the heat budget in the Gulf of St. Lawrence. Rep. 62-1, Bedford Inst. Oceanogr., Dartmouth, N.S., 65 p.

Coon, M.D. 1979. A review of AIDJEX modelling. Proc. ICSI/AIDJEX Symp. on Sea Ice Processes and Models, University of Washington, 96p.

Coon ,M.D., G.A. Maykut, R.S. Pritchard, and D.A. Rothrock. 1974. Modelling pack ice as an elastic-plastic material. *AIDJEX Bull.*, 24, 1-105.

Department of Transport, Meteorological Branch. 1968, 1969. Ice Summary and Analysis: Eastern Canadian Seaboard. Toronto, 50p., 50p.

Déry, F. 1992. Interannual and intraseasonal variability of the ice cover in the Gulf of St. Lawrence, 1963-1990. M.Sc. Thesis, Dept. of Atmos. and Ocean. Sci., McGill University, Montreal, Quebec, 220 p.

Doronin, Y.P. 1970. On a method of calculating the compactness and drift of ice floes. *Tr. Arkt. Antarkt.* Nauchno-Issled. Inst., 291, 5-17.

El-Sabh, M.I. 1976. Surface circulation patterns in the Gulf of St Lawrence *J. Fish. Res. Board Can.*, 33, 124-128.

Environment Canada, Atmospheric Environment Service. 1987. Climatic Atlas Canada. Ottawa.

Environment Canada, Atmospheric Environment Service. 1972. Ice Summary and Analysis, Eastern Canadian Seaboard. Toronto, 61 p.

Fel'zenbaum, A.I. 1958. The theory of steady drift of ice and the calculation of the long period mean drift in the central part of the arctic basin. *Problems of the North*, No.2.

Forrester, W.D. 1964. A quantitative temperature-salinity study of the Gulf of St. Lawrence. Rep. 64-11, Bedford Inst. Oceanogr., Dartmouth, Nova Scotia, 16 p.

Forrester, W.D., and P.E. Vandall, Jr. 1968. Ice volumes in the Gulf of St. Lawrence. Rep. 68-7, Bedford Inst. Oceanogr., Dartmouth, Nova Scotia , 16p.

Fukutomi, T. 1951. On the form and formation ot the hummocky ice ranges. *Low Temperature Science*, No.8, p.59-88.

Häkkinen, S. 1990. Models and their applications to polar oceanography, p.335-384 in W.O. Smith, Jr. [ed.] *Polar Oceanography, Part A*. Academic Press, Toronto, 406p.

Häkkinen, S. 1987. A coupled dynamic-thermodynamic model of an ice-ocean system in the marginal ice zone. *J. Geophys. Res.* 92, 9469-9478.

Haltiner, G.J., and R.T. Williams. 1980. *Numerical Prediction and Dynamic Meteorology*. John Wiley & Sons, New York, 477 p.

Herfst, F.J. 1984. Wind Regimes in the St. Lawrence River valley. M.Sc. thesis, University of Toronto, Toronto, 152 p.

Hibler, W.D. III. 1979. A dynamic thermodynamic sea ice model. *J. Phys. Oceanogr.*, 9, 815-846.

Hibler, W.D. III. 1980. Modeling variable thickness sea ice cover. *Mon. Weather Rev.*, 108, 1943-1973.

Hibler, W.D. III and K. Bryan. 1984. Oceanic circulation: Its effect on seasonal sea ice simulations. *Science*, 224, 489-492.

Hibler, W.D. III and K. Bryan. 1987. A diagnostic ice-ocean model. *J. Phys. Oceanogr.*, 17, 987-1015.

Hibler, W.D. III and J.E. Walsh. 1982. On modeling seasonal and interannual fluctuations of the Arctic sea ice. *J. Phys. Oceanogr.*, 12, 1514-1523.

Koutitonsky, V.G., and G.L. Bugden. 1991. The physical oceanography of the Gulf of St. Lawrence: a review with emphasis on the synoptic variability of the motion, p. 57-90. in J.-C. Therriault [ed.]. *The Gulf of St. Lawrence: Small Ocean or Big Estuary?* Can. Spec. Publ. Fish. Aquat. Sci. 113. 359p.

Laevatsu, T. 1960. Factors affecting the temperature of the the surface layer of the sea. *Comment. Phys. Math.*, 25, 1.

Lauzier, L.M., and W.B. Bailey. 1957. Features of the deep waters of the Gulf of St. Lawrence. *Bull. Fish. Res. Board Can.*, 111, 213-250.

Levitus, S. 1982. *Climatological Atlas of the World Ocean*. NOAA Prof. Pap, 13, Natl. Oceanic and Atmos. Admin., Washington D.C., 173 p.

Matheson, K.M. 1976. The Meteorological Effect on Ice in the Gulf of St. Lawrence. Publ. in Meteorology No. 110, McGill University, Montreal, 107 p.

Maykut, G.A. 1986. The surface heat and mass balance [of sea ice] in p.395-464 N. Untersteiner [ed.], *The Geophysics of Sea Ice*, Plenum Press.

Maykut, G.A. and Untersteiner, N. 1971. Some results from a time-dependant thermodynamic model of sea ice. *J. Geophys. Res.*, 76, 1550-1575.

Mesinger, F., and A. Arakawa. 1976. *Numerical Methods Used in Atmospheric Models.* GRAP pulb. Ser. no.17, Geneva, 64 p.

Nikiforov, E.G. 1957, Variation in ice compactness due to its dynamics. *Probl. Arktiki*, Vol.2, Morskoi Trans. Leningrad.

Overland, J.E. 1985. Atmospheric boundary layer structure and drag coefficients over sea ice. *J. Geophys. Res.*, 90, 9029-9049.

Overland, J.E. and C.H.Pease. 1988. Modeling ice dynamics of coastal seas. *J. Geophys. Res.* 93, 15619-15637.

Parkinson, C.L. and W.M. Washington. 1979. A large scale numerical model of sea ice. *J. Geophys. Res.*, 84, 311-337.

Pritchard, R.S. 1975 An elastic plastic constitutive law for sea ice. *J. Appl. Mech.*, 42, 379-384.

Rossby, C.G., and R.B. Montgomery. 1935. The layer of frictional influence in wind and ocean currents. Papers in Physical Oceanography, MIT, Vol.3.

Semtner, A.J. 1974. An oceanic general circulation model with bottom topography. Numerical Simulation of Weather and Climate, Tech. Rep. No.9, Dept. of Meterol., Univ. of California, Los Angeles, 99p.

Semtner, A.J. 1976. A model for the thermodynamic growth of sea ice in numerical investigations of climate. *J. Phys. Ocean.*, 6,379-389.

Semtner, A.J. 1987. A numerical study of sea ice and oceanic circulation in the Arctic. *J. Phys. Oceanogr.*, 17, 1077-1099.

Shirasawa, K., and R.G. Ingram. 1991. Characteristics of the turbulent oceanic boundary layer under sea ice. Part 1: A Review of the Ice-Ocean Boundary Layer. *J. Marine. Systems*, 2, 153-160.

Shuleikin, V.V. 1938, The drift of ice fields. *Doklady. Akad. Nauk SSSR*, Vol 19, No.8.

Sverdrupp, H.U. 1928. The wind drift of the ice on the north Siberian Shelf: The Norweigan North Polar Expedition with "Maud", 1918-1925. *Scientific Results*,4, No.1.

Tang, C.L., and T. Yao. 1992. A simulation of sea-ice motion and distribution off Newfoundland during LIMEX, March 1987. *Atmosphere-Ocean*. 30, No.2, 270-296.

Trites, R.W. 1972. The Gulf of St. Lawrence from a pollution point of view. p.59-72 in M.Ruivo[ed.] *Marine Pollution and Sea Life*. FAO, Fishing News Books, London.

Washington, W.M.. A.J. Semtner, C.L. Parkinson and L. Morison. 1976. On the development of a seasonal change sea-ice model. *J. Phys. Ocean.*, 90, 679-685.

Zillman, J.W. 1972. A study of some aspects of the radiation and heat budgets of the southern hemisphere oceans. *Meteor. Stud.*, 26, 562 p. Bureau of Meteor. Dept. of Interior, Canberra, Australia.

Zubov, N.N. 1945. *Arctic Ice*. Trans. by USAF Cambridge Research Centre, 491 p.

Appendix

Analyzed Forcing Fields

This appendix contains maps of all the forcing fields used in this modelling study. Chapter 6 describes how these fields were produced.

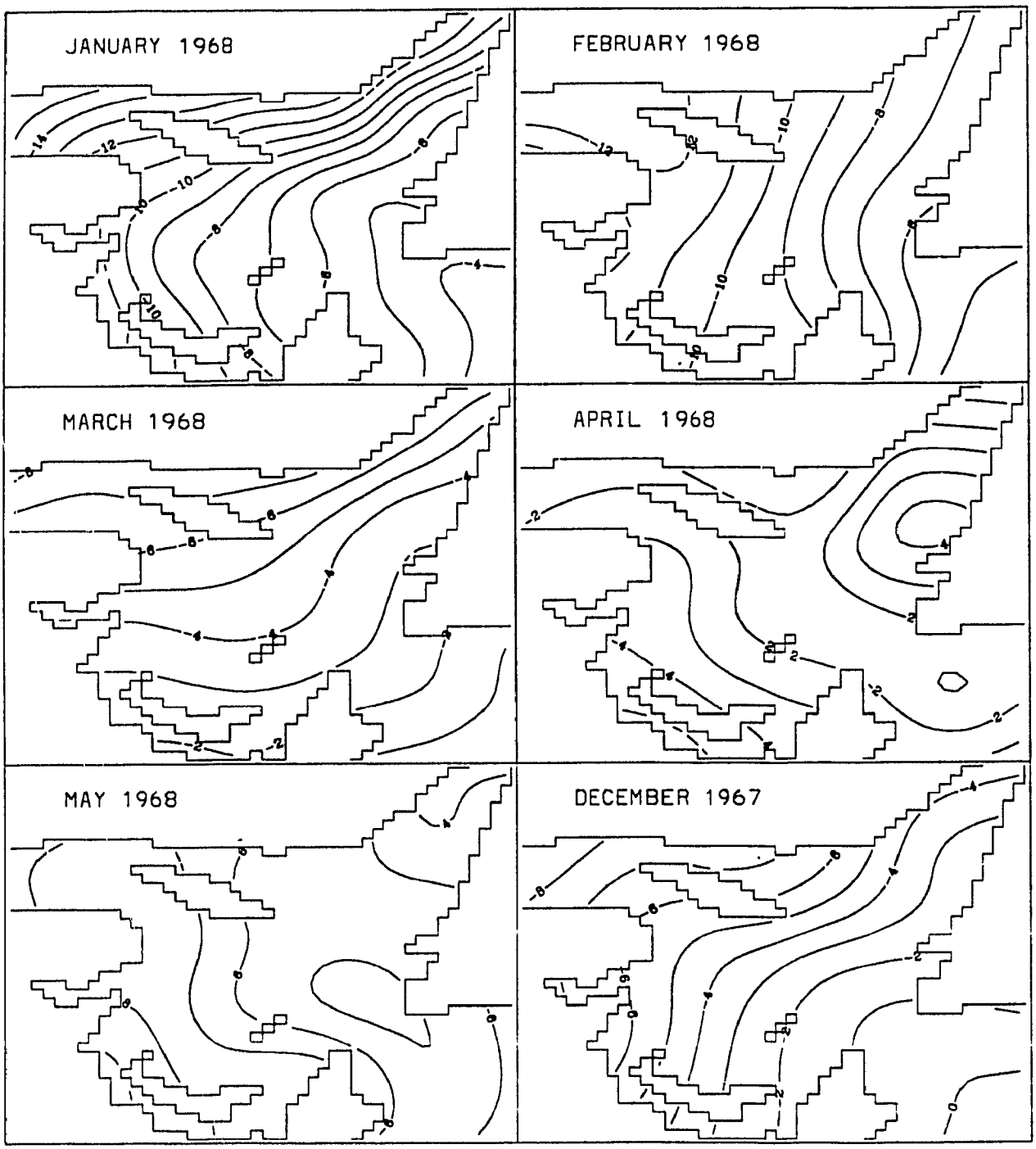

Figure A.1 Air temperature. 1°C contour interval.

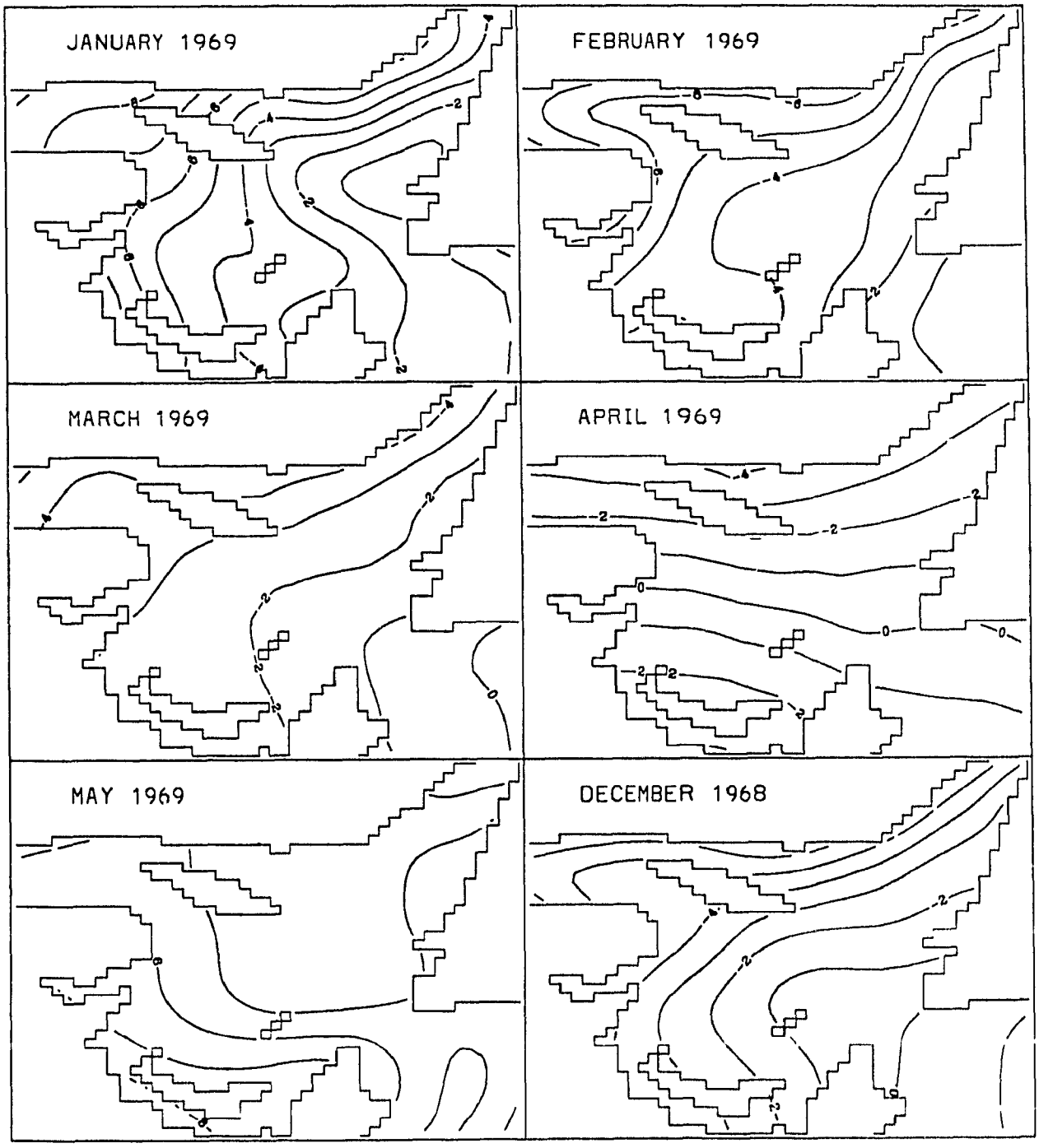

Figure A.1 continued.

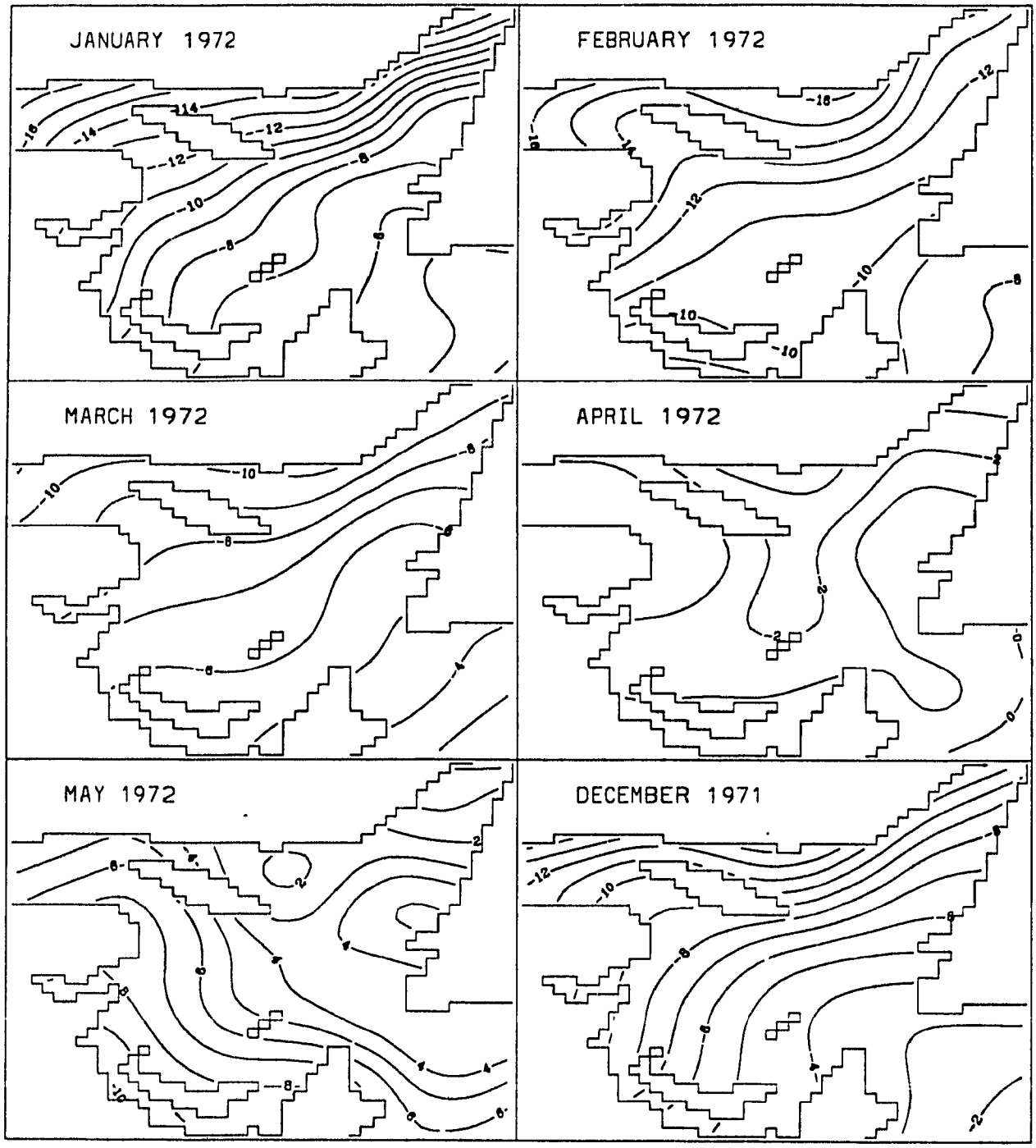

Figure A.1 continued.

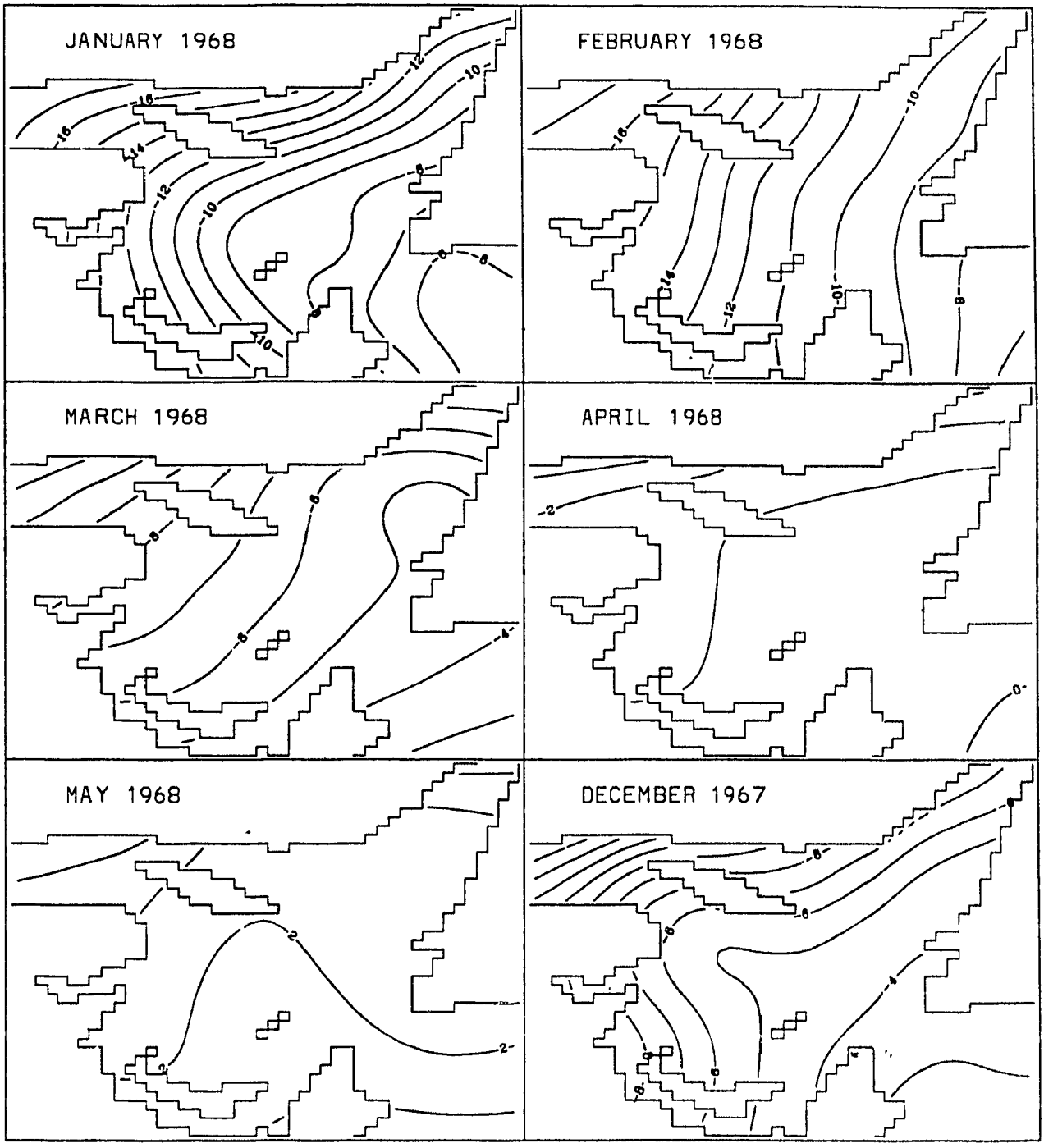

Figure A.2 Dew point temperature. 1°C contour interval.

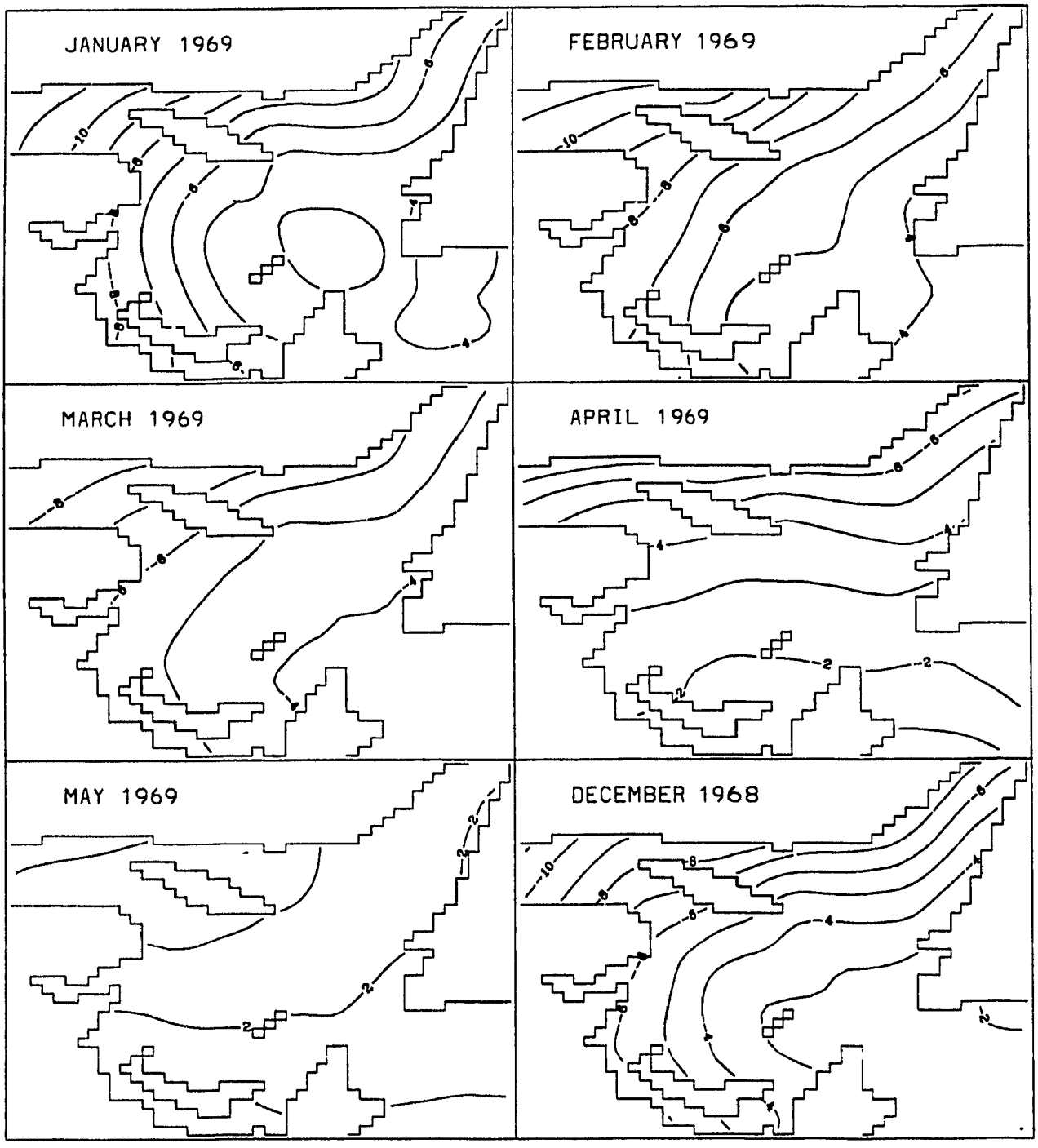

Figure A.2 continued.

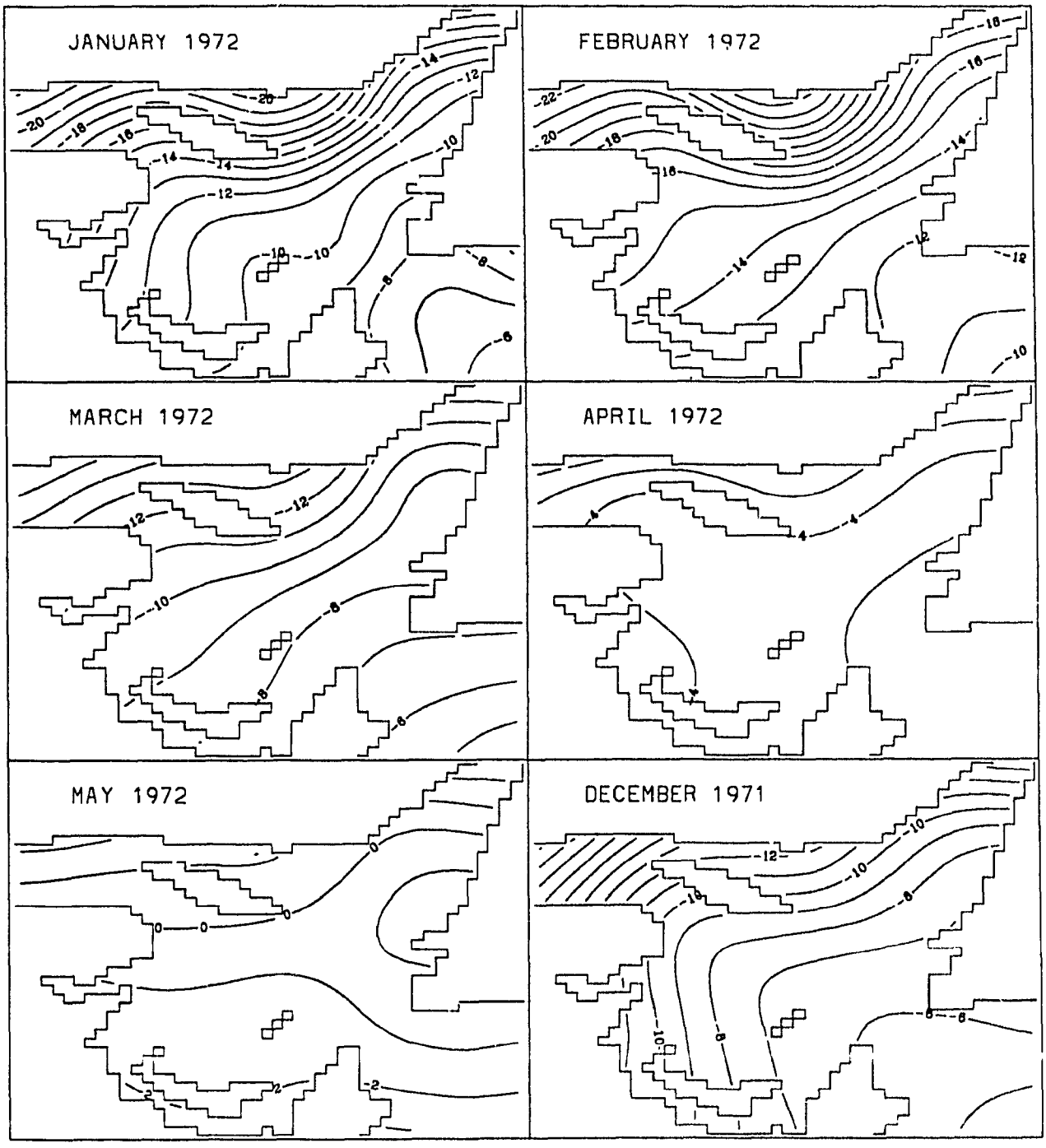

Figure A.2 continued.

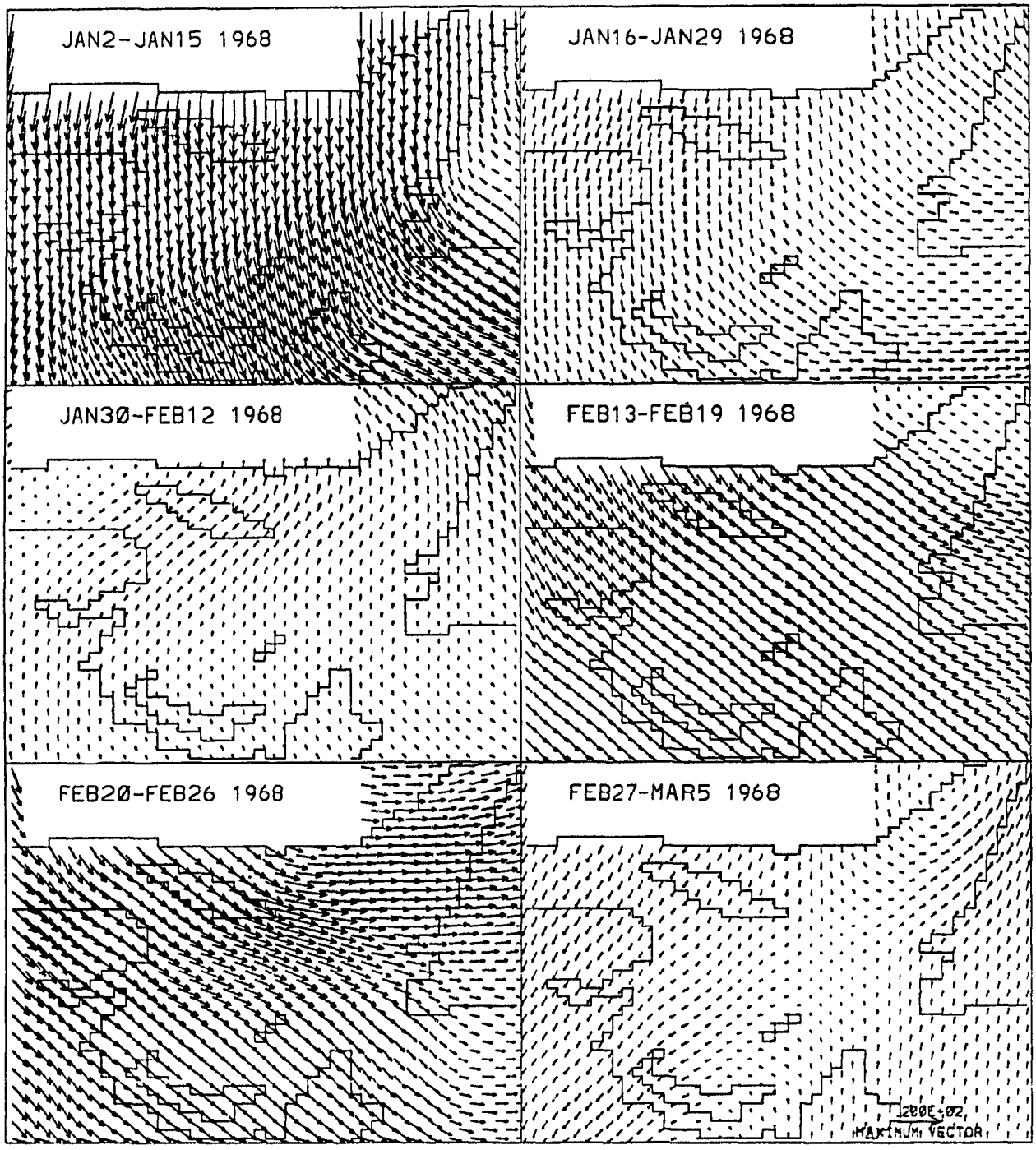

Figure A.3 Surface geostrophic wind. Longest vector is 20m•s^{-1}.

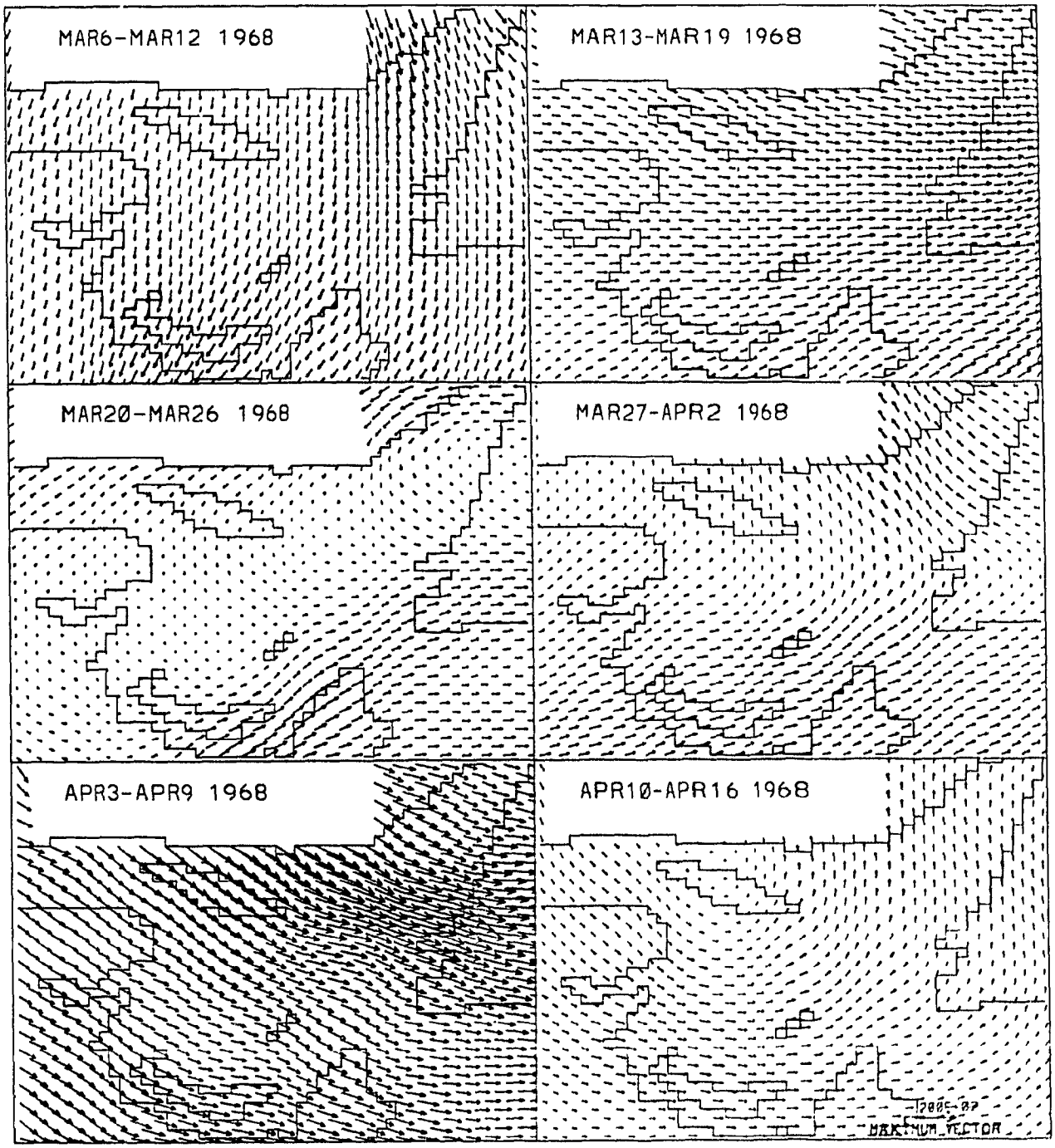

Figure A.3 continued

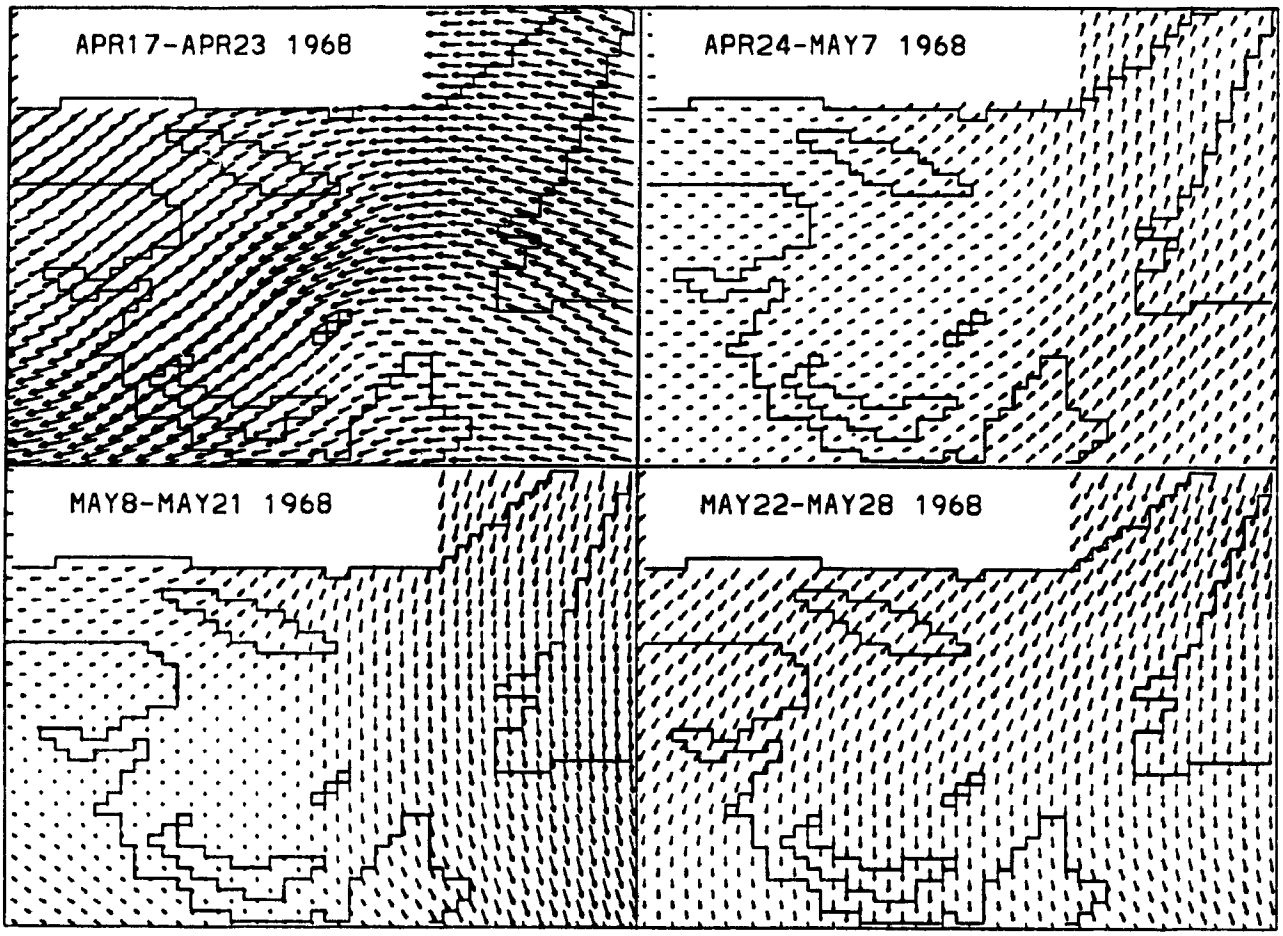

Figure A.3 continued

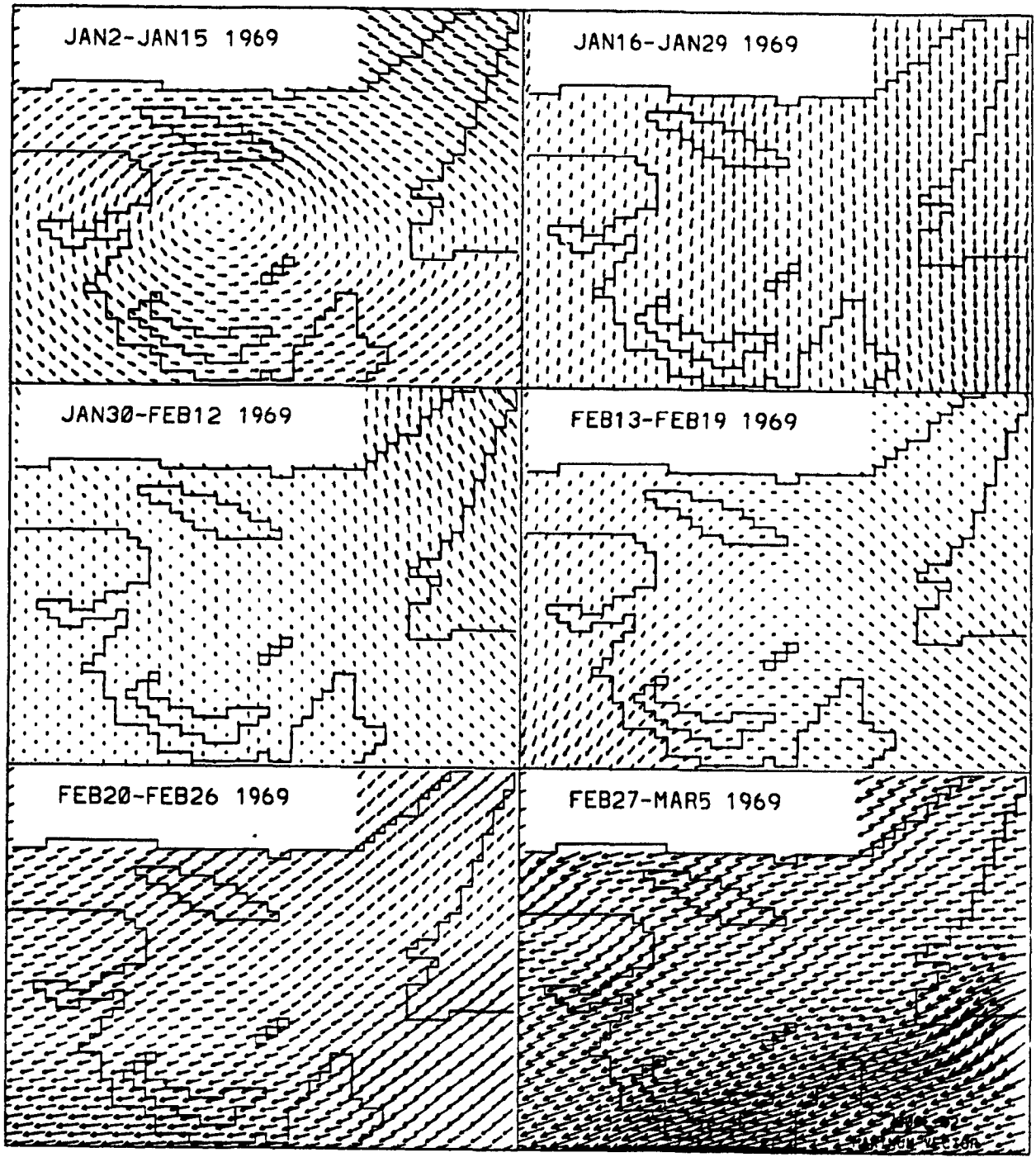

Figure A.3 continued

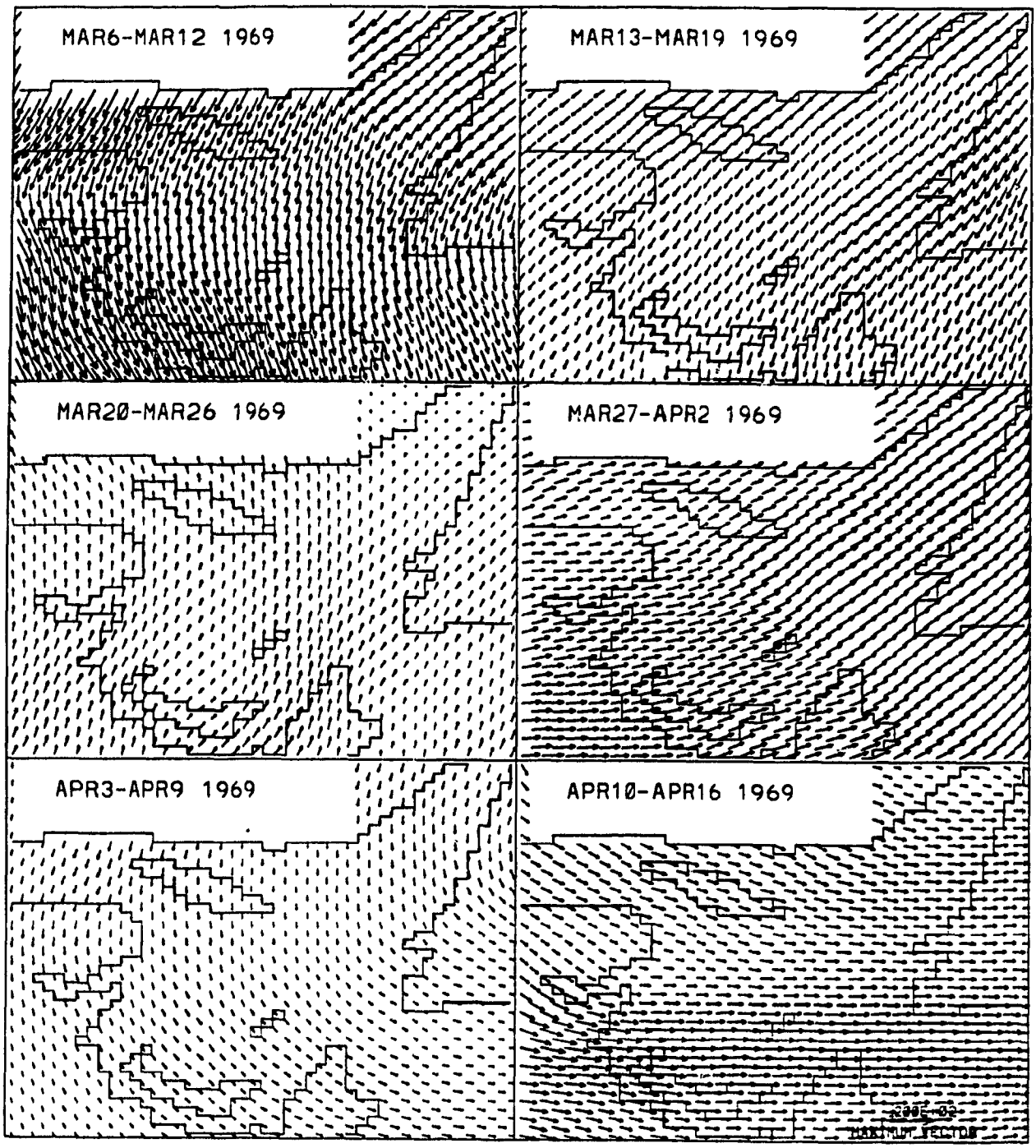

Figure A.3 continued

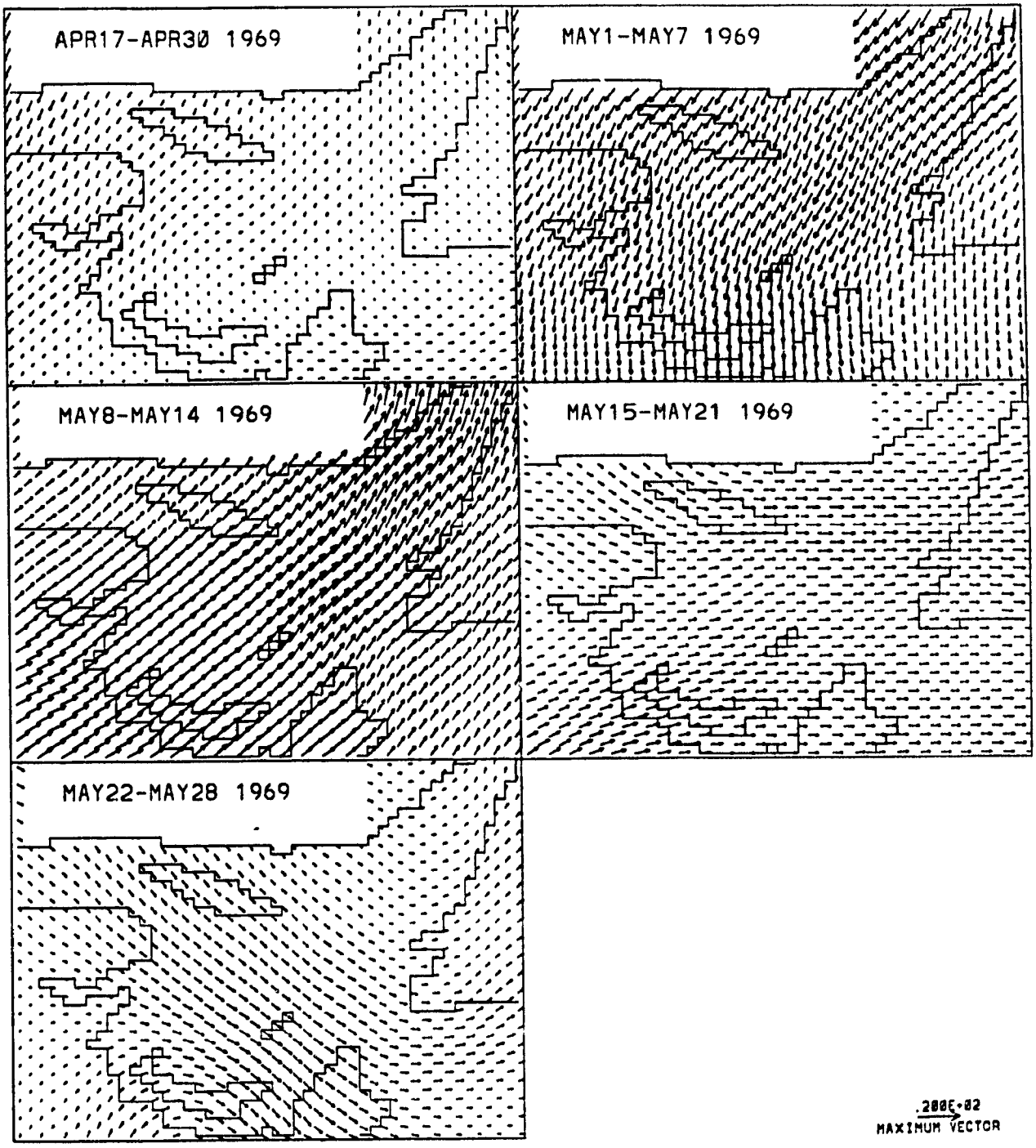

Figure A.3 continued

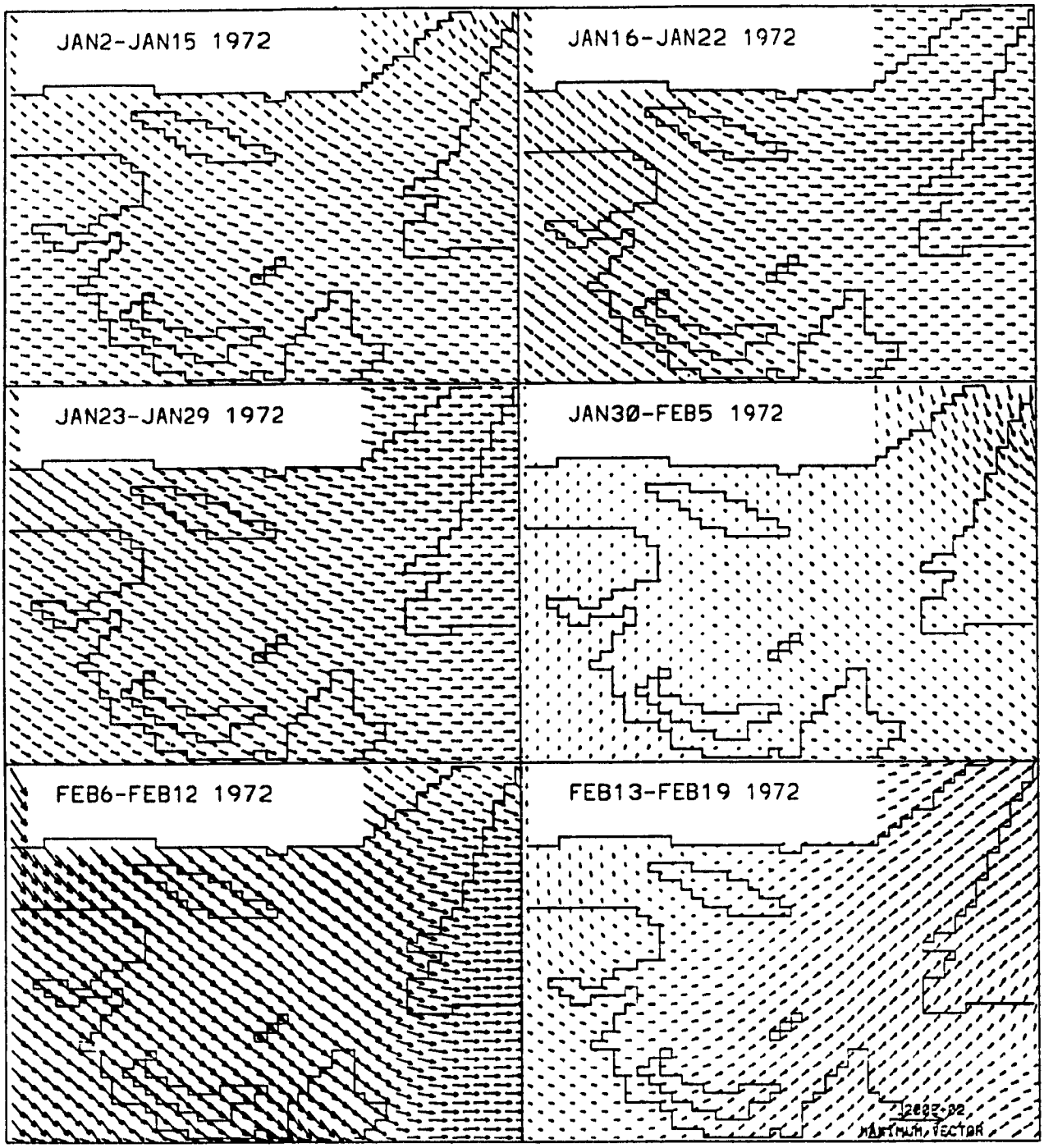

Figure A.3 continued

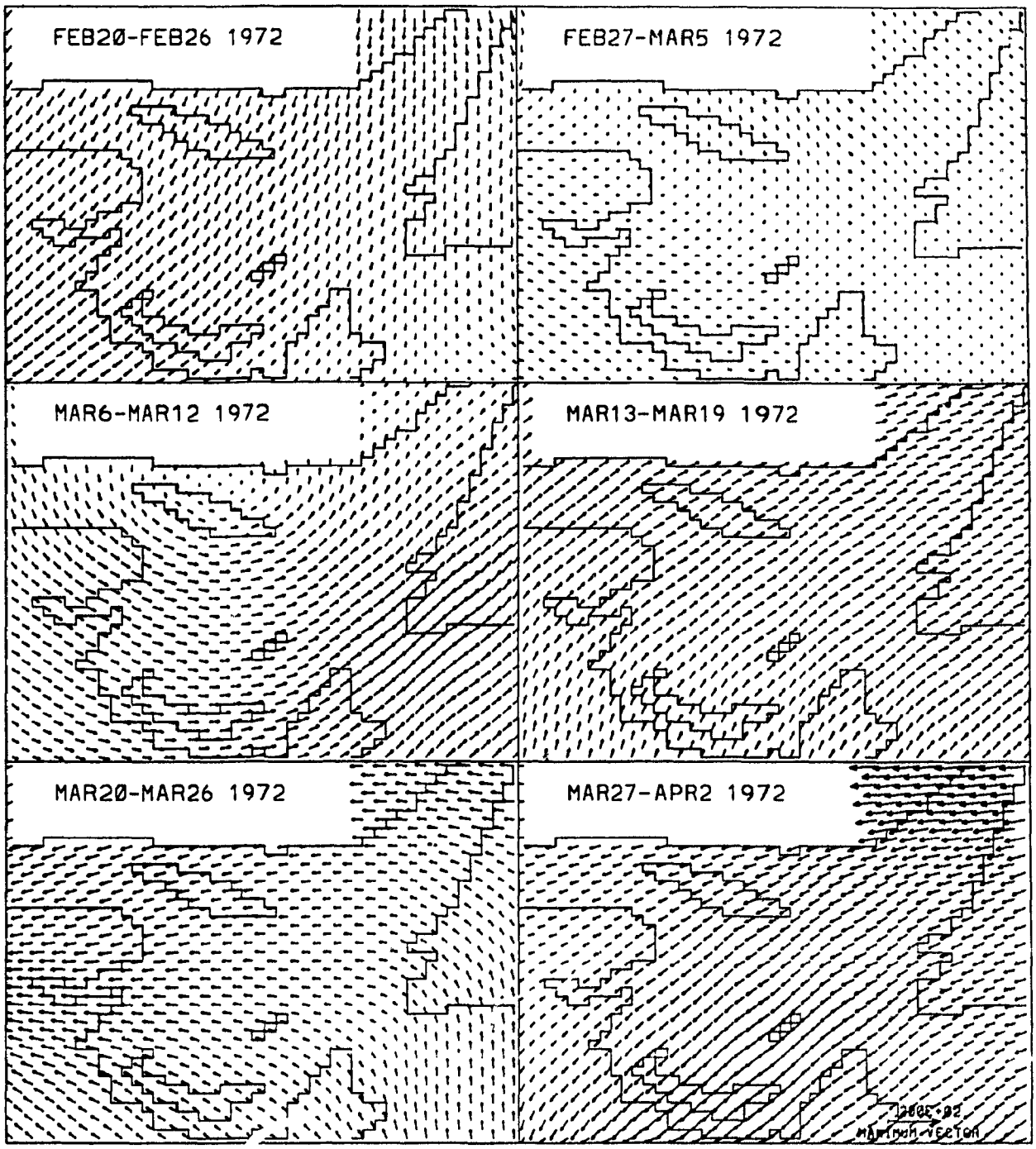

Figure A.3 continued

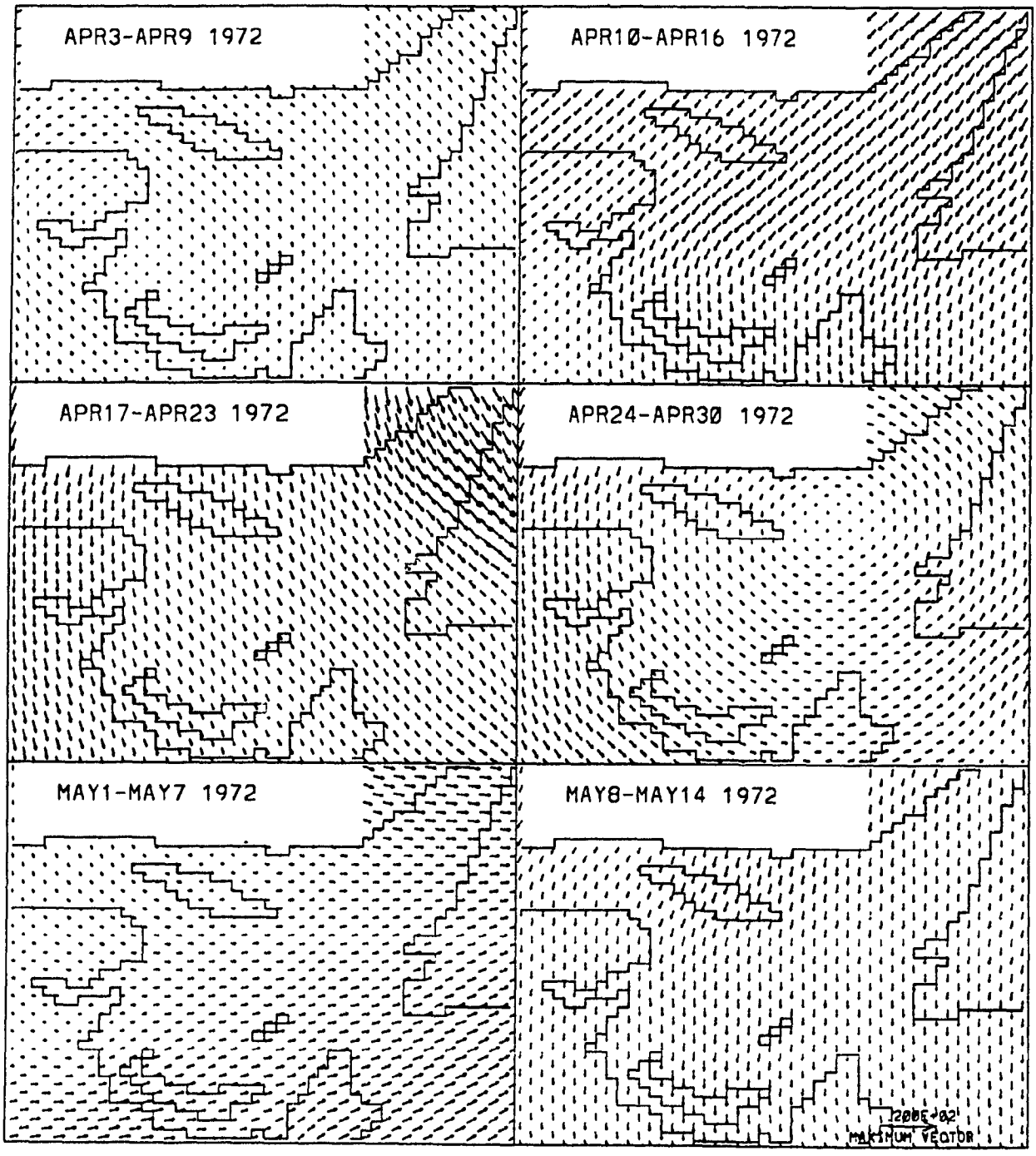

Figure A.3 continued

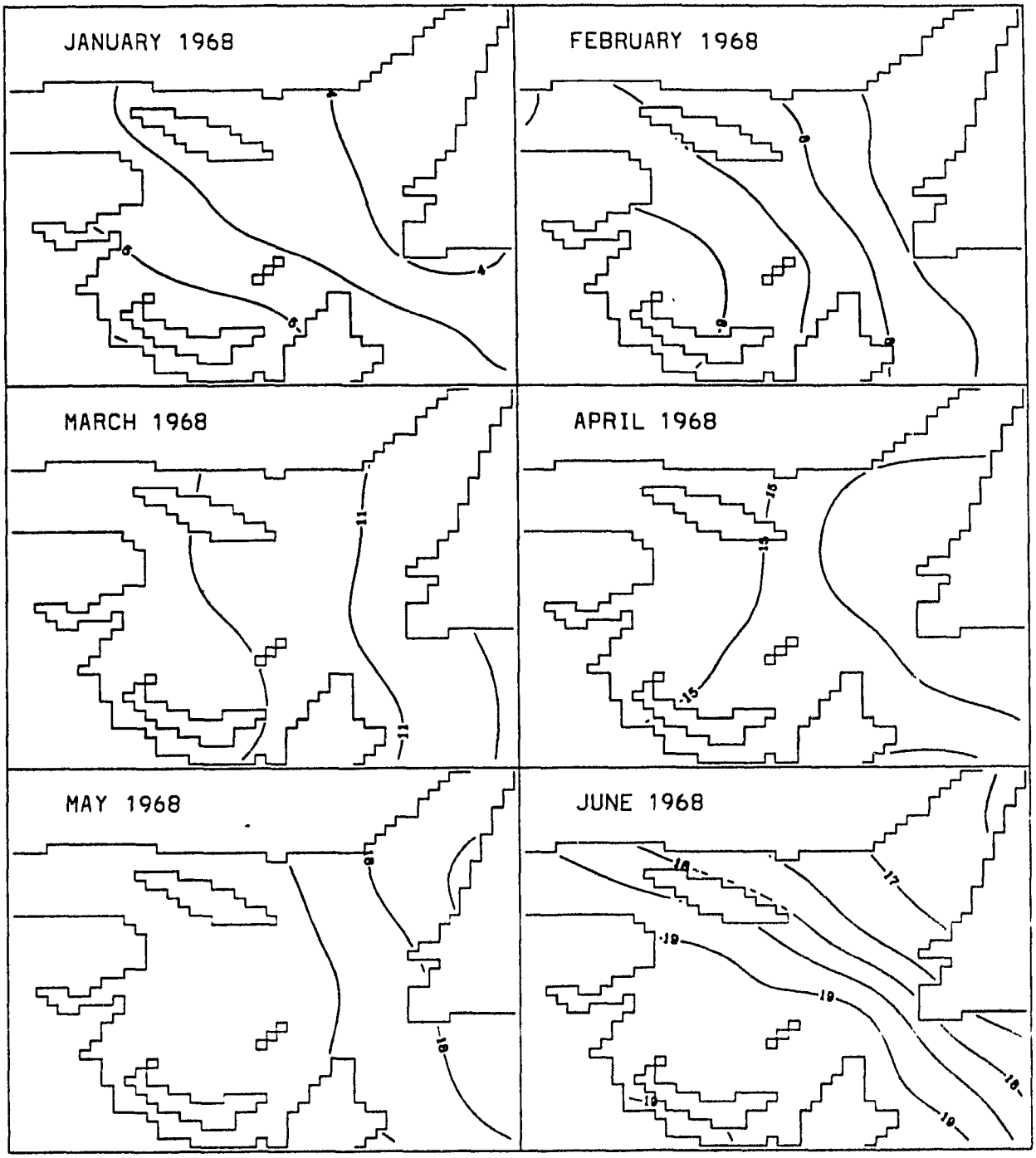

Figure A.4 Incoming Global Solar Radiation. 0.5 MJ/day contour interval. 1 MJ/day = 11.57 $W \cdot m^{-2}$.

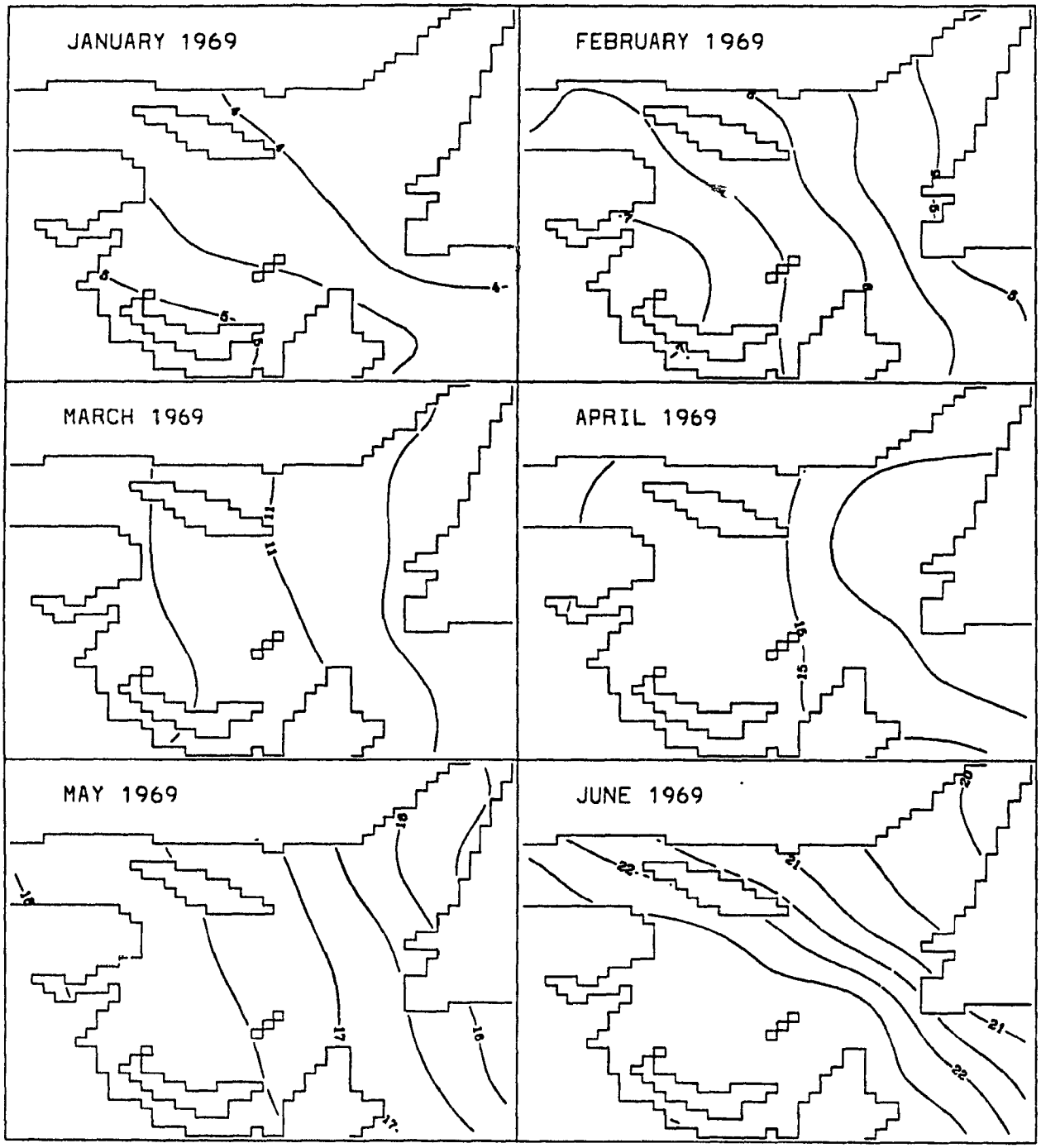

Figure A.4 continued.

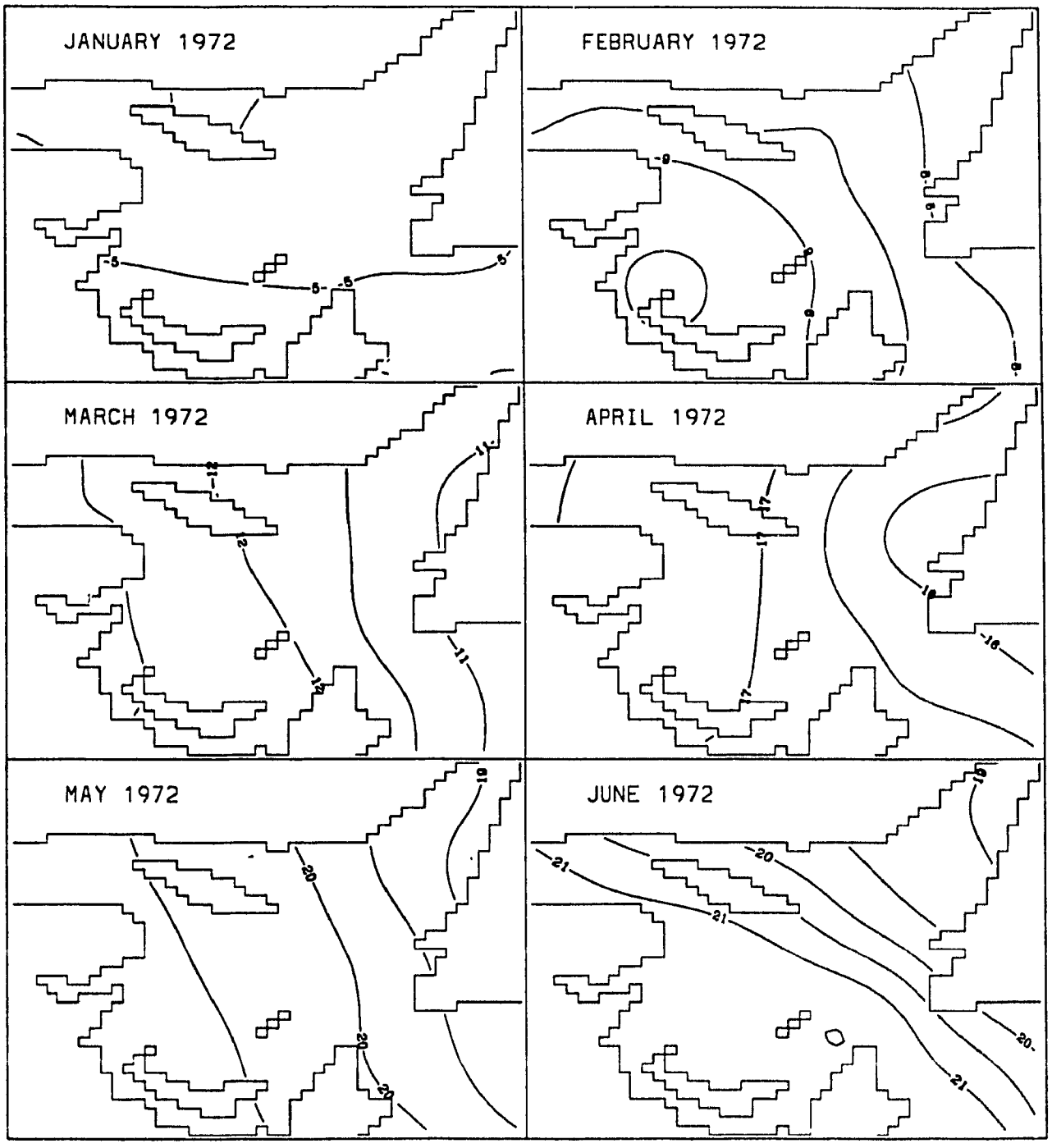

Figure A.4 continued.

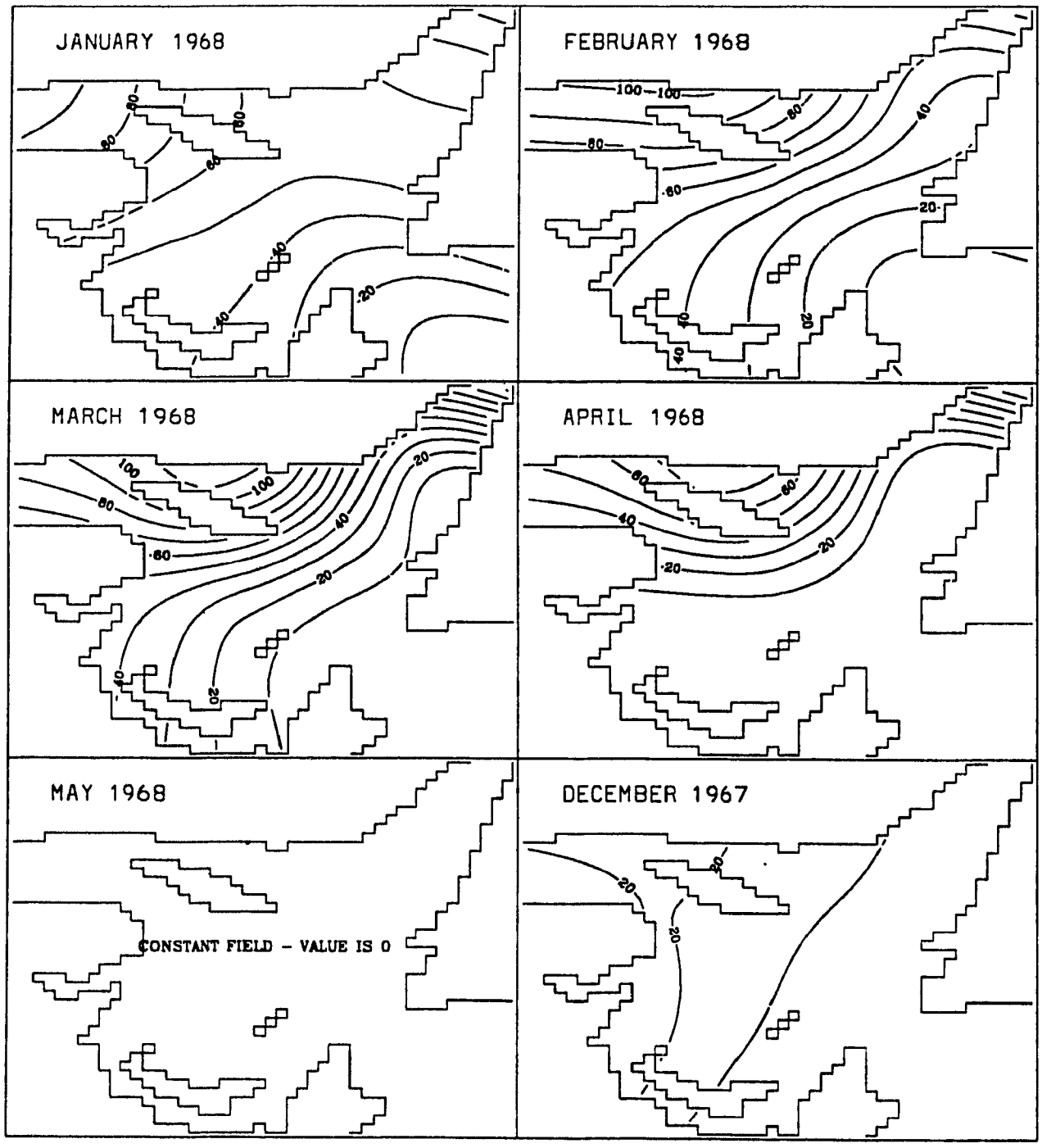

Figure A.5 Monthly averaged snowdepth. 10 cm contour interval.

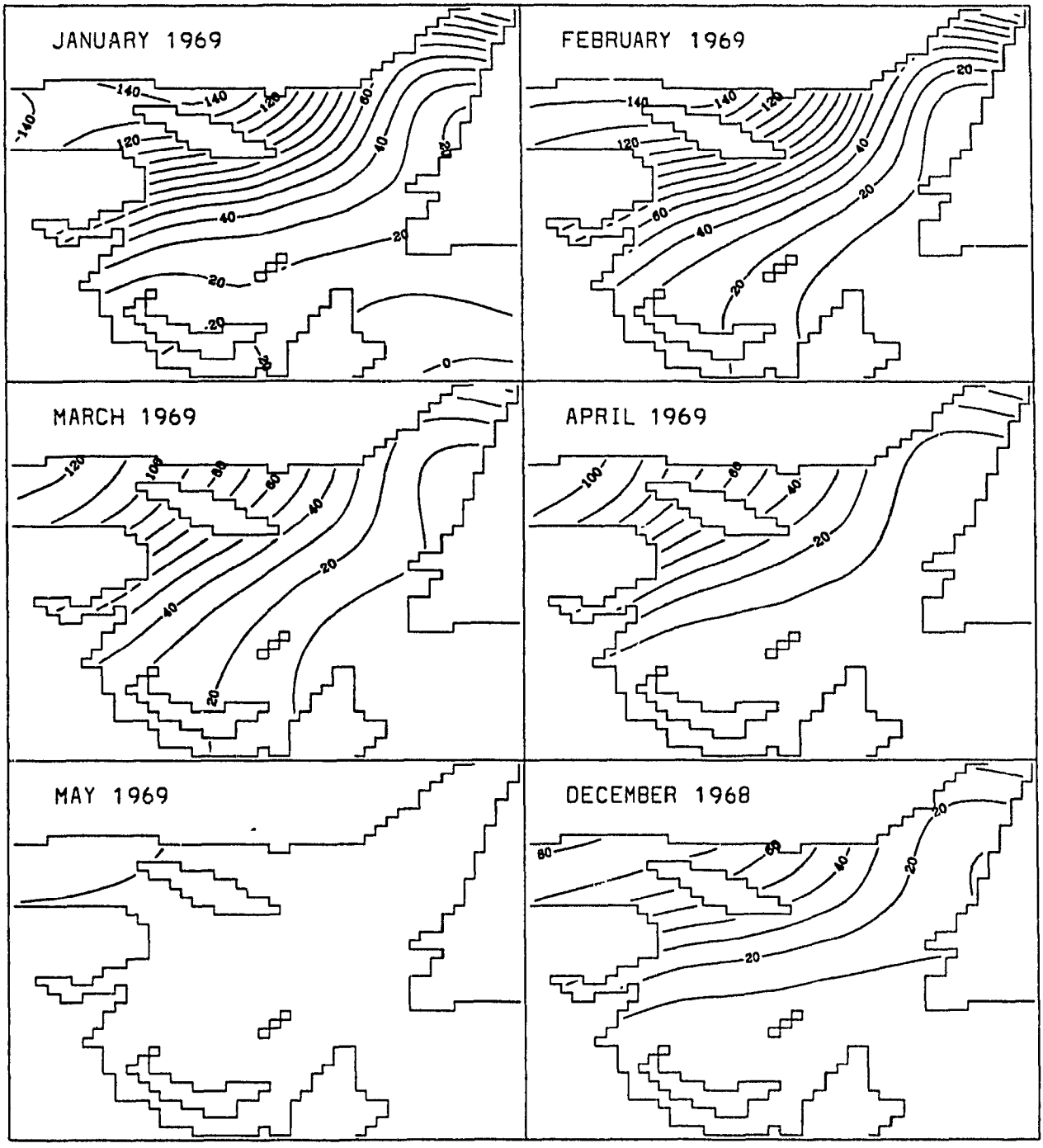

Figure A.5 continued.

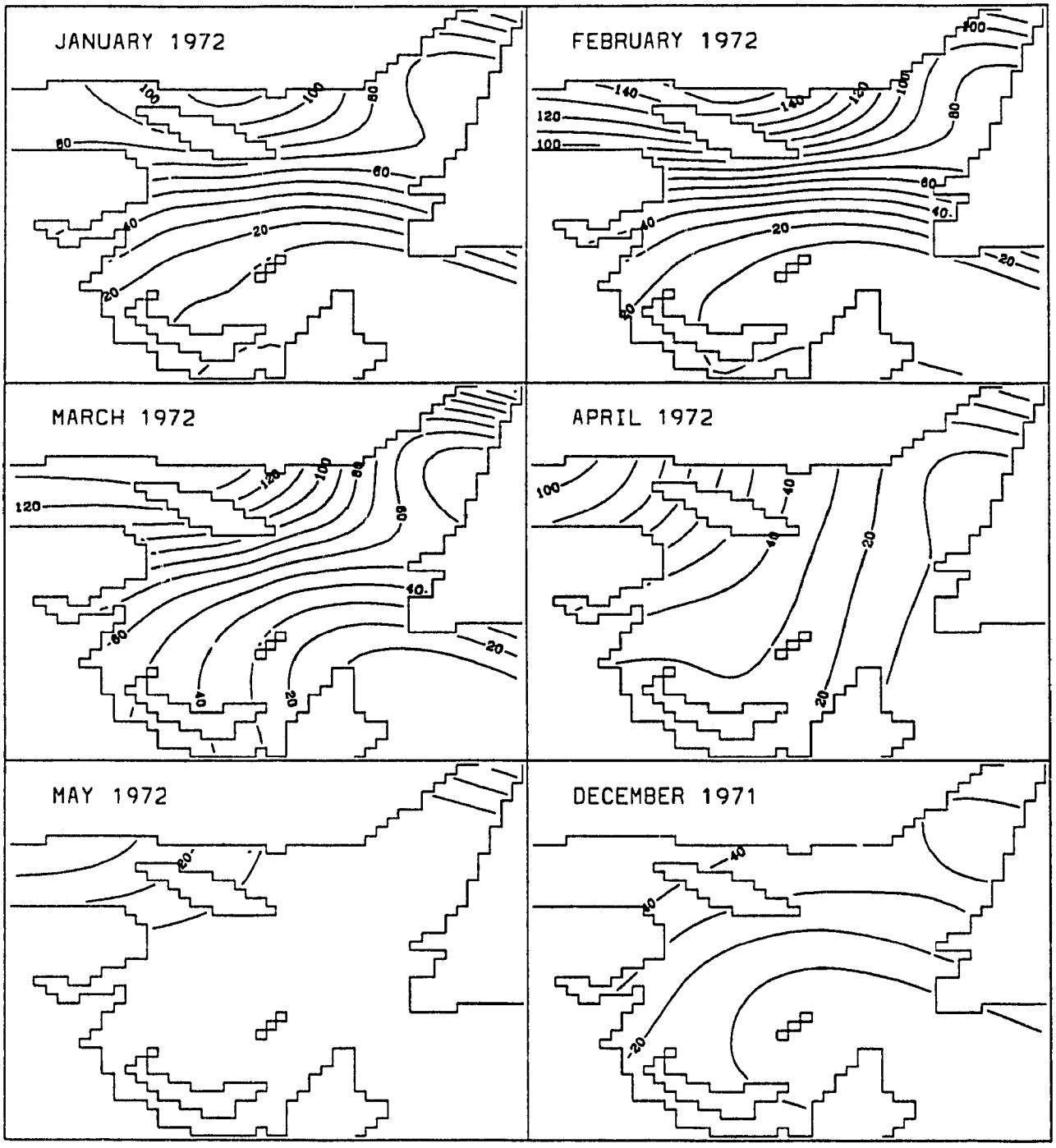

Figure A.5 continued.

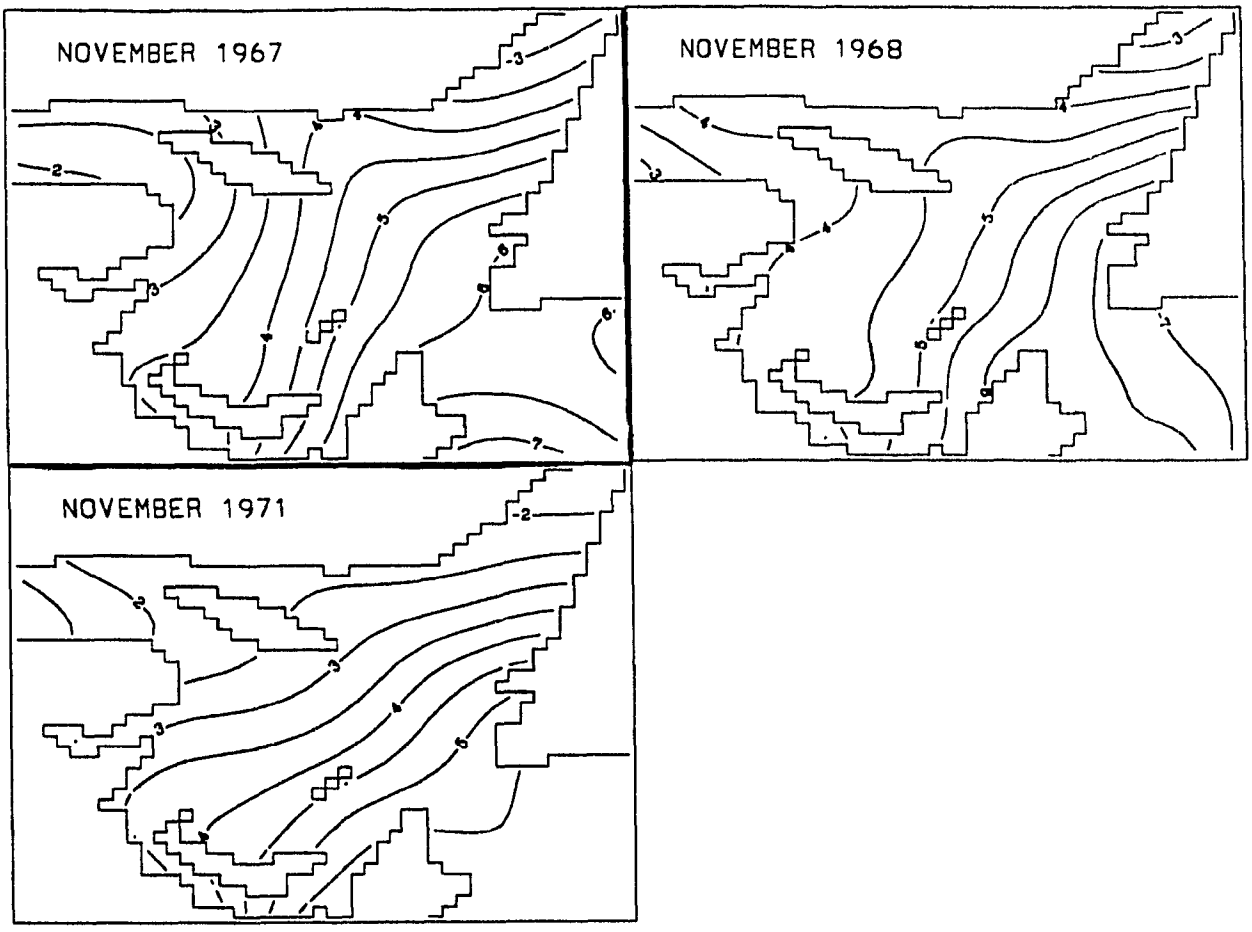

Figure A.6 November sea surface temperature. 0.5°C contour interval.